

## Deliverable 2.13

# Validation of high rotational speed aerodynamics by wind tunnel tests

Part I September 2014

Part II June 2015

Agreement no.:	308974
Duration	60 months from 1st November 2012
Coordinator:	Mr Peter Hjuler Jensen
Supported by:	EU 7th Framework Programme

Support by:



The InnWind deliverable D2.13 “Validation of high rotational speed aerodynamics by wind tunnel tests” contains two main measurable parts:

- MEXICO rotor tested in the DNW tunnel
- Simulation models validated against the new MEXICO data

The reporting was split up in two separate parts where the first part finished in September 2014 addresses the first measurable. The second part was finished in June 2015 and reports the second measurable.

The two parts are:

- **New MEXICO experiment** – Preliminary overview with initial validation, September 2014
- **Validation of models by the new MEXICO data**, June 2015

The present report contains both parts which are separate. It means also that each part has its own “Table of contents” and “Reference list”.

## Document information

Document Name:	New MEXICO experiment – Preliminary overview with initial validation
Confidentiality Class	PU
Document Number:	D2.13 Part I
Contributing Authors:	K. Boorsma, J.G. Schepers
Review:	Helge Aagaard Madsen (DTU), Flemming Rasmussen (DTU), Francesco Grasso (ECN)
Date:	September 2014
WP:	WP2 LIGHTWEIGHT ROTOR
Task:	Task 2.13 Validation by experiments

# New MEXICO experiment

Preliminary overview with initial validation

K. Boorsma, J.G. Schepers

September 2014

ECN-E--14-048



## Acknowledgement

Financial support for this work was given in part by the EU INNWIND project. In addition to that the European ESWIRP project has been responsible for sponsoring the tunnel time in the DNW. The support of the the steering committee (Delft University of Technology, Technion Israel Institute of Technology and DTU Technical University of Denmark), which advised during the preparation of the tunnel test, was greatly appreciated.

Last but not least the test would have never been made possible without the assistance of Giel Hermans (DEMO), Arie Wolf and Doron Ben-Shmuel (Technion), Nando Timmer and Daniel Baldacchino (Delft University of Technology), Özlem Ceyhan (ECN), the ESWIRP students and off course the whole DNW team.

## Abstract

This report gives an overview of the New MEXICO wind turbine measurements as carried out in the the Large Scale Low Speed Facility (LLF) of the German Dutch Wind Tunnels (DNW) between June 20<sup>th</sup> and July 4<sup>th</sup> 2014. The test is a follow up of the first MEXICO campaign, which was held in 2006. The main objective of the test is to progress aerodynamic (and acoustic) modelling of wind turbines and wind turbine farms. The test preparation activities are described, including a pressure sensors calibration and static wind tunnel test of the blades. Some preliminary results of the rotating test are discussed. Several open questions from the first campaign have been resolved and a good agreement has been found between these measurements. The MEXICO database has been extended with extra test cases to progress modelling of dynamic inflow, non-uniformity between the blades, yawed flow effects, parked conditions and pitch misalignment. In addition to that several blade add-ons were tested to improve the turbine performance. Acoustic measurements have been performed using both far field microphones as well as a microphone array. Flow visualization was performed by application of smoke candles to the blade tips and oil to the blade surface.

In summary, after years of preparation, ECN and partners have performed very successful aerodynamic experiments in the largest wind tunnel in Europe. The comprehensive high quality database that has been obtained will be used in an international consortium to further develop wind energy aerodynamic modelling.

Although the information contained in this report is derived from reliable sources and reasonable care has been taken in the compiling of this report, ECN cannot be held responsible by the user for any errors, inaccuracies and/or omissions contained therein, regardless of the cause, nor can ECN be held responsible for any damages that may result therefrom. Any use that is made of the information contained in this report and decisions made by the user on the basis of this information are for the account and risk of the user. In no event shall ECN, its managers, directors and/or employees have any liability for indirect, non-material or consequential damages, including loss of profit or revenue and loss of contracts or orders.



# Contents

<b>1</b>	<b>Introduction</b>	<b>5</b>
1.1	Historical review	5
<b>2</b>	<b>Objectives</b>	<b>11</b>
2.1	Outstanding Mexnext research questions	11
2.2	Validate and compliment first MEXICO campaign	11
2.3	Additional priorities	13
<b>3</b>	<b>Test set-up and preparations</b>	<b>15</b>
3.1	Wind turbine model	15
3.2	Measurement apparatus	16
3.3	Verification of pressure sensors and data acquisition	17
<b>4</b>	<b>Test matrix</b>	<b>29</b>
4.1	PIV overview	33
<b>5</b>	<b>Preliminary results</b>	<b>39</b>
5.1	Tunnel calibration and velocity verification	39
5.2	Comparison to MEXICO	42
5.3	Influence of roughness	49
5.4	Flow visualization	54
<b>6</b>	<b>Conclusions</b>	<b>57</b>
	<b>Bibliography</b>	<b>59</b>
<b>A</b>	<b>Kulite® specification sheet</b>	<b>61</b>



# 1

## Introduction

In December 2006, measurements on the MEXICO wind turbine were carried out in the Large Scale Low Speed Facility (LLF) of the German Dutch Wind Tunnels (DNW) [6].

Analysis of the MEXICO experiment has been performed within the framework of IEA Wind Task 29 Mexnext. The results from this project are summarized in [7]. One of the recommendations is to perform additional tests with the still available model in the DNW.

Within the EU ESWIRP project [1] a budget became available to sponsor the tunnel time of a new MEXICO test in the DNW. The New MEXICO experiment was integrated in the EU INNWIND project as it will provide important information for the development of new high tip speed turbine concepts. Therefore a financial contribution to prepare and supervise the experiment was granted. Between June 20th and July 4th 2014 the New MEXICO experiment was carried out, illustrated in Figure 3. An overview of this experiment and its preparation is given in the current document. Since this project is the culmination of long running efforts in the field of wind energy aerodynamics, a historical review is given below.

### 1.1 Historical review

In this section a historical review is given of all endeavours which had to be undertaken to make the New MEXICO experiment reality. The lessons learned can be used in the preparation and performance of future experiments. Most efforts took place within the EU FP5 project MEXICO and IEA Task 29 Mexnext. Both projects were coordinated by ECN.

The history of the MEXICO project goes back to 1996 with a discussion between TUDelft and ECN on the uncertainties in atmospheric aerodynamic experiments [12], which were related to the stochastic nature of the atmosphere. Since a wind tunnel environment does not suffer from this uncertainty the

idea was launched to carry out measurements on a wind turbine model under controlled conditions in the largest wind tunnel of Europe, the LLF of DNW. This idea eventually culminated into a MEXICO project proposal for which a cooperation was sought with various European institutes in order to perform the experiment in an international context. After several attempts the MEXICO project was approved within the EU FP5 program with a starting date of January 1<sup>st</sup> 2001. The measurements in DNW were taken from December 6<sup>th</sup> to December 14<sup>th</sup> 2006. Thereafter the measurements were analysed in IEA Task 29 Mexnext. As a result of the analyses in Mexnext it was recommended to carry out a second experiment taking into account the lessons learned from the first experiment. This second tunnel slot was baptized into New MEXICO. Eventually the New MEXICO project was approved within the European aerospace program ESWIRP with respect to tunnel costs, after which the costs for person hours were found from a variety of other sources (i.e. the FP7 project Innwind.EU, IEA Task 29 Mexnext and ECN own funds). The New MEXICO experiment was then carried out in June/July 2014 which is almost 8 years after the first tunnel slot!

### **MEXICO, goal and participants**

The main goal of the MEXICO project was to design and build a wind tunnel model and to carry out detailed aerodynamic measurements (in particular pressure and flow field measurements) on this model in the Large Low Speed Facility LLF of the German Dutch Wind Tunnel Facilities DNW. The participants of the MEXICO project and their role are described in [6]:

- ECN, as coordinator was the first project responsible confronted with the many setbacks which occurred in the project and undertook all possible efforts to find a satisfactory solution. Apart from being the coordinator ECN also defined the functional specifications of the model, it designed the wind turbine model, and it assisted in the definition of the test matrix. Moreover ECN, together with NLR, supervised the actual experiment at DNW.
- TUDelft designed and built the DAQ system with associated software. TUDelft also carried out 2D wind tunnel tests of the blade sections.
- Technion built the wind turbine model and control.
- NLR, located on the same premises as DNW, was the interface between the DNW and the MEXICO project team. Moreover they instrumented the blades with pressure sensors, and developed post-processing software.
- DTU and CRES/NTUA performed, amongst other things, CFD calculations which gave insights on the most suitable conditions for the experiment and as such supported the definition of the test matrix. Moreover their CFD calculations helped to assess the tunnel effects.

### **Mexnext/New MEXICO, goal and participants**

The MEXICO project did not allow much analysis activities and therefore this work was undertaken in the Mexnext project. Mexnext is an IEA Task, i.e a project organized under auspices of the IEA, the International Energy Agency. It was carried out in two phases, the first phase ran from September 2008

until December 2011 and the second phase ran from January 2012 until the end of 2014. The participants (20 participants from 10 different countries) of the projects are listed in [7].

One of the outcomes of Mexnext was the New MEXICO project proposal which has been submitted to ESWIRP on behalf of the entire consortium. After approval of this proposal, the experiment was prepared by a core group of Mexnext participants (ECN, TUDelft, Technion and DTU).

### **Management issues**

It should be mentioned that the MEXICO project as well as the preparation towards the New MEXICO measurements suffered from a large amount of management problems, the solution of which caused considerable delays and high costs.

For the MEXICO project alone there was already a delay of 3 years: The original project period was from January 1<sup>st</sup> 2001 until December 31<sup>st</sup> 2003 but the actual project period had to be extended until December 31<sup>st</sup> 2006. In terms of budgets there was an overspending of more than 750 kEuro. The original budget was 2.3 MEuro including a subcontract of 310 kEuro to DNW and some 500 kEuro for hardware costs. The actual budget turned out to be slightly above 3 MEuro. The overspending was carried by the participants own funds (mainly ECN and Technion). Some important reasons for the delays and overspending were (apart from some technical issues which are explained in [6]):

- MEXICO started with a bankruptcy of the industrial partner Aerpac which led to a hold from the EU until another industrial partner was found. Aerpac role was then taken over by Polymarin which went bankrupt as well. After a long period of negotiations the project continued without industrial participants.
- Another management issue lied on the sometimes cumbersome negotiations with DNW, since DNW initially gave a higher priority to aerospace projects by which the MEXICO project was given a tunnel slot in January 2007 only, which was beyond the (already extended) MEXICO end date of December 31<sup>st</sup> 2006. The resulting situation was considered unacceptable by the EU and eventually a tunnel slot could be given in December 2006 (just before the end date of the project).
- Another important delay was caused by an accident during transportation of the wind turbine model from Technion in Israel to the DNW wind tunnel in the Netherlands see Figure 1 and 2. The model suffered from severe damage and the necessary repairs were very time consuming and costly for Technion and the other partners. Although these costs were supposed to be covered by the insurance, they are still not reimbursed at the time of writing this report.

After the MEXICO experiment, ECN invested much effort in making a New MEXICO experiment possible. Several attempts were undertaken to find funds in EU FP6 projects but eventually the application for the EU Aerospace project ESWIRP was successful. Unfortunately, very shortly before the submission deadline, it appeared that ECN as Dutch participant was not allowed to submit an ESWIRP proposal for a wind tunnel in the same country. This problem could be solved (within the very few days left) through the



Figure 1: Damage to wind turbine model



Figure 2: Damage to wind turbine model

cooperation with DTU which, as non-Dutch participant, was willing to take over the role of coordinator and submitted the proposal. A next problem was given by the fact that ESWIRP funded tunnel time only. Person hours for the experiment (not only from ECN but also for TUDelft and Technion) were at long last found from the FP7 project INNWIND.EU, the above mentioned Mexnext project and ECN own funds. Moreover TUDelft offered free wind tunnel time in their LST tunnel in order to measure the aerodynamic performance of the MEXICO blade under non-rotating conditions and to check the instrumentation and data acquisition which had to be revived after more than 7 years. All in all these management problems were successfully overcome and resulted in an excellent database for both the MEXICO and New MEXICO experimental campaigns.

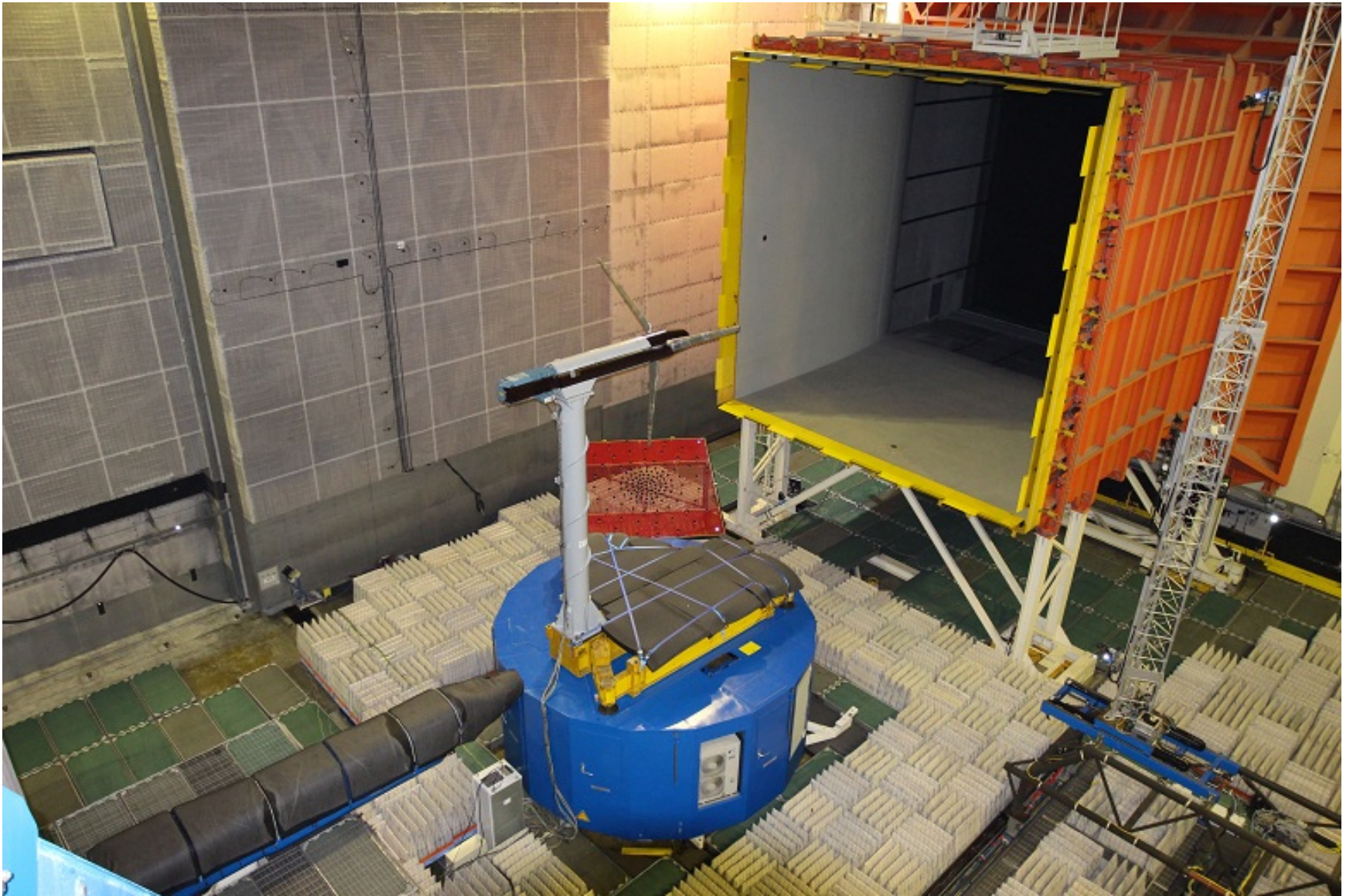


Figure 3: The New MEXICO experiment



# 2

## Objectives

The main objective of the test is to progress aerodynamic (and acoustic) modelling of wind turbines and wind turbine farms. Associated with this comes a reduction of the large uncertainty bands resulting from design loads and yield calculations. Consequently this work contributes to a reduction of the Cost of Energy (CoE) of wind power plants in general. In line with this is the possibility to apply and study innovative features in controlled conditions, also to reduce the CoE of wind energy.

Below this general motivation, a number of priorities can be distinguished, partly based on the analysis of the previous test campaign in Mexnext [7]. These priorities are discussed below.

### 2.1 Outstanding Mexnext research questions

The most important question arising from Mexnext concerns the relation between measured loads and velocities. Both CFD codes as well as lifting line methods (with input of sectional aerodynamic coefficients) overpredict the loads compared to the measurements. Please consult [7] for more details. In addition to overprediction of the loads, the velocities are (against expectations) overpredicted as well in comparison to the experiment. Loads and velocities are coupled through mass and momentum conservation, which means that a higher loading should result in an increased rotor induction and hence lower velocities. Since all simulations obey the conservation laws in unbounded flow, the question remains why the measurements do not.

### 2.2 Validate and compliment first MEXICO campaign

To preserve the validity of the previous dataset and validate the settings of the new measurements, part of the previous measurements must be reproduced. Regarding the PIV measurements, the radial and axial traverses for axial flow conditions suffice for this purpose.

In addition to that the current database should be complimented with the following items.

- Standstill measurements

The measurements for a parked rotor in the previous experiment have not produced usable results, possibly due to a malfunction of the PCB connection at large pitch angles. This dataset should be rerun, taking care that the PCB's are working correctly. Several new azimuth and yaw angles in standstill are added in agreement with IEC load case definitions. These should provide validation material for challenging load cases including radial flow.

In addition to that, (balance) measurements at various speeds should be taken without the blades installed to allow a more accurate estimate of the rotor axial force from the balance.

- Dynamic inflow

The previous experiment involved both pitching steps (up and down) and rotational speed ramps. Unfortunately the setting of the pitch angle gave an overshoot and probably has been much slower than the target of 0.05 s from  $-2.3^\circ$  to  $5^\circ$ . Because the pitch angle position was not monitored in time, the data set is not suitable for simulation purposes. The rotational speed ramps did not show a dynamic inflow effect. Both pitch and rotational speed experiments need to be re-performed to obtain dynamic inflow data sets suitable for simulation purposes. A pitch angle monitoring system needs to be installed for this purpose.

- PIV of inboard rotorplane sections

Unfortunately the previous PIV measurements did not cover the sections inboard from 1.2 m span, due to the reduced field of view of the sheets. In addition to that, laser sheet reflections from the nacelle prevented valid measurements in this region. Covering the nacelle with a laser absorbing paint and a doubling of the field of view in radial direction compared to the first campaign should allow to capture the inboard flow fields as well.

- Tailored azimuth step for PIV radial traverse

To check the azimuthal variation of flow velocities, the previous discretization angle of  $20^\circ$  azimuth was not ideal for tracking this variation around the blade passage. Based on CFD, an estimate is made of the azimuth angle discretization necessary to properly capture the azimuth average velocities. This resulted in 13 non-equidistant angles per radial traverse, which allows both monitoring of wake convection and determination of azimuthal averages. Because the blade will reflect the laser around its passage through the sheet and possibly damage the cameras, the rotorplane at  $x=0$  m cannot be visualized and the sheets are displaced a few centimeters in axial direction.

- Compliment measurement instrumentation

Based on the experience from the first test campaign, some extra measurement instrumentation/signals were added.

- Pitch angle

As mentioned above, it is necessary to measure the pitch angle with sufficient temporal resolution in order to be able to reproduce the measurements involving a pitch step.

- 1P sensor  
The 1P sensor from the previous campaign was judged to be not accurate enough to trigger the phase locked PIV measurements with less than a degree accuracy. Hence a new sensor will need to be implemented.
- Accelerometer  
Although the model is assumed to be rigid, and visual inspection confirmed this hypothesis, it would be useful to double check this especially for the dynamic inflow runs.
- Strain gauges  
The strain gauges from the previous campaign did not give correct results [8]. Since this is judged to be an important part of the measurements, allowing us to differentiate between the blades and make a comparison to balance and pressure measurements, it was decided to install new flap- and edgewise strain gauges at the blade roots.
- Generator torque  
Unfortunately time and resource constraints did not allow for application of a torque meter that measures aerodynamic torque directly. However, the ABB control cabinet measures the generator/motor torque as applied by the control system.
- Inclinometer  
To be able to distinguish between different azimuth angles during the standstill measurements, an inclinometer is needed.

Please check section 3.2 for more details on the implementation of this instrumentation.

## 2.3 Additional priorities

In addition to the reproducing and complementing the previous database, several new measurements are to be taken.

- Influence of roughness strips on performance and loads  
The blades of the previous experiment were tripped using zig-zag strips. In addition to ensuring transition to turbulent flow, a side-effect of these strips is to increase the thickness of the boundary layer (due to the thickness of the strips themselves). This side-effect can result in an extra decambering of the airfoils. The unknown significance of this contribution has resulted in the desire to perform non-tripped measurements. Although the experimental Reynolds numbers generally are above  $3 \times 10^5$ , it is kept in mind that allowing natural transition also comes with uncertainties (e.g. laminar flow separation phenomena).
- Acoustics  
The large open test section of the DNW-LLF is often used as an acoustic test facility and includes acoustically treated walls to minimize reverberations. Because the aerodynamics of the MEXICO turbine is extensively mapped, this test program provides an unique opportunity to simultaneously measure

aerodynamics and acoustics. Since commercial wind turbine noise is largely driven by the blade aerodynamics, this allows improving the knowledge about the relation between the two. Noise generation mechanisms (both self-noise and inflow noise) and also noise directivity studies can be subject of investigation.

- Blade add-ons

A requirement of the ESWIRP grant was to provide an innovative feature to the test. It was decided to apply Guerney flaps to the inboard part of the blade, which allowed to map the aerodynamic performance of these in comparison to a reference data set. Delft University of Technology was responsible for design and application of the flaps. In addition to that blade spoilers and serrations were designed and applied by ECN, to increase yield and reduce the aerodynamic noise respectively.

# 3

## Test set-up and preparations

The test set-up has been examined thoroughly prior to the first MEXICO project. This set-up including apparatus has been described in [8]. The test set-up has been the same as the first campaign, except for the acoustic lining that was added to the tunnel floor. In addition to that, the external balance was covered with foam padding to prevent noise from the tunnel jet shear layer possibly impinging on the balance. An acoustic array was positioned between nozzle exit and the model, below the jet. Within Mexnext, the tunnel calibration from the first campaign as determined and used by the DNW has been point of discussion. Therefore it is chosen to perform an empty tunnel calibration prior to the tunnel test again. To verify the tunnel calibration it was decided to perform a test with the model in parked conditions and a pitot tube mounted between the blades. This allowed to check the incident velocity in the rotor plane and validate the PIV system which was also used in this configuration.

The remainder of this section discusses model and instrumentation issues in section 3.1 and 3.2. Section 3.3 is especially dedicated to the pressure sensors and its data acquisition system, which was subject of investigation in the LTT tunnel of Delft University prior to the rotating tunnel test.

### 3.1 Wind turbine model

Technion has published a detailed description of the model in [2, 3]. Several points needed to be addressed before entering the wind tunnel.

The basic functionality was checked successfully after the model was stored for more than 7 years. The pitch actuator and speed controller deserved special attention in this respect to perform successful dynamic inflow measurements. Firstly the pitch angle setting has to be monitored in time (see also section 3.2). An attempt was made to increase both pitch speed as well rpm acceleration. Unfortunately it appeared to be impossible to improve the second feature. The first however was improved significantly to

a higher pitching speed, whereas this was around  $10^\circ/\text{s}$  for the first campaign.

The roughness strips from the previous experiment were removed to facilitate scanning of the shape of the blades, which was performed within Mexnext. To reproduce the previous experiment, identical strips had to be applied at the same location. The roughness configuration from the first test campaign was applied by Delft University of Technology as accurate as possible.

Rhodamine was spray painted onto the nacelle of the turbine by DNW, to make sure that laser sheet reflections would not corrupt the PIV measurements.

## 3.2 Measurement apparatus

Based on the experience from the first test campaign, some extra measurement instrumentation/signals were added. The MEXICO data acquisition system was extended with 16 more signals to 176 channels to allow for adding the extra signals mentioned below.

- Pitch angle

For this purpose a potentiometer was installed which measures the position of the linear actuator, that drives the pitch angle setting. This analog signal is connected to the overall MEXICO data acquisition that samples data at 5kHz. A static calibration between  $-5^\circ$  and  $90^\circ$  is performed to correlate this signal to the 'true' pitch angle as displayed by the Technion control system. Unfortunately exporting the latter signal directly to the MEXICO data acquisition appeared to be not an option due to possible introduction of noise into the control system.

- 1P sensor

DNW has implemented an optical 1P sensor, which gives an up- and down going pulse at specified azimuth angles. The signal was connected to the MEXICO data acquisition system, as well as exported to the DNW system to allow triggering the phase locked PIV measurements.

- Accelerometer

An accelerometer which measures acceleration in all three direction was installed in the nacelle. The accelerometer also measures 'static' acceleration, hence it also measures gravitational, which can be used to detect angle misalignments. The signal was connected to the MEXICO data acquisition system.

- Strain gauges

The blades were instrumented with new gauges by dedicated ECN personnel. A calibration was performed prior to the test. In addition to that an idling run at 3 rpm without wind was performed at the beginning and end of the test at 3 different pitch angles ( $0^\circ$ ,  $45^\circ$ ,  $90^\circ$ ), to allow for identification and correction for drift. Similar as for the first campaign, the six strain gauges signals were connected to the MEXICO data acquisition system.

- Generator torque and HSS rpm

The generator torque is exported from the ABB power cabinet to the MEXICO data acquisition. Un-

fortunately a distinction cannot be made between a driving and generating situation, which means adding a plus or minus will have to be part of the data reduction process. To estimate the generator/mechanical losses, blade off measurements without wind have been performed at 324 and 424 rpm. Unfortunately these machine characteristics were not supplied by ABB. In addition to exporting the generator torque, the High Speed Shaft (HSS) rpm was exported from the ABB controller to the MEXICO data acquisition.

- Inclinator

An inclinometer was installed in the nacelle between the rotating and non-rotating part. Similar to the above signals, this signal was connected to the MEXICO data acquisition.

In addition to that, the DNW measurement apparatus was extended in comparison to the previous campaign. Apart from averaged quantities, more statistics (standard deviation, minimum, maximum) of the tunnel related quantities and balance data will be saved. For the velocity verification test, a pitot connected to pressure measurement system was used. The PIV measurement system has changed, of which the increase of the camera resolution is most important. Keeping the spatial resolution identical to the previous campaign, the field of view has increased from 337x394 mm to 380x610 mm in axial and lateral direction respectively.

For the acoustics, both side wall microphones as well as an acoustic array were used. The averaging time needed to guarantee reliable acoustic results exceeded the averaging time of the MEXICO data acquisition system, which amounted to 5s (approximately 35 rotations at 424 rpm). This is due to the required resolution at lower frequencies in combination with the necessary correction for shear layer refraction for acoustic propagation through the open jet shear layer. To compromise, the most important acoustic runs were selected at an average time of 60s, whereas the rest was averaged over 15s to still allow for a meaningful acoustic data point for each pressure data point.

A separate section below has been dedicated to the verification of the pressure sensors and their corresponding data acquisition.

### 3.3 Verification of pressure sensors and data acquisition

To check whether the pressure sensors and data acquisition embedded in the three blades are still functioning as desired, a test in the Delft University Low Speed Tunnel was performed. A calibration of the pressure sensors is performed as well. Firstly an estimate is made of the uncertainty of the sensors.

#### Uncertainty

The interpretation of the sensor specification sheet A for the MEXICO situation has been clarified by the Dutch distributor of Kulite® [10]. From the specification sheet, the uncertainty of the sensors is correlated to the the Full Scale Output (FSO), which can be taken as the pressure range of 35 kPa. The residual unbalance can be taken as a possible offset, and the  $\pm 3\%$  then indicates a possible offset of  $\pm 1050$  Pa. Bearing this in mind it is a good choice to perform zero measurements. The combined non-

linearity and hysteresis are estimated at a  $\pm 0.25\%$  FSO from the best fit straight line (BFSL). However the non-linearity is expected to be negligible if zero measurements are applied, because the linearity is only applied to the relatively small differential pressure from atmosphere. In that case only the hysteresis of less than  $0.1\%$  FSO or 35 Pa remains. In addition to that there is the repeatability estimated at around  $\pm 0.25\%$  FSO or 35 Pa.

Also on the specification sheet is the thermal zero and sensitivity shift. Where the offset again is corrected for by the zero measurement, the sensitivity of  $\pm 1\%$  per  $55^\circ\text{C}$  can influence the pressure readings. However since the sensitivity is only used in a differential way (with respect to atmosphere), the absolute error stays low depending on the dynamic pressure. Combining the above information, the resulting uncertainties for the different radial stations are summarized in Table 1. The results indicate that for the

Table 1: Estimated maximum uncertainty based on specification sheet

r/R [%]	25	35	60	82	92
rpm [rpm]	324	424	424	424	424
$U_\infty$ [m/s]	15	15	15	14	15
1 Cp <sup>‡</sup> [Pa]	311	810	2262	4172	5235
Resulting maximum uncertainties					
Repeatability [Pa]	35	35	35	35	35
Hysteresis [Pa]	35	35	35	35	35
Thermal <sup>†</sup> [Pa]	1	3	8	15	19
Total <sup>†</sup> [Cp]	0.23	0.09	0.04	0.02	0.02
Cn <sup>∓</sup> [-]	0.46	0.18	0.07	0.04	0.03

<sup>‡</sup> Estimating axial induction factor of 0.2 for 25% and 0.33 for the other sections

<sup>†</sup> Assuming difference of  $20^\circ\text{C}$  between calibration and operation temperature and a pressure differential of 1 Cp from atmosphere

<sup>∓</sup> Resulting uncertainty in normal force coefficient assuming the worst case scenario of the suction side pressure uncertainties showing the opposite sign of the pressure side ones

inboard sections the accuracy of the sensors is rather poor, judging by a maximum uncertainty in terms of Cp of 0.23 at the 25% section at 324 rpm. Assuming the worst case scenario of the suction side pressures showing a different sign than the pressure side ones, this could lead to differences in normal force of up to 0.46. Nevertheless the good agreement between pressure readings taken at the same conditions during the first campaign do not point in this direction. The good agreement between the readings taken at different rotational speeds (but equal tip speed ratios, see also [7]) gives further confidence in this observation. At least the uncertainties due to repeatability seems less than the maximum assumed in Table 1. In addition to that, Daniel Micallef [4] has compared the cross checking of sensors which were placed at identical radial, chordwise and flapwise location but at different blades. The level of disagreement between results of the different blades turns out to be small. The slight differences could also be caused by a geometrical offset, i.e. slightly different position of the sensor.

## Calibration

A proper calibration should include the whole data acquisition chain. The sensitivity of the sensor should be checked by applying a number of known pressures. A pressure or climate chamber that allows placement of a full blade is favourable for this purpose. Since this is not available, a steel tube is used that fits a blade. One side of the tube is welded air tight, the other side is closed with a plastic foil and tacky tape. This means that only below atmospheric pressures are taken, since positive pressures would blow up the package. It is beyond the scope of the current report to go into detail and discuss the set-up, instrumentation and results. Below a summary of the results is given.

Figure 4 illustrates the sensitivity differences compared to the specification sheet values. The correlation of the least squares fit was calculated to exceed 0.9999 for all sensors except for four sensors which however still featured values above 0.996. A consistent sensitivity increase roughly between 5% and 10% can be observed. A valid question is whether the sensitivity difference can be attributed to the fact that the specification sheet values are different from the in-situ values including the whole data acquisition chain, or the difference arises from the sensors ageing over time. Although the Kulite® distributor has indicated that it is possible that the sensor specifications may vary over time, an order of magnitude is not given. However, it is acknowledged that it is especially the offset that may vary in time rather than the sensitivity [10]. Since offset is excluded during the experiment by subtracting the zero runs, it is not likely that the sensors would give a different value over time.

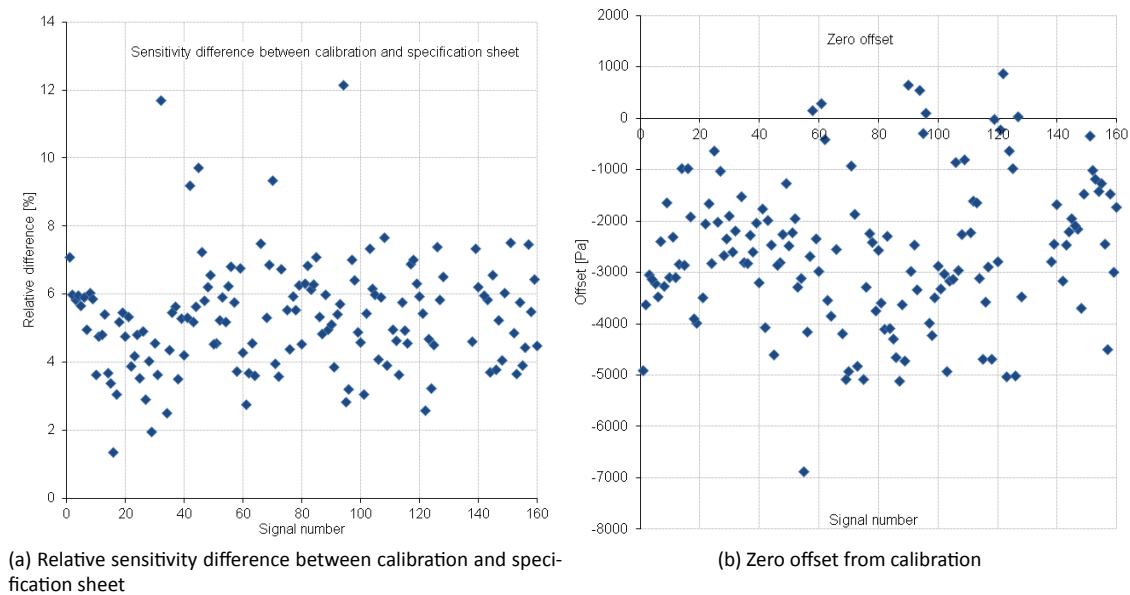


Figure 4: Illustration of calibration results as a function of signal number

To estimate the effect of the different sensitivity on the experimental values of the first campaign, the new sensor values have individually been taken into account in the chordwise and spanwise integration.

The results for three standard load cases at 424 rpm and a pitch angle of  $-2.3^\circ$  and are given in Table 2.

Table 2: Relative increase of loads due to calibration, 424 rpm, pitch= $-2.3^\circ$

	$U_\infty=10$ m/s		$U_\infty=15$ m/s		$U_\infty=24$ m/s	
Fax [%]	6.6		6.6		7.0	
Torque [%]	3.7		4.9		3.9	

	F <sub>n</sub> [%]	F <sub>t</sub> [%]	F <sub>n</sub> [%]	F <sub>t</sub> [%]	F <sub>n</sub> [%]	F <sub>t</sub> [%]
25%R	5.2	12.4	5.5	7.5	5.3	6.8
35%R	4.3	11.8	4.4	5.1	4.3	4.9
60%R	6.0	15.5	6.0	7.0	6.0	6.4
82%R	5.2	1.4	5.1	5.1	5.0	5.9
92%R	4.6	6.0	4.9	6.1	5.2	6.0

‡ F<sub>n</sub> denotes normal and F<sub>t</sub> tangential force

† Fax denotes the rotor axial force and Torque the rotor torque. These are obtained by linear integration of the radial force distribution along the blade span, assuming zero load at root and tip.

## Tunnel test

The blades were mounted in the TUDelft Low Speed Tunnel. In addition to checking the status of the blades and its instrumentation, this test also enabled the measurement of quasi-standstill sectional characteristics. Also the effect of tripping the boundary layer could be investigated. The tunnel features an octagonal cross section of 1.25 m high by 1.8 m wide, in which the blades are positioned vertically pointing downward. Since the blade length of 2.04 m exceeds the tunnel height two configurations were employed, one focusing on the outboard part (with a free tip) and one on the inboard blade part (with the tunnel floor cutting off the 69%R section), see also Figure 5. With a maximum tunnel speed of 100 m/s, the Reynolds numbers of the rotating experiment could be matched. Both clean and rough conditions were subject of investigation, where the rough configuration was identical to the MEXICO experiment.

The data acquisition and pressure sensors were brought back to life successfully after an inactive period of more than seven years. Having a close look at the apparatus allowed for fixing some of the pressure signals in the inboard sections which were faulty during the first MEXICO campaign. A wake rake was positioned downstream of the blade to measure the velocity deficit. In addition to obtaining sectional drag, traversing the rake along the blade span for all three blades gave a possibility to further investigate the agreement between the blades.

## Sectional characteristics

Using the ECN Aero-Module free vortex wake code AWSM, a first survey was performed to investigate the angle of attack variation along the blade using prescribed airfoil data. By this approach an estimate of the degree of 'two-dimensionality' of the experimental set-up can be obtained. Although full details



Figure 5: Test set-up in the Delft tunnel

such as wall effects are not taken into account here, this approach yields an approximation for the order of magnitude of the induced velocities causing different inflow angles than the local geometric twist angle. The results shown in Figure 6 reveal that for this particular blade pitch angle induced angles of attack exceeding  $2^\circ$  can be expected, not only confined to the tip area. Hence the trailing vorticity is not only concentrated in the tip vortex but also plays a role in the remainder of the span due to the varying circulation along the blade span as a consequence of the radial twist and chord distribution. Increasing or decreasing the blade pitch angle from this value is found to reduce the induced velocities. For the  $15^\circ$  pitch angle, the geometric angle of attack along the blade in combination with the chord distribution results in a circulation distribution where the trailing vorticity is most effective in inducing velocities perpendicular to the chordline. Although it is clear that the test set-up cannot be used to determine sectional characteristics directly, the set-up can be considered comparable to parked rotor conditions. Combining the measurements with planned CFD simulations including the tunnel will possibly reveal information on the underlying two dimensional sectional characteristics.

The deduced sectional characteristics as a function of **geometric** angle of attack for the various sections are subject of the paragraph below. Here it must be noted that no tunnel correction was applied. Also,

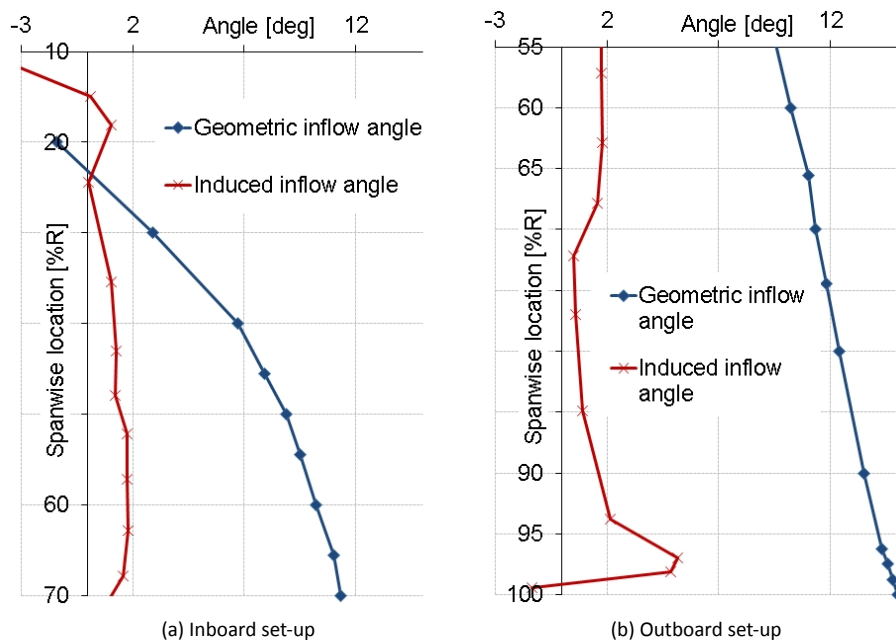


Figure 6: Calculated induced angle of attack variation for a geometric tip angle of  $15^\circ$

the application of zero measurements to correct for sensor drift needs to be looked at more closely. In addition to the test results, the (tunnel corrected) two-dimensional wind tunnel test results as supplied in IEA Task 29 Mexnext are included for comparison as well.

Referring to the uncertainty approximation from Table 1, it is clear that for the inboard section the low operational dynamic pressure for the rotating case hampers an accurate measurement. This is clearly illustrated in Figure 7, where the distribution becomes more smooth for increasing tunnel speed. The undisturbed tunnel speeds range from 20 m/s at  $Re=0.3 \times 10^6$  to 60 m/s at  $Re=0.9 \times 10^6$ . It can also be observed that the unexpected increase in suction level at the trailing edge (suction side), which was also noticed in the first rotating campaign, disappears at the higher tunnel speeds. This indicates that, unless this is a Reynolds number effect, we are not dealing with a physical phenomenon but an accuracy effect.

The deduced lift and drag curves for the 25%R section are displayed in Figure 8 for a Reynolds number of  $Re=0.5 \times 10^6$ . The effect of roughness can be clearly distinguished for both lift and drag and is rather large. Comparing to data from two-dimensional profile testing shows a different lift slope and drag curve position, which can be explained by the three-dimensional test set-up and the close proximity of this section to the blade root. The same picture for the 35%R section is displayed in this Figure as well. Here it must be noted that since the profile shapes at 35%R and 25%R are identical, if the set-up would have been purely two-dimensional, the results from 25%R and 35%R would have to coincide. Due to the three-dimensional set-up, it can be observed that this is clearly not the case. Again the difference between clean and rough conditions is considerable. Because this section is located further from the blade root, the measured lift curve slopes agree much better with the two dimensional sectional data.

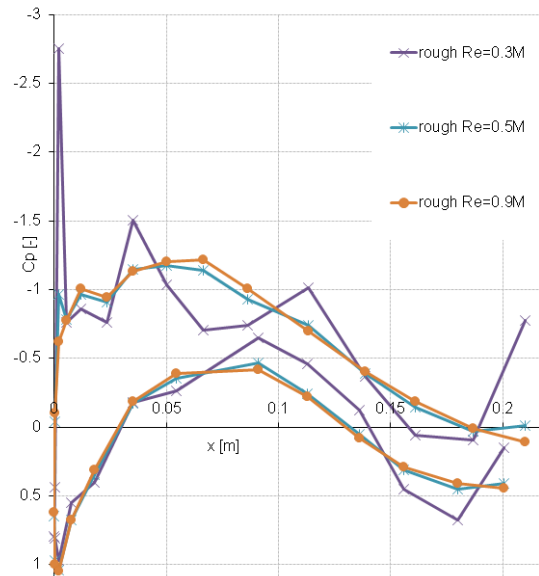
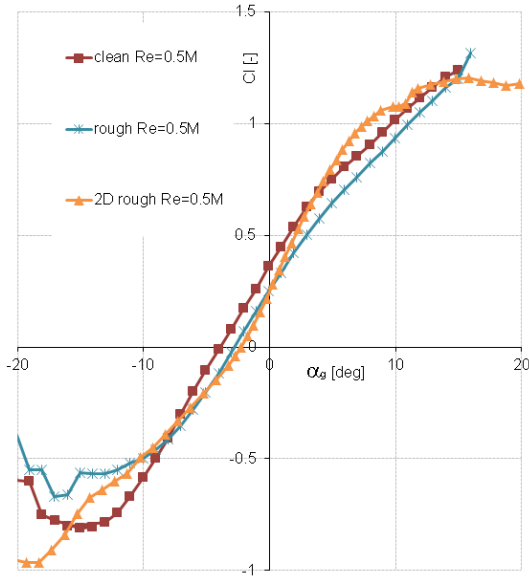


Figure 7: Pressure distribution at 25%R for different Reynolds numbers,  $\alpha_g = 4.95^\circ$

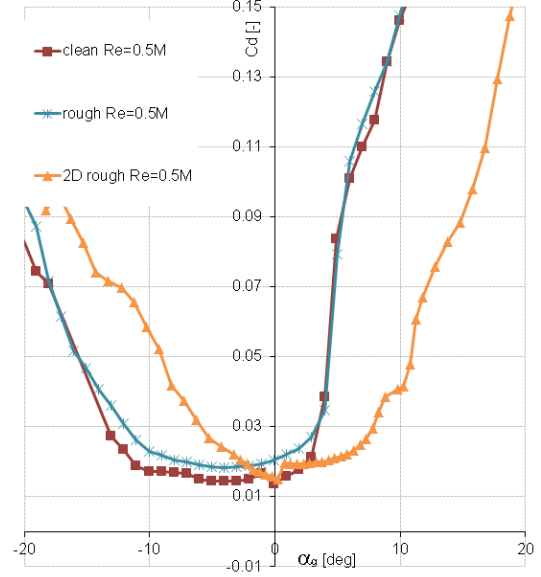
For the 60%R section, the results are displayed in Figure 9. Here only results are available for a rough configuration. The lift offset from the two dimensional characteristics often exceeds  $\Delta Cl=0.2$ . The lift curve slope is also slightly smaller. Whether this offset originates from the three-dimensional set-up, a misalignment in angle of attack setting or the Reynolds number difference can be subject of further investigation. Where the two dimensional data from the inboard and outboard profiles originate from the same wind tunnel, the sectional data from the midboard profile was obtained in the VELUX wind tunnel [11]. It is surprising to see that the drag levels are lower for the two-dimensional data, since the VELUX tunnel is known to feature a high turbulence intensity. Probably this is caused in part by the higher Reynolds number of the two-dimensional test, which flattens the surface boundary layers and results in higher lift and lower drag levels.

For the 82%R section, the results are displayed in Figure 10. The difference between clean and rough conditions can be observed again as change in lift curve slope and a difference in the minimum drag levels. The two-dimensional data shows a higher lift and lower drag compared to the rough configuration. Although the differences (especially in the lift) are smaller here, the same was observed for the 60%R section and similar considerations apply towards the reasoning behind this difference. The 92%R section results from Figure 10 show a similar trend as for the 82%R section. Just as for the 25%R section the lift curve slope is considerably smaller than for the two-dimensional data, due to the proximity of this section to the blade tip.

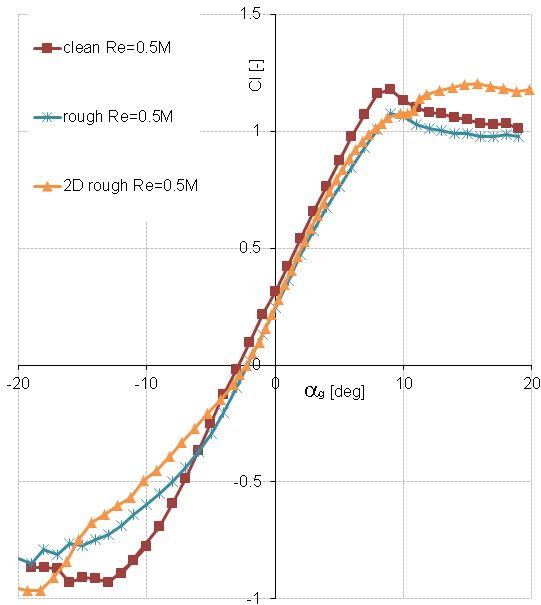
The promising initial results from this test are just a first taste of the full data set obtained. This data can be used for future research into standstill aerodynamics, influence of rotational effects, Reynolds number effects, transition etc. The obtained pressure distributions can be compared to the distributions



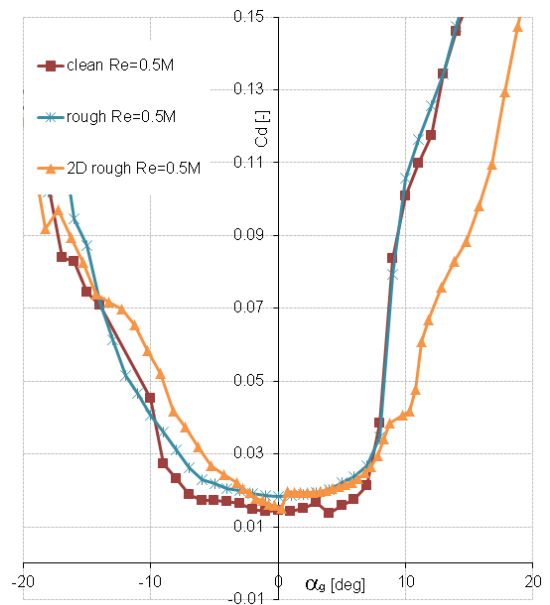
(a) 25%R lift



(b) 25%R drag



(c) 35%R lift



(d) 35%R drag

Figure 8: Comparison of measured sectional characteristics for the 25%R and 35%R section

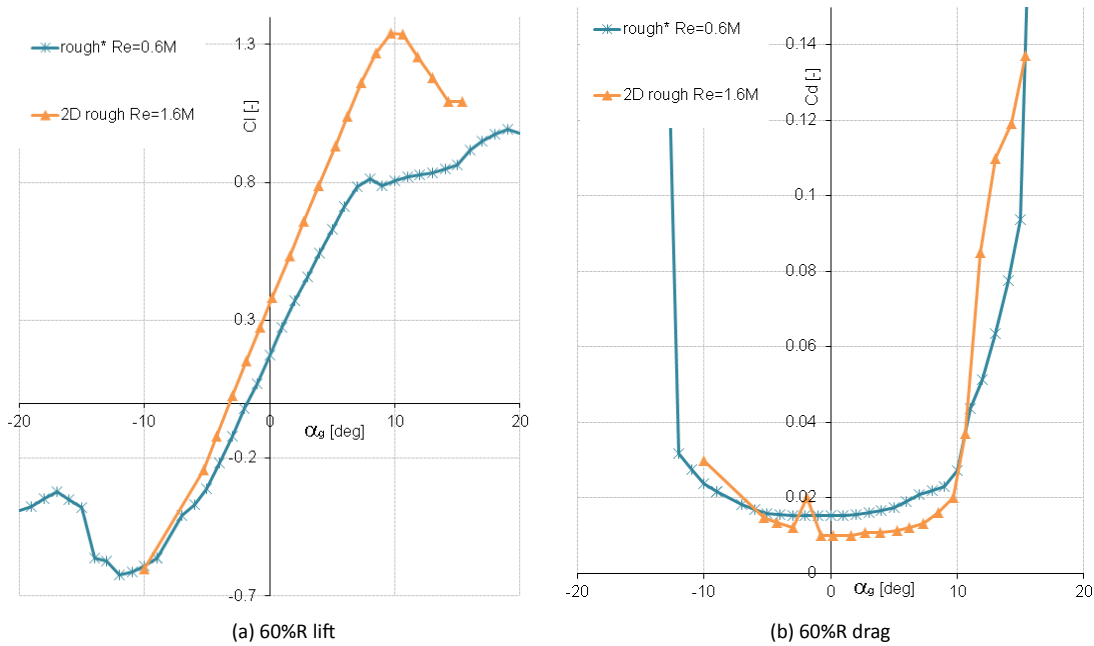


Figure 9: Comparison of measured sectional characteristics for the 60%R section

from the rotating experiment and the two-dimensional data. In addition to the sectional data, the wake rake was traversed along the span to measure drag variation as a function of radius. The Mexnext task is a suitable platform for coordinating these efforts.

### Flow visualization and stethoscope

A stethoscope was traversed over the blade surface to determine the location of laminar to turbulent transition along the blade radius. In a clean configuration, small surface irregularities (mainly compartment edges) were found to influence the exact chordwise position of transition along the span. Although this is regarded as unwanted taking into account comparison to CFD calculations, the effect of parasitic drag due to the strip itself (which is not included by CFD simulations unless the actual strip is modelled) is judged to impose a larger uncertainty in the computations than the first effect. Therefore it was decided to perform the rotating New MEXICO test with the outboard sections (NACA profile) in a clean configuration. Because the inboard sections feature a relatively low onset velocity in combination with the occurrence of separated flow and rotational effects, it was chosen to keep the tripping in place to prevent laminar separation phenomena.

To minimize the parasitic drag due to the strip itself, an attempt was made to determine the minimum width and thickness of the zigzag strip to yield transition for the operational range of angles of attack and Reynolds numbers. This resulted in a configuration featuring strips with a width of 5 mm and unchanged thickness of 0.2mm. The chordwise position of the strips was kept at 10%chord for both pressure and suction side of the blades. The zigzag strips positioning close to the pressure sensors were modified in

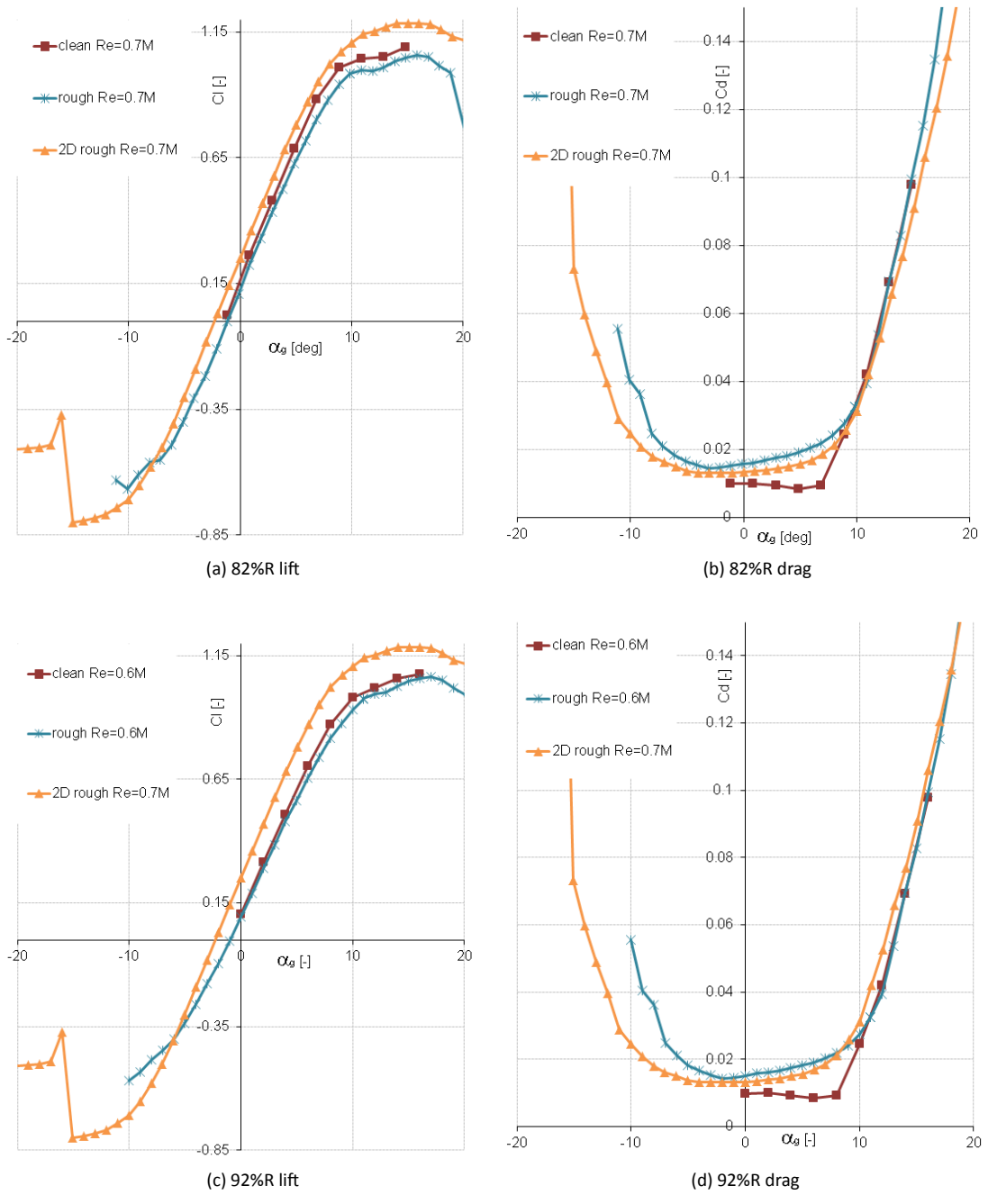


Figure 10: Comparison of measured sectional characteristics for the 82%R and 92%R section

such a way that distortion of the measured pressure distribution by local pressure changes due to the small vortices emanating from the zigzag shape was prevented. The resulting sectional characteristics were shown to closely match the characteristics of the 'old' strips featuring a 10 mm width. Therefore, and also for the sake of repeatability verification, the same strips as for the first campaign were chosen to be applied in New MEXICO.

An oil flow visualization in the set-up for the outboard part of blade 3 confirmed that the roughness strips indeed provoke transition. Figure 11a shows laminar to turbulent boundary layer transition (directly aft of the zigzag strip), illustrated by the light and respectively darker colours due to the different friction coefficient between them. The difference with the tip region which does not feature a zigzag strip is clearly noticeable. The tape covering the sensors at 60%R, 82%R and 92%R can be observed from top to bottom respectively. Due to the twist distribution, the geometric angle of attack is  $4.8^\circ$ ,  $2.4^\circ$  and  $1.2^\circ$  larger for these sections respectively than the tip angle. Because of this the outboard sections already exhibit trailing edge separation, which can be observed by the bright colours due to the oil not being transported over the surface. Generally speaking the flow pattern can be considered two-dimensional. Figure 11b then shows a configuration at a higher tip pitch angle, where spanwise flow features can be observed in the separated flow region. In addition to that a small laminar separation bubble can be observed by a bright coloured line before the roughness strip just aft of the leading edge, approximately between the tip and 70%R. Figure 11c shows the lower side surface for a negative angle of attack, where the midboard part of the blade shows separation in the cusp of the RISØ profile.

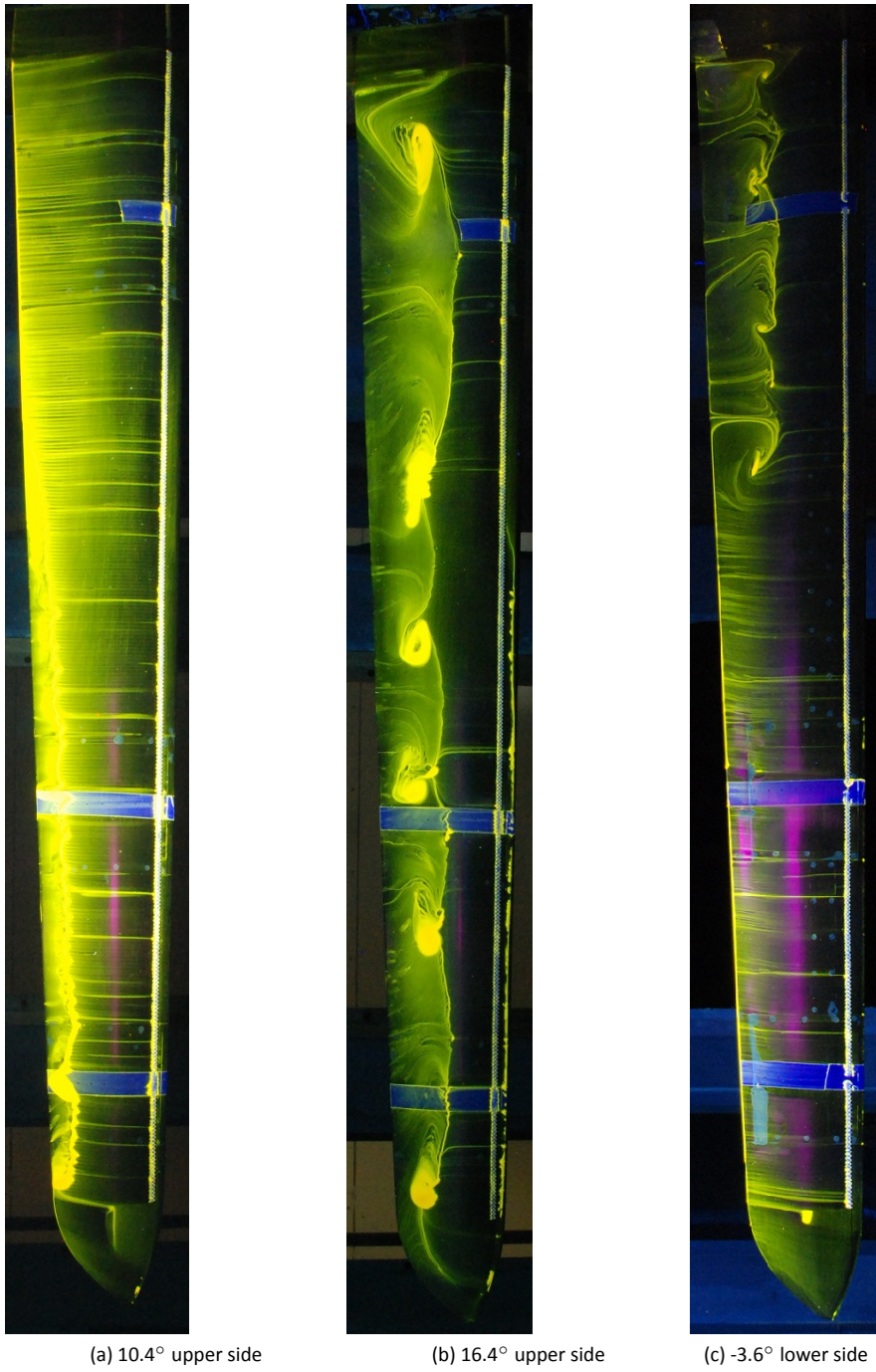


Figure 11: Blade oilflow visualization for a variety of geometric angles of attack referenced to the tip chord (flow from right to left),  $U_\infty=60$  m/s

# 4

## Test matrix

The test matrix is summarized in Table 4. The column ordering largely follows the test schedule in chronological order. The first rows indicate which measurement apparatus has been used for each part of the test. The model configuration describes whether roughness, add-ons or other features have been applied to the model. A clarification for the given numbering is given in Table 3. The operational condition gives an overview of the pitch angles, yaw angles, rotational speed and tunnel speeds that have been applied for each part of the test.

Table 3: Model configuration legend for New MEXICO

Legend number	Configuration
0	Roughness on full blade
1	Guernsey flaps long
2	Guernsey flaps short
3	Outboard blade clean
4	Spoilers
5	Serrations
6	Pitch misalignment B2 (-20°)
7	Oil flow: sensors taped off
99	Blade off

Table 4: New MEXICO test matrix overview

Test type	Velocity verification	Loads vs velocity	Standstill	Axial flow (pressure)	PIV	Dynamic inflow	Yawed flow (pressure)	Blade add-ons	Pitch misalignment	Flowviz	Blade-off	
	DEMO	x	x	x	x	x	x	x	x	(x)	(x)	
	Balance	x	x	x	x	x	x	x	x	x	x	
Apparatus	PIV traverse	(+ pitot) radial	axial radial		axial radial							
	Mics Array	x	x	x	x	x	x	x	x	x	x	
		x	x	x	x	x	x	x	x	x	x	
Model config <sup>†</sup>		0	0	0, 3	3	3	3	3	1, 2, 4, 5	3, 7	6	99
	Pitch angle [°]	90	-5.3→1.7	-2.3→90	-5.3→1.7	-2.3	-2.3 Steps	-2.3,0.7	-5.3→1.7	-5.3→20	-2.3, 73.6	NA
Operational condition	Yaw angle [°]	0	0	-90→+30	0	-30,0,30	0,15,30	-30→+45	0	0	0	-30→+30
	Rot. speed [rpm]	0	324,424	0	324,424	424	324,424 Ramp	424	0,324,424	324	0,324,424	0,324,424
	$U_{\infty}$ [m/s]	10→30	7.5→24	30	5→30	10,15,24	10,15,18	10,15,18,24	5→30	-5→15	15,18,30	10→30

<sup>†</sup> Legend clarification in Table 3

After the tunnel calibration (empty tunnel), the model was transferred to the test section. A velocity verification was performed with blades pitched to vane, using both a pitot tube as well as PIV measurements (see also section 5.1). Then a repeat of several pressure and PIV runs from the first MEXICO campaign was performed, which together with the velocity verification provided answers towards the discrepancy of the loads-velocity relation from momentum theory.

With the roughness strips still applied to the full span of the blades, a standstill test was performed at the maximum tunnel speed. This choice was motivated by the relatively low chord based Reynolds numbers for the maximum tunnel speed of  $U_\infty=30$  m/s. In addition to the pitch angle traverse in axial flow during standstill, the model was misaligned at yaw angles of  $-90^\circ$ ,  $-60^\circ$ ,  $-45^\circ$ ,  $-30^\circ$ ,  $-15^\circ$ ,  $15^\circ$  and  $30^\circ$  with the blades pitched to vane. Because in misaligned flow the blades are experiencing different inflow conditions and the sectional pressure sensors are distributed between the blades, these tests were performed at  $0^\circ$ ,  $120^\circ$  and  $240^\circ$  azimuth angles.

A full sweep through the operational regime was then performed in axial flow conditions, which included lambda traverses for both 324 rpm and 424 rpm at various pitch angles. Here the roughness strips were removed from the outboard part of the blades. To be able to compare to the rough blade configuration, also a pitch angle sweep in standstill conditions was taken for this blade configuration. An enormous amount of PIV data was acquired for this configuration, of which more details are given in section 4.1.

Several dynamic inflow runs were then performed, consisting of rpm ramps (324 rpm to 424 rpm and back) and pitch angle steps ( $-2.3^\circ$  to  $5^\circ$  and back) at various operational conditions (tip speed ratios  $\lambda=5.5$ , 6.7 and 10). Lower tip speed values were judged as non-relevant because of the low rotor induction associated with them, probably discarding a dynamic inflow effect. Since the pitch angle step change was slower than hoped for, these measurements are performed at 324 rpm as well as the default of 424 rpm. In addition to the previous MEXICO campaign the dynamic inflow runs were also performed at  $15^\circ$  and  $30^\circ$  yaw.

Pressure runs at yaw angles between  $-30^\circ$  and  $45^\circ$  and various tunnel speeds (mostly at  $-2.3^\circ$  pitch angle) were performed to study yaw effects. An  $8^\circ$  misalignment case was added because it is prescribed in the IEC load case calculations.

Several blade add-ons were tested out on the turbine. All of them featured a full sweep through the rotating operational regime, just as was performed for the clean configuration. Also a pitch angle sweep in standstill for attached flow conditions was added to deduce the effect on the 'two-dimensional' polars. Firstly Guerney flaps were applied to the blade up to 60%R, later they were cut off to extend to 46%R. Then 3D-printed spoilers were applied to the transition from the cylindrical part of the first streamlined section of the blades. The same manufacturing technique was used to produce serrations, which were designed to extend from roughly 70%R to 90%R. Unfortunately due to time restrictions only the 80%R to 90%R section was covered on the blades. An illustration of the add-ons is given in Figure 12.

For the pitch misalignment runs, the pitch angle of blade 2 was reduced by  $20^\circ$  in comparison to the other blades. The rotational speed was limited to 324 rpm to keep the instability due to the aerodynamic



(a) Guerney flap



(b) Spoiler



(c) Serrations



(d) Blade-off

Figure 12: Pictures of different MEXICO configurations

imbalance low (the nose cone could be observed to 'wobble' around a bit). A full sweep through the operational regime was performed, featuring the standard pitch angles for blade 1 and 3. In addition to that, lambda sweeps at  $15^\circ$  and  $20^\circ$  (referring to the blade 1 and 3 pitch angle) were performed.

The flow visualization contains both oil flow visualization on the blades as well as smoke visualization by application of smoke candles from the blade tips. The oil flow visualization was attempted at both rotating and standstill conditions. To save time, only blade 2 was immersed with oil. After this test the blades were removed and the holes in the nacelle were covered with tape, see also Figure 12d. The blade-off measurements were also performed in both rotating and standstill conditions, to provide information for determination of generator losses (with and without wind) as well as isolating rotor forces and moments.

## 4.1 PIV overview

An overview is given of the configuration used for the several PIV measurements is given. A distinction is made between the different parts of the test matrix. The same operational conditions were subject of investigation as for the first campaign. The PIV velocity verification configuration is not discussed here. For all given PIV sheets an average of 31 image pairs was used, which was judged to be the ideal compromise between accuracy and time based on the experience of DNW.

A sheet size of 380 mm × 610 mm in x- and y-direction respectively has been used, referring to the tunnel coordinate system from Figure 13. All sheets have been taken at the 9 o'clock position, i.e. the xy-plane at z=0 for positive y-values (tunnel coordinate system).

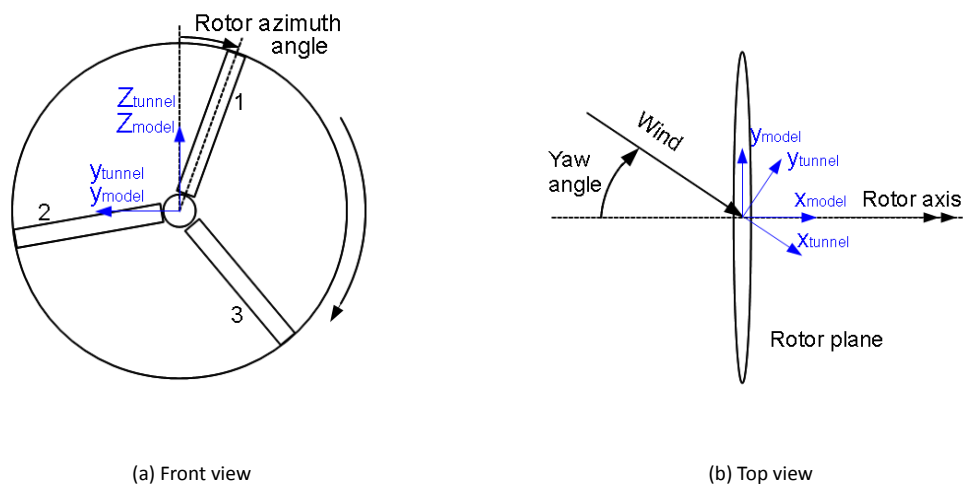


Figure 13: Definitions and conventions of the New MEXICO experiment

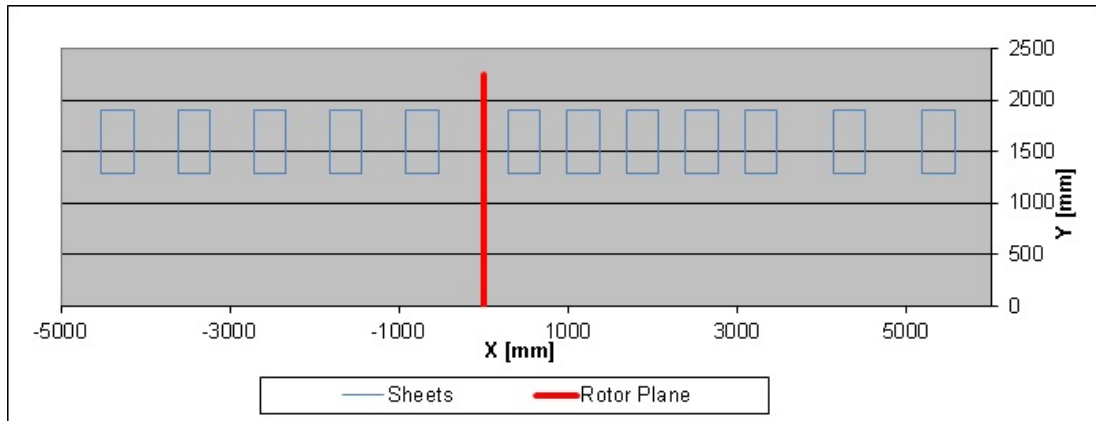
### Loads versus velocity, rough blade configuration

Both radial as well as axial traverses were performed at design conditions ( $U_\infty=15$  m/s, 424 rpm,  $-2.3^\circ$  pitch). The main purpose is to compare the results to the PIV traverse from the first campaign. They are summarized in Figure 14a and 14b. Due to the increased sheet size (especially in radial direction), only 1 instead of 2 radial locations are necessary for the axial traverse to cover both  $y=1400$  mm as well as  $y=1800$  mm. For the radial traverse, also the inboard region was included. The axial traverse was performed at a phase locked azimuth angle of zero degree, as defined in Figure 13a. Instead of using a  $0^\circ/20^\circ/40^\circ/60^\circ/80^\circ/100^\circ/120^\circ$

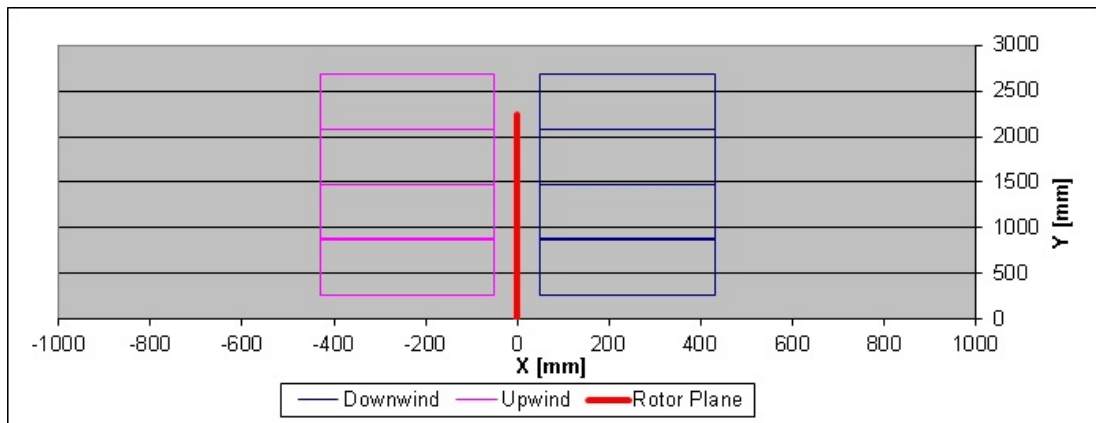
azimuth spacing for the radial traverse (as was performed for the first MEXICO campaign), it was decided to focus on the blade passage to be able to approximate the annulus averaged induction. Since blade 2 passes at  $30^\circ$ , it was chosen to use angles of

$10^\circ/17^\circ/22^\circ/26^\circ/29^\circ/31^\circ/34^\circ/38^\circ/43^\circ/50^\circ/70^\circ/90^\circ/110^\circ$

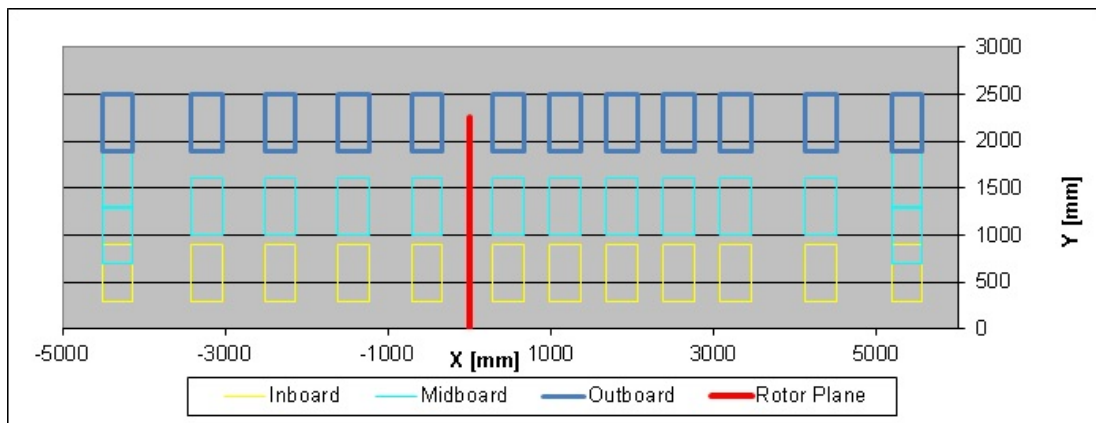
based on velocity estimates from CFD at  $x=-300$  mm and  $x=300$  mm. The disadvantage was that to pre-



(a) Axial traverse



(b) Radial traverse



(c) Momentum traverse

Figure 14: Axial flow sheet spacing

vent laser reflections from the blade, the PIV sheets had to be displaced 50 mm in axial direction away from the rotor plane. The view close to the blade passage was however judged to be more important than the missing part for the study of blade wake convection aerodynamics.

### Partly clean blade configuration

A more extensive PIV traverse was performed for the partly clean blade configuration, where the strips were removed from the outboard section. Again both radial and axial traverses were performed. Due to lack of time and the limited additional value, it was decided not to perform new vortex searches in addition to the first campaign. An important consideration here is the fact that the limited extension of sheet resolution in axial direction precludes the capture of two vortex cores within one sheet for design conditions.

#### Axial flow

For the design condition, an attempt was made to gather data for a momentum analysis using the measured flow velocities. The resulting sheet spacing is depicted in Figure 14c. Regarding the axial extent of the control volume, it is important to choose a control volume for which the pressure forces have no influence. For the inflow, a sufficient distance is needed such that streamline expansion has not yet started. For the outflow, a sufficient distance is needed such that streamline convergence has been finalized. For the upwind sheets, an azimuth spacing of  $15^\circ$  between  $0^\circ$  and  $120^\circ$  has been chosen. Downwind this spacing has been reduced to  $10^\circ$ . Special attention was paid to the outflow plane. The outflow plane is not considered uniform and a spacing of  $10^\circ$  between  $0^\circ$  and  $360^\circ$  has been chosen. The resulting configuration appeared to be extremely costly in time (approximately 4 hours testing time). For  $U_\infty=10$  m/s and  $U_\infty=24$  m/s, the axial traverse was the same as depicted in Figure 14a.

The radial traverses were performed identical for all three operational conditions as depicted in Figure 14b, using the same azimuth discretization as for the rough configuration. To study the difference between the blades, the radial traverse at design conditions was repeated to focus at the blade passage of blade 3 and 1. Thereto a similar azimuth discretization as for blade 2 was used, but now adding  $120^\circ$  and  $240^\circ$  to the azimuth angles respectively. Here only the downwind sheets were captured since, if there are differences, they are expected to appear in the wake.

#### Yawed flow

For yawed flow conditions, axial and radial traverse sheet spacing is depicted in Figure 15. The azimuth discretization is identical to the axial flow cases. For the radial spacing, the increased sheet size in radial direction unfortunately introduces large gaps between the sheets. Therefore extra sheets are added in between to cover these gaps. Where the axial traverse has only been performed for the design case, the radial traverse also contains data for the  $U_\infty=10$  m/s and  $U_\infty=24$  m/s case. An overview of the availability of PIV load cases is given in Table 5.

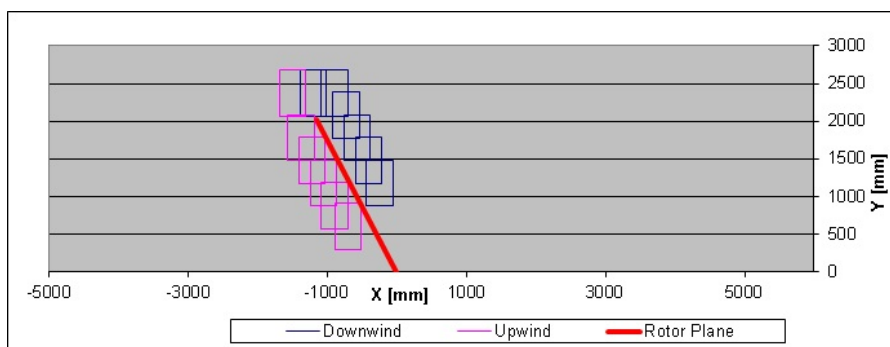
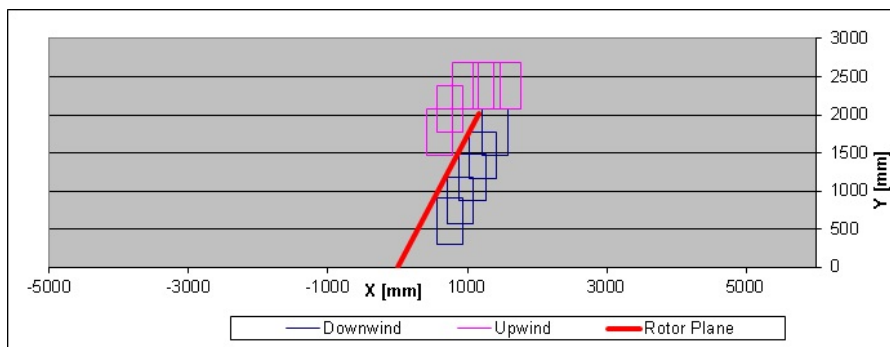
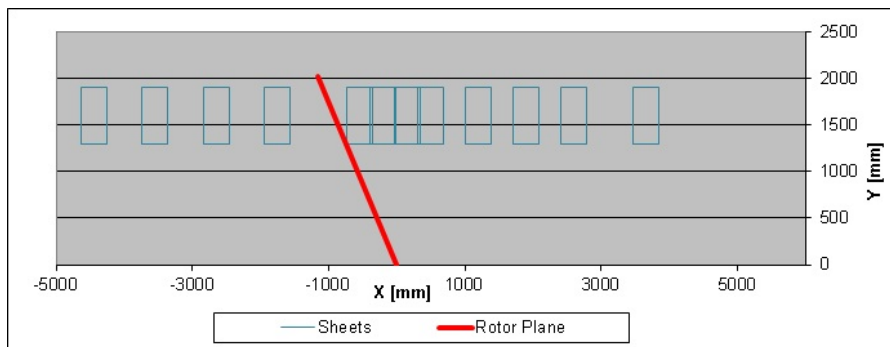
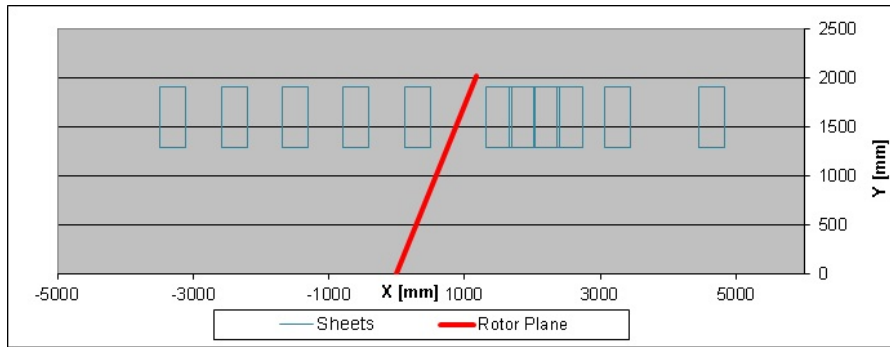


Figure 15: Yawed flow sheet spacing

Table 5: Overview of New MEXICO PIV traverses

$U_\infty$ [m/s]		15	10	15	24
Rot. speed [rpm]		424	424	424	424
Pitch angle [°]		-2.3	-2.3	-2.3	-2.3
Blade config	(Table 3)	0	3	3	3
<hr/>					
Axial flow					
	Axial	x	x		x
	Radial	x	x	x <sup>†</sup>	x
	Momentum			x	
<hr/>					
Yawed flow (+/-30°)					
	Axial			x	
	Radial		x	x	x <sup>‡</sup>
<hr/>					

<sup>†</sup> Downwind sheets repeated for different phase angle to study blade similarity

<sup>‡</sup> Only -30° yaw



# 5

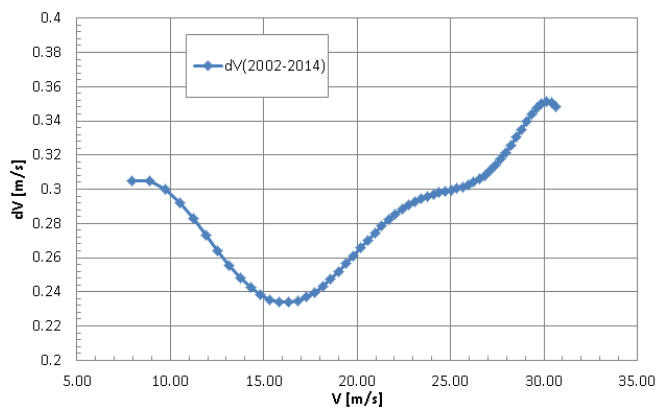
## Preliminary results

This chapter provides a preliminary look into the experimental results. These are divided into subsections roughly following the test matrix order.

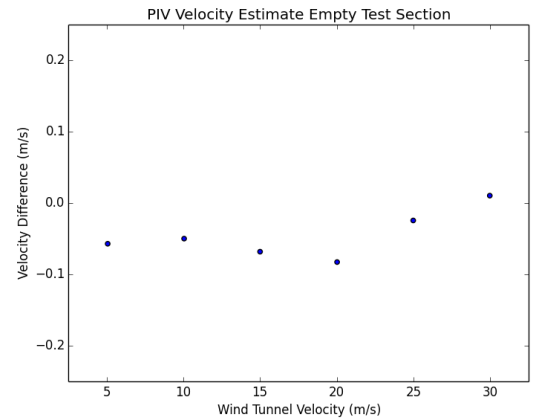
### 5.1 Tunnel calibration and velocity verification

As mentioned in section 3, an empty tunnel calibration was performed for the test set-up with the 9.5 by 9.5 m open jet section. The previous calibration was performed in 2002, but no significant changes to the tunnel have been made as was stated by DNW. As such the calibration results, which consists of a polynomial of the test section pitot dynamic pressure versus a pressure difference over the contraction, are expected to be the same. At first glance the results appeared to be indeed identical. After the test however, a significant variation was observed by zooming in on the velocity difference for standard atmosphere conditions (Figure 16a). The variation with tunnel speed does not seem to obey a trend, which can be explained by the fact that the results are obtained by subtracting the values from two high order polynomials. DNW has stated that the difference between the calibrations is created by the fact that the pitot tube in 2002 was mounted on the "sting", which normally is used to suspend aircraft models [5]. The large frontal area associated with the sting has increased the pitot readings in 2002, which results in an increase of calibrated tunnel speeds compared to 2014 for a given contraction differential. This indicates that the results from the first campaign have to be corrected by lowering the tunnels speeds 0.2 to 0.3 m/s to allow a comparison to the current results. During the empty calibration, a simultaneous measurement of PIV was performed in proximity of the pitot tube. Differences below 0.1 m/s between pitot readings and PIV results were found as depicted in Figure 16b, validating the PIV set-up for the campaign.

After moving the model into the tunnel, a pitot tube was attached to a strut and mounted onto the nacelle. The tube was positioned at  $r=1.525$  m from the rotor center, at the 9 o'clock position (looking at



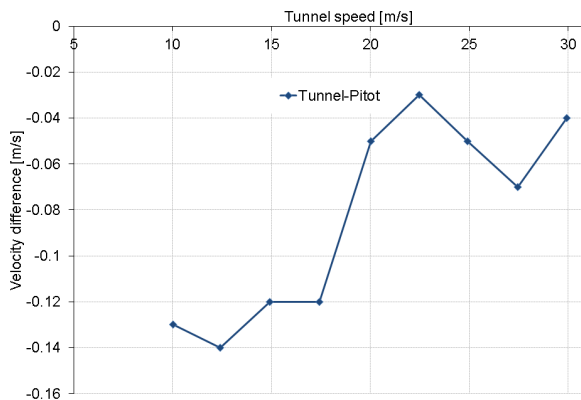
(a) Approximated difference between the 2002 and 2014 tunnel calibrations ( $\rho = 1.225 \text{ kg/m}^3$ )



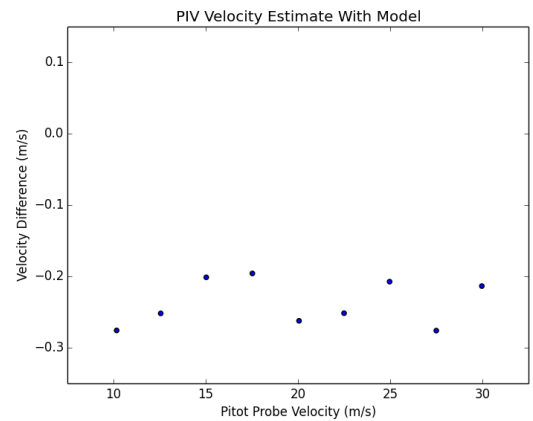
(b) Pitot versus PIV

Figure 16: Empty tunnel results

the model from an upwind location) to allow comparison to simultaneous PIV measurements. The rotor azimuth angle was 210 deg for this test (pitot between blade 1 and 3), and the blades were pitched to vane ( $90^\circ$  pitch angle), to minimize the induction from the blades as verified by CFD simulations prior to the test. The results are shown in Figure 17. The pitot tube was found to agree very well (within 0.1 m/s



(a) Pitot versus calibration



(b) Pitot versus PIV

Figure 17: Velocity verification results

with the velocity as indicated by the tunnel calibration, see also Figure 17a. The PIV results however feature larger differences (Figure 17b), which is subject of further investigation. The PIV values in the graph are represented by the sheet average, whereas the pitot shows a point value. A radial traverse was performed with PIV, which should clarify the velocity variation both in radial and axial direction.

## Application of new calibrations to MEXICO data

After the above investigation it would be interesting to investigate what the effect of the new calibrations is on the measured loads-velocity relationship. Hereby both the tunnel speed as well as the pressures are re-calibrated. The results in terms of axial force coefficient  $C_{dax}$  versus axial induction factor  $a$  are presented in Figure 18. Here the axial induction is calculated by averaging the PIV results up- and downwind of the rotorplane ( $x=-0.3$  m and  $x=+0.3$ m), and the azimuth average is determined by considering the  $0^\circ/60^\circ/80^\circ/100^\circ$  phase locked angles only. The  $20^\circ$  and  $40^\circ$  angles were discarded because their values would not represent the average trend, which is expected to feature large gradients due to the proximity to the blade passage. Since PIV results were not available for the inboard sections these two sections are not included. The rotor averaged values are determined by linear interpolation for both loads and velocities, assuming a zero influence at both the root and tip. For this purpose the missing velocity values of the inboard section are approximated by the average of the available velocity measurements. A line representing one dimensional momentum theory is included as well.

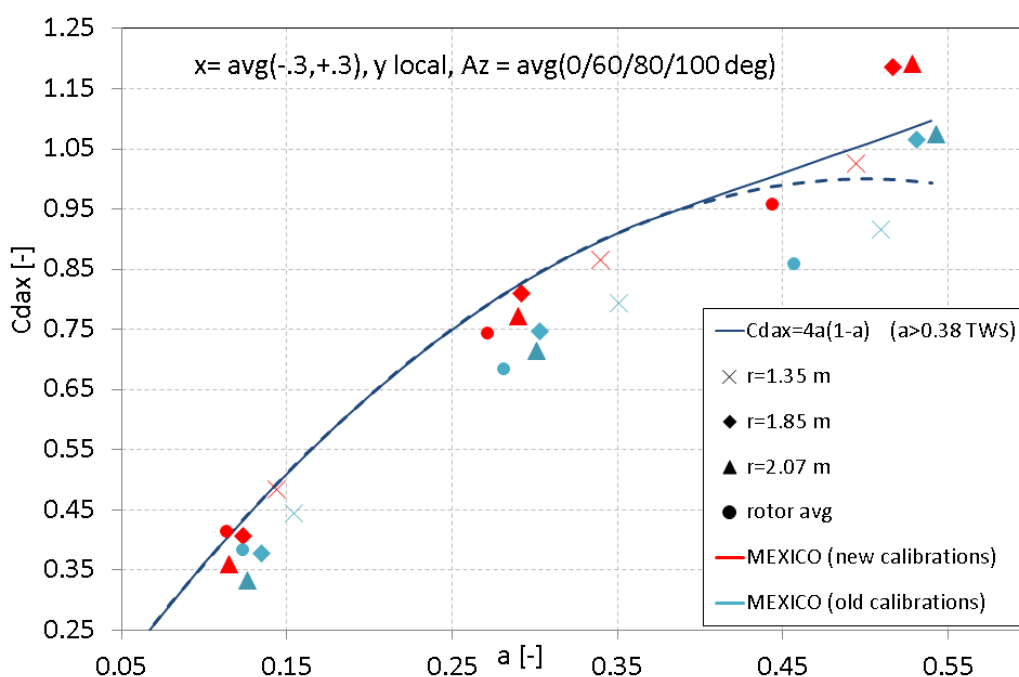


Figure 18: Influence of new calibrations on loads-velocity relationship from MEXICO, results from 424 rpm  $\lambda=4.2, 6.7$  and  $10.0$

From the results it becomes clear that the new calibrations bring the relationship acceptably close to the momentum theory. The lower tunnel speed slightly reduces the axial induction factors. The force coefficients substantially increase due to the fact that the absolute forces are increased (pressure calibration) and are non-dimensionalized using a lower freestream velocity (tunnel calibration). The small

remaining discrepancy from momentum theory can possibly be attributed to remaining experimental uncertainties (e.g. PIV apparatus, determination of induction by axial and azimuthal averaging, assumption of three identical blades) and limited validity of this theory on a local level due to radial mixing. The values obtained for a tip speed ratio of 10 ( $\lambda > 0.4$ ) are anyway situated in the turbulent wake state, where theoretical values are subject to engineering approximations. More considerations towards the validity of this approach are included in section 5.2.

## 5.2 Comparison to MEXICO

To check the consistency between the MEXICO and New MEXICO dataset, a comparison of runs with similar operational conditions was made. Both loads (balance and pressures) as well as velocities (PIV) are subject of investigation.

### Loads

Both sectional loads as well as axial force results are discussed. The torque data are yet to be processed.

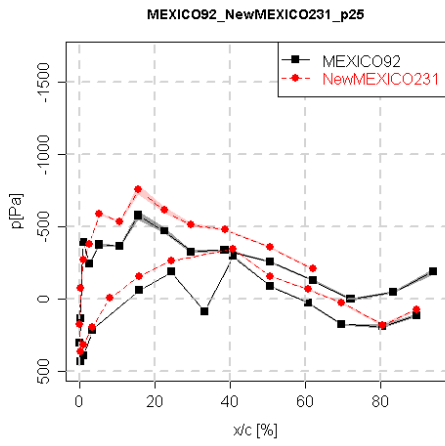
### Sectional loads

Figure 19 to Figure 21 show a comparison of the pressure distributions for three cases across the operational regime, together with the resulting normal force plot from integrating the pressures. Both results here use the pressure calibration as determined in November 2013, see also section 3.2. Since the tunnel speed of the previous campaign has not been re-calibrated yet by DNW, a constant value of 0.2 m/s has been deducted from the measurements.

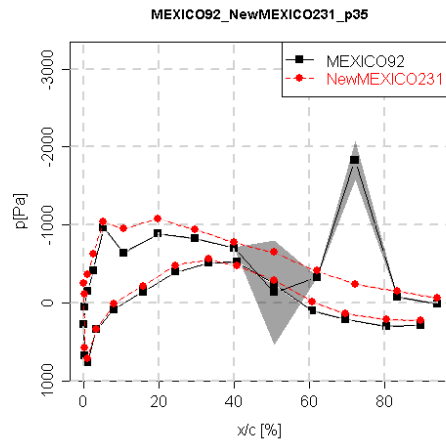
Generally speaking the agreement is very satisfactory, although there are small differences in air density and operational condition due to the fact that the tunnel speed setting from the first campaign is off due to the calibration discrepancy. Several inboard sensors from the first campaign were faulty, which were repaired prior to the New MEXICO campaign. As was reported in section 3.3, the uncertainty associated with the inboard pressure sensors can become large. For example Figure 19a shows a clear offset, as this combination of wind speed and radial location features the lowest dynamic pressure. The largest differences in the resulting normal force are observed for the low tip speed ratio case (Figure 21f). This could be attributed to the fact that for separated flow conditions, small differences in operational and surface condition can result in significant aerodynamic variations.

### Axial force

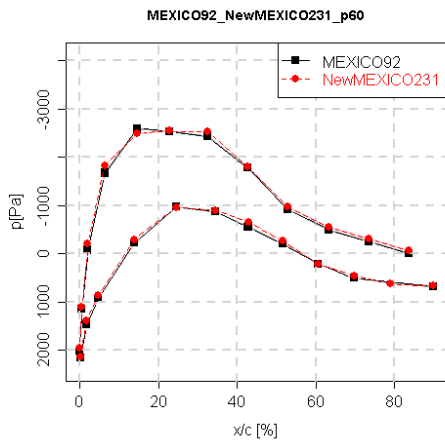
The axial force is compared for a pitch angle of  $-2.3^\circ$  at 424 rpm for both the balance as well as the pressure results in Figure 22. Since the tunnel speed of the previous campaign has not been re-calibrated yet by DNW, a constant value of 0.2 m/s has been deducted from the measurements. The balance provides the total force in x-direction from which the contribution of the tower and nacelle are deducted. This includes estimates for the drag of these components. For the pressures, the blades are assumed to feature the same aerodynamic forces. The pressures from the various blades are integrated linearly in chordwise and spanwise direction, assuming zero loads at the root and tip. The resulting integrand is increased by



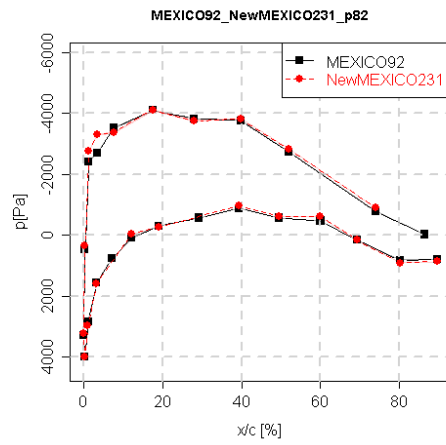
(a) Pressure distribution at 25%R



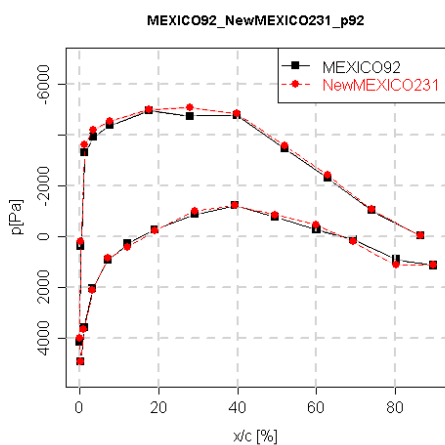
(b) Pressure distribution at 35%R



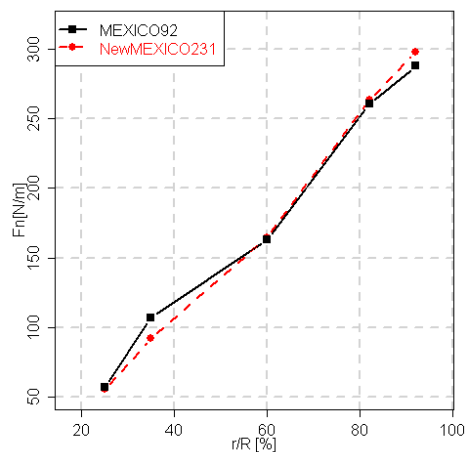
(c) Pressure distribution at 60%R



(d) Pressure distribution at 82%R



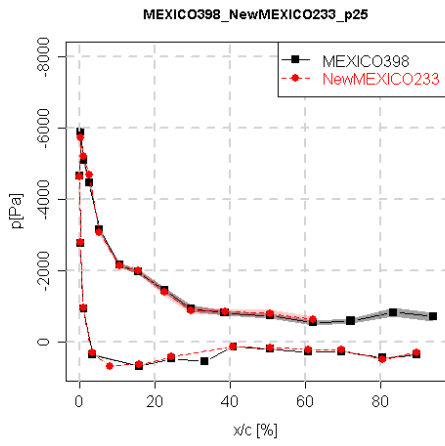
(e) Pressure distribution at 92%R



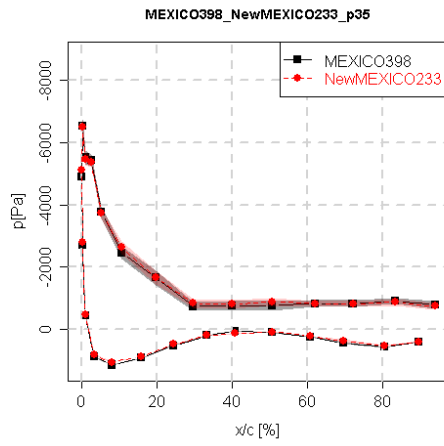
(f) Normal force distribution

Figure 19: Comparison between MEXICO ( $U_\infty=9.77$  m/s,  $\lambda=10.2$ ,  $\rho=1.19$  kg/m<sup>3</sup>) and New MEXICO ( $U_\infty=10.04$  m/s,  $\lambda=10.0$ ,  $\rho=1.21$  kg/m<sup>3</sup>) sectional loads in axial flow at 424 rpm,  $-2.3^\circ$  pitch

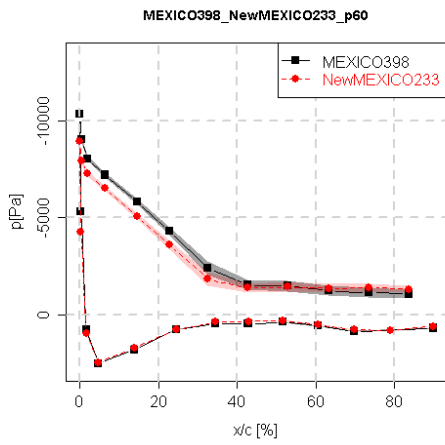




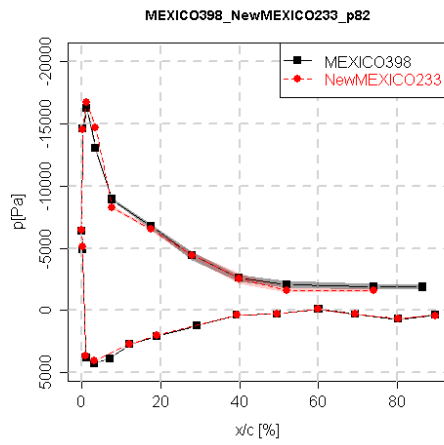
(a) Pressure distribution at 25%R



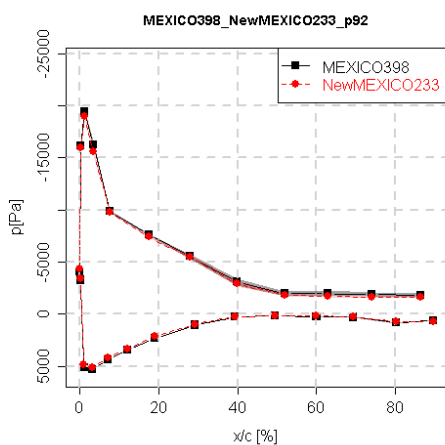
(b) Pressure distribution at 35%R



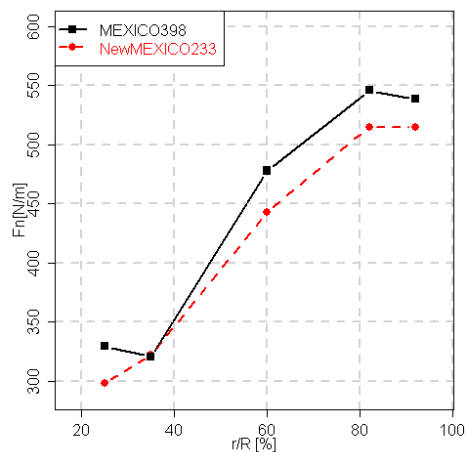
(c) Pressure distribution at 60%R



(d) Pressure distribution at 82%R



(e) Pressure distribution at 92%R



(f) Normal force distribution

Figure 21: Comparison between MEXICO ( $U_\infty=23.76$  m/s,  $\lambda=4.2$ ,  $\rho=1.20$  kg/m<sup>3</sup>) and New MEXICO ( $U_\infty=24.13$  m/s,  $\lambda=4.2$ ,  $\rho=1.20$  kg/m<sup>3</sup>) sectional loads in axial flow at 424 rpm,  $-2.3^\circ$  pitch

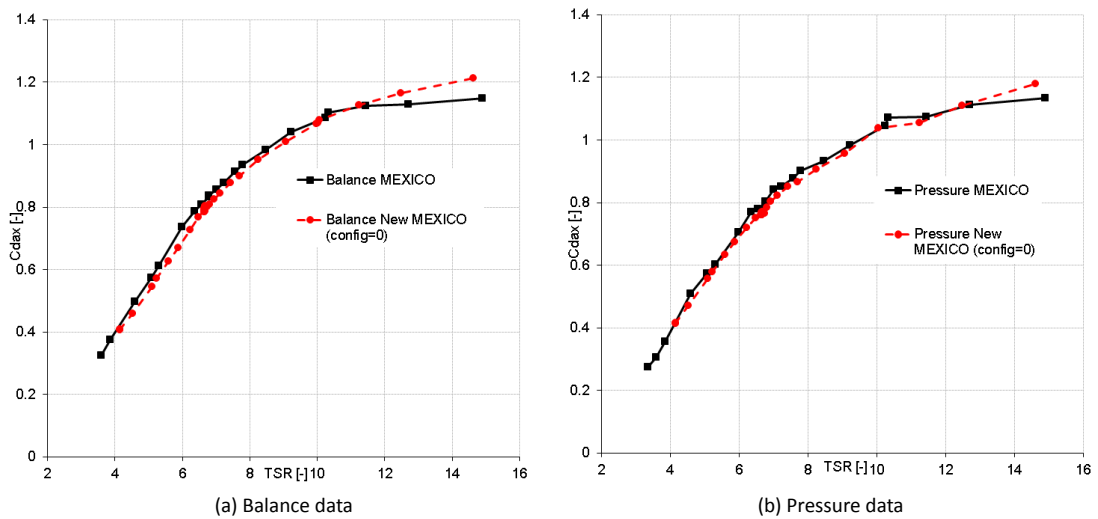


Figure 22: Comparison of axial force coefficient  $C_{dax}$  as a function of tip speed ratio  $\lambda$  between MEXICO and New MEXICO (424 rpm,  $-2.3^\circ$  pitch)

6% to correct for the fact that the axial force variation with radius at the root and tip areas is not linear. This factor results from an investigation using CFD results as previously reported [9]. Generally speaking the results are again satisfactory, indicating that the set-up for 2014 is similar to the 2006 experiment and the load results can be compared.

### Velocities

Both axial as well as radial traverses were performed, similar to the traverse in the first campaign.

#### Axial traverse

The comparison results are shown in Figure 23 for the axial velocity. The MEXICO velocities are not corrected for the new tunnel calibration here. The most upwind results show a deviation of around 0.4 m/s which is slightly larger than the results indicated by the empty tunnel calibration. Anyhow, the CFD results from EllipSys3D seem to be in good agreement with the New MEXICO values for the upwind region. Where the  $r=1.4\text{m}$  results from the previous campaign suffered from laser sheet reflections, the nacelle paint applied for New MEXICO seems to prevent this. Also for  $r=1.8\text{m}$ , the values show differences. This could well be attributed to vortex structures that were observed in the preliminary radial traverse results and will be subject of further study.

#### Radial traverse

To compare the radial traverse results, the variation of axial velocity with azimuth angle was plotted for specific radial locations, using both the upwind and downwind sheets. Again the MEXICO velocities are not corrected for the new tunnel calibration. Although the inboard part has also measured in New MEXICO, for the sake of comparison the results for  $r/R=60\%$  and  $92\%$  are shown in Figure 24 and 25. Similar

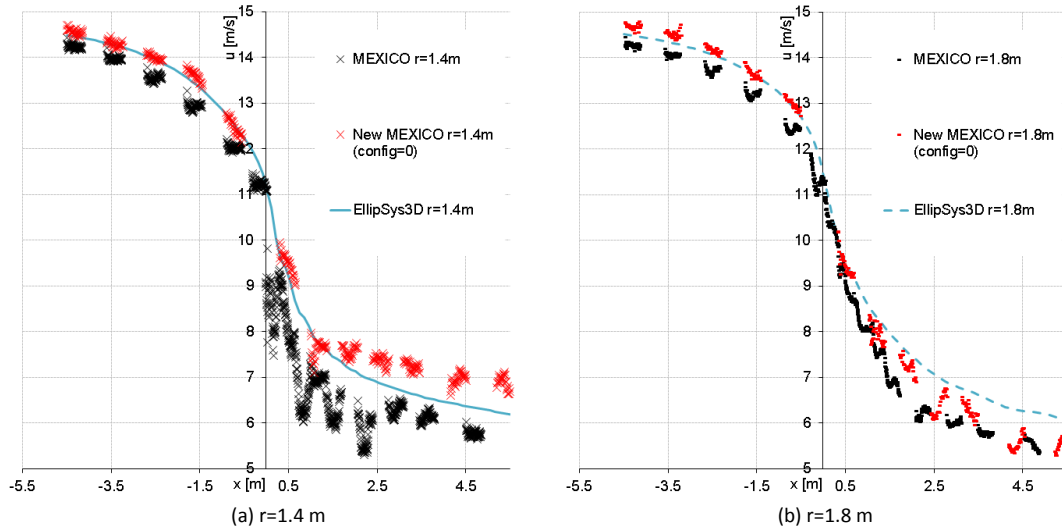


Figure 23: Comparison of axial velocity from axial traverse,  $U_\infty=15$  m/s, 424 rpm,  $-2.3^\circ$  pitch,  $0^\circ$  azimuth

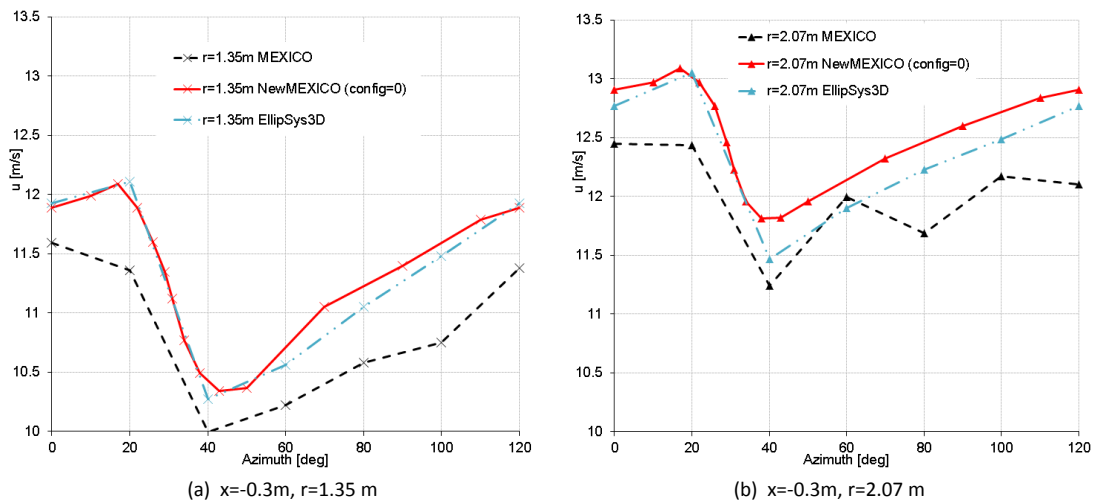


Figure 24: Comparison of axial velocity from upwind radial traverse,  $U_\infty=15$  m/s, 424 rpm,  $-2.3^\circ$  pitch

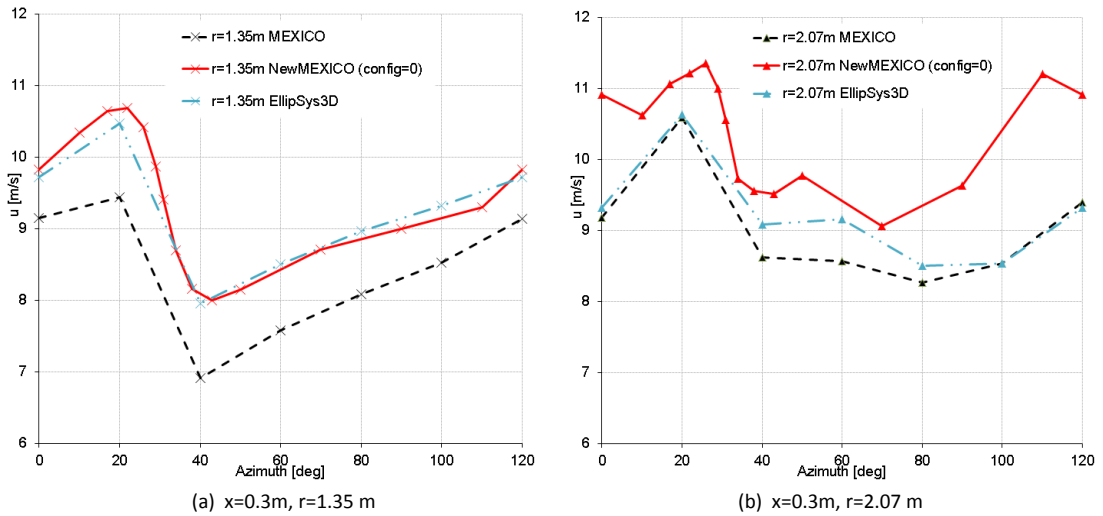


Figure 25: Comparison of axial velocity from downwind radial traverse,  $U_{\infty}=15$  m/s, 424 rpm,  $-2.3^{\circ}$  pitch

as for the radial traverse, an offset around 0.4 to 0.5 m/s is found compared to the previous campaign results. The velocity trend around the blade passage ( $30^{\circ}$  azimuth) is captured better now due to the increased azimuth resolution. Although the agreement of the CFD results with the new measurements generally speaking is very good, especially at  $r=2.07$  m discrepancies can be observed. For the upwind traverse in Figure 23b, this is shown mostly after the blade passage. In the wake (Figure 25b) the CFD seems to underpredict the measurements by approximately 0.5 m/s. It can also be observed that the axial induction at 92%R is significantly lower than at 60%R.

## Momentum

Combining the loads and velocity measurements, it would be interesting to see how the New MEXICO results compare to the momentum theory. In addition to that the CFD results are processed in a similar way as the experimental data to validate the approach. The same approach as outlined in section 5.1 and displayed in Figure 18 has been taken. Since the New MEXICO results contain a tailored spacing around the blade passage, the azimuth average induction has been determined using all available data for this case. Application of this approach and the previously outlined approach (taking steps of  $20^{\circ}$  between  $0^{\circ}$  and  $120^{\circ}$  and omitting the  $20^{\circ}$  and  $40^{\circ}$  angle) to the New MEXICO data revealed differences of less than 0.009 in the axial induction factor  $a$ . The resulting picture is shown in Figure 26, where also the inboard data are included. Most of the results are found to scatter around the theoretical line. The fact that the CFD results mostly agree with this line seems to validate the approach taken. Again it is shown that the turbulent wake state at high induction is difficult to approximate by both theory and CFD. The rotor averaged values, which are indicated by a filled circle, are consistently found closer to the theoretical line in comparison to several outliers at local positions. This seems to indicate that the radial independence approach of BEM is not strictly valid. It should be investigated further whether the measured outliers can be related to radial discontinuities which were found in the preliminary contour plots, possibly caused

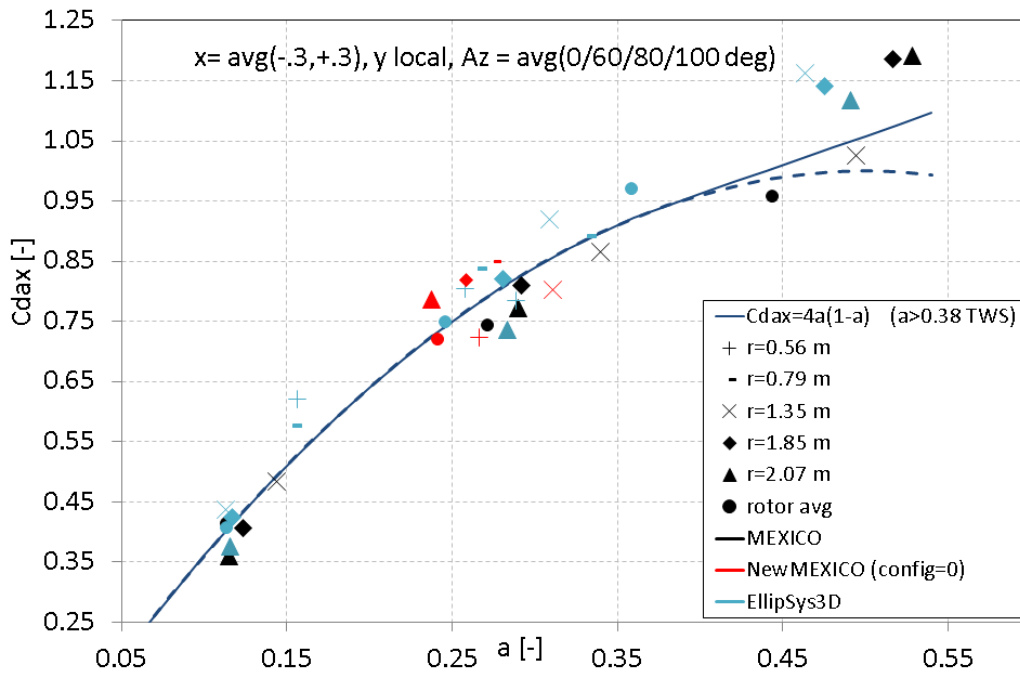


Figure 26: Loads-velocity relationship from (New) MEXICO and CFD, results from 424 rpm,  $\lambda=4.2, 6.7$  and 10.0

by the airfoil transition regions.

### 5.3 Influence of roughness

The influence of roughness strips on the rotor loads is assessed. Firstly the section loads are discussed after which the effect on the rotor axial force is subject of discussion. The PIV results are yet to be processed. The same holds for the effect on the rotor torque.

#### Sectional loads

Figure 27 to Figure 29 show a comparison of the pressure distributions for three cases across the operational regime, together with the resulting normal force plot from integrating the pressures. Both results here use the pressure calibration as determined in November 2013, see also section 3.2. Since the tunnel speed of the previous campaign has not been re-calibrated yet by DNW, a constant value of 0.2 m/s has been deducted from the measurements.

Since difference in tripping configuration only applies to the outboard sections, a difference in pressure distribution should only be observed for the 82%R and 92%R section if no radial interaction occurs. The normal plot distributions for attached flow conditions (Figure 27f and 28f) confirm this image by showing

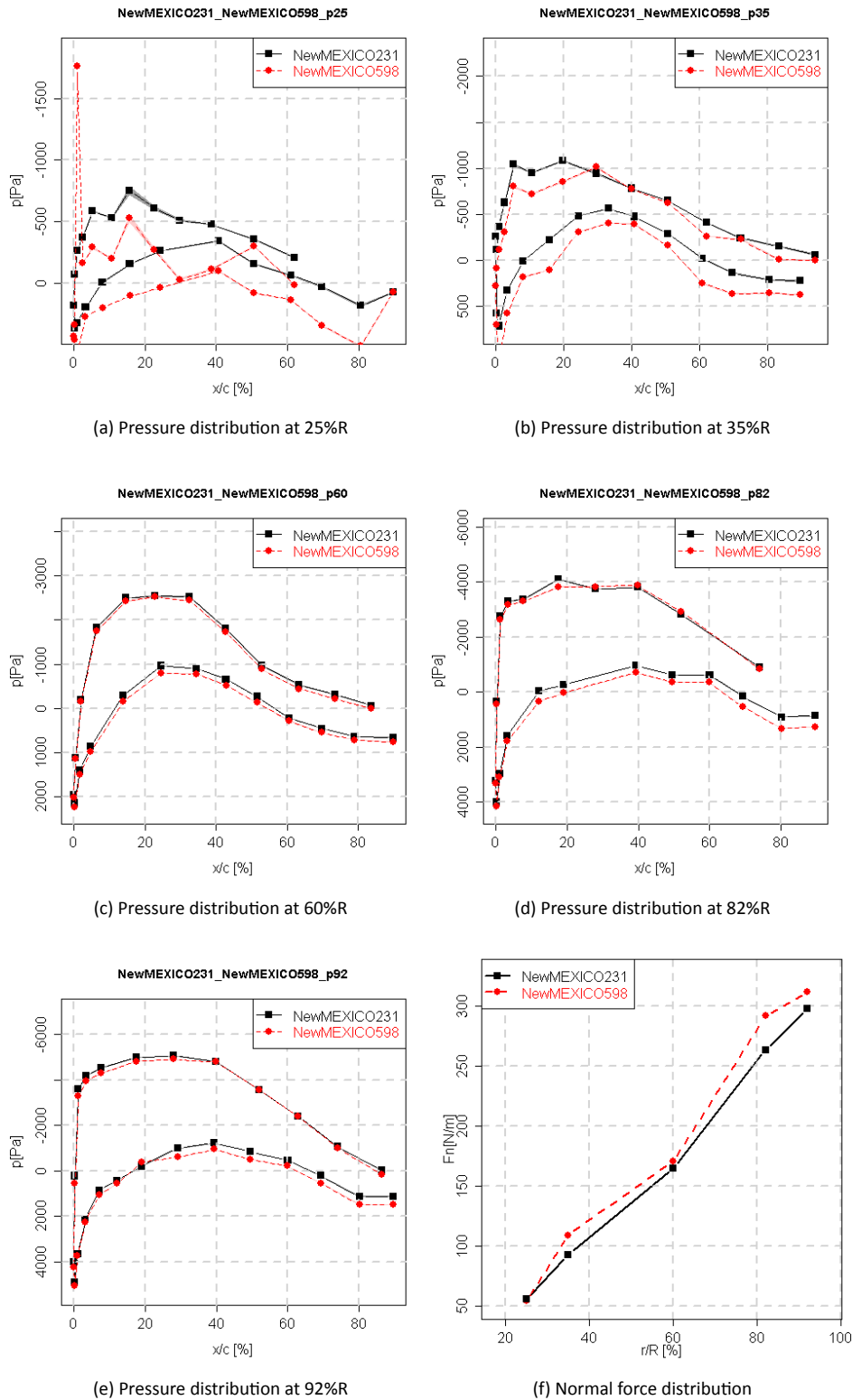


Figure 27: Influence of roughness strips: Comparison between datapoint 231 (config=0,  $U_\infty=10.04$  m/s,  $\lambda=10.0$ ,  $\rho=1.21$  kg/m<sup>3</sup>) and 598 (config=3,  $U_\infty=10.05$  m/s,  $\lambda=10.0$ ,  $\rho=1.19$  kg/m<sup>3</sup>) sectional loads in axial flow at 424 rpm, -2.3° pitch

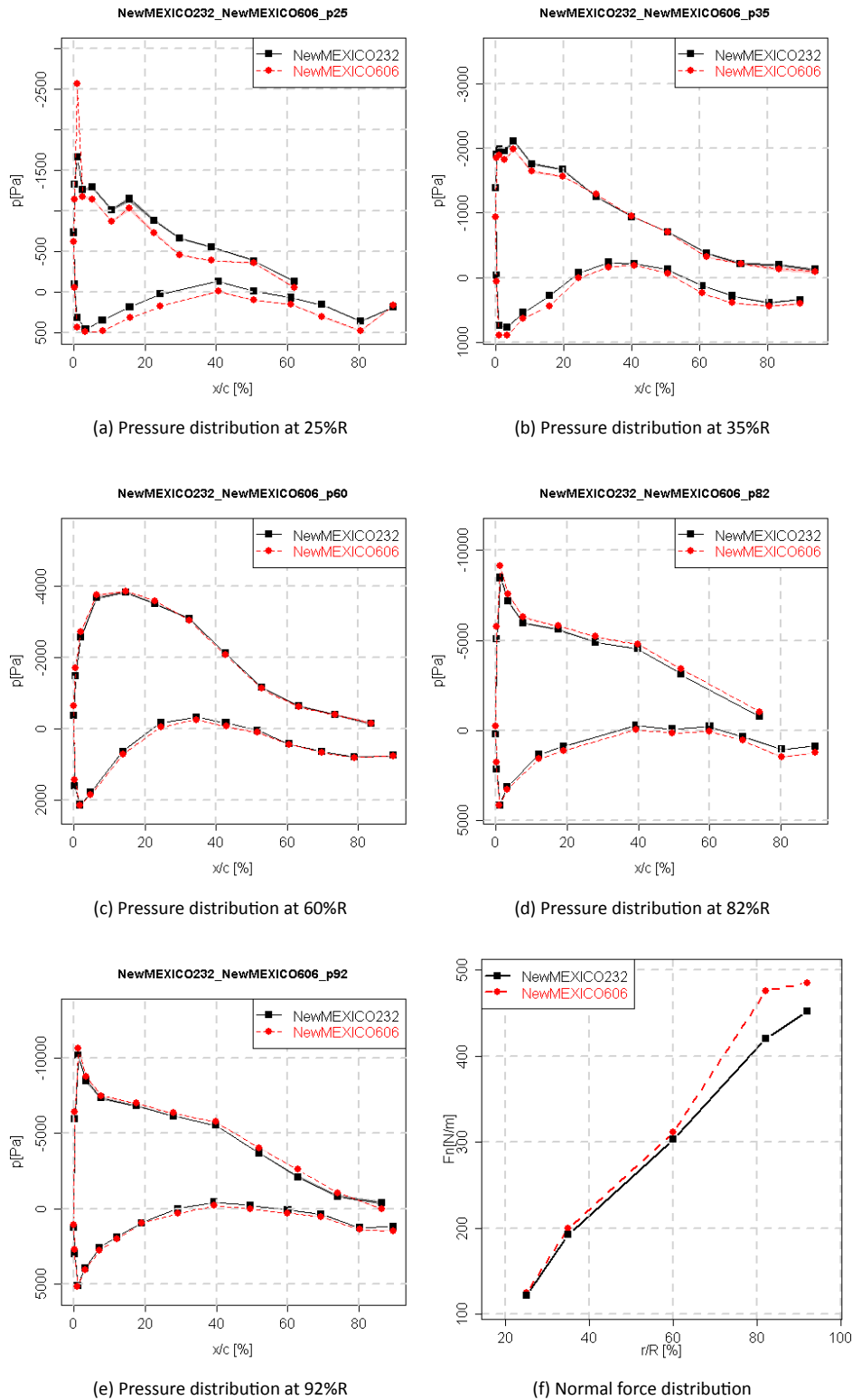


Figure 28: Influence of roughness strips: Comparison between datapoint 232 (config=0,  $U_\infty = 14.86$  m/s,  $\lambda = 6.7$ ,  $\rho = 1.20$  kg/m<sup>3</sup>) and 606 (config=3,  $U_\infty = 15.03$  m/s,  $\lambda = 6.7$ ,  $\rho = 1.19$  kg/m<sup>3</sup>) sectional loads in axial flow at 424 rpm, 23° pitch

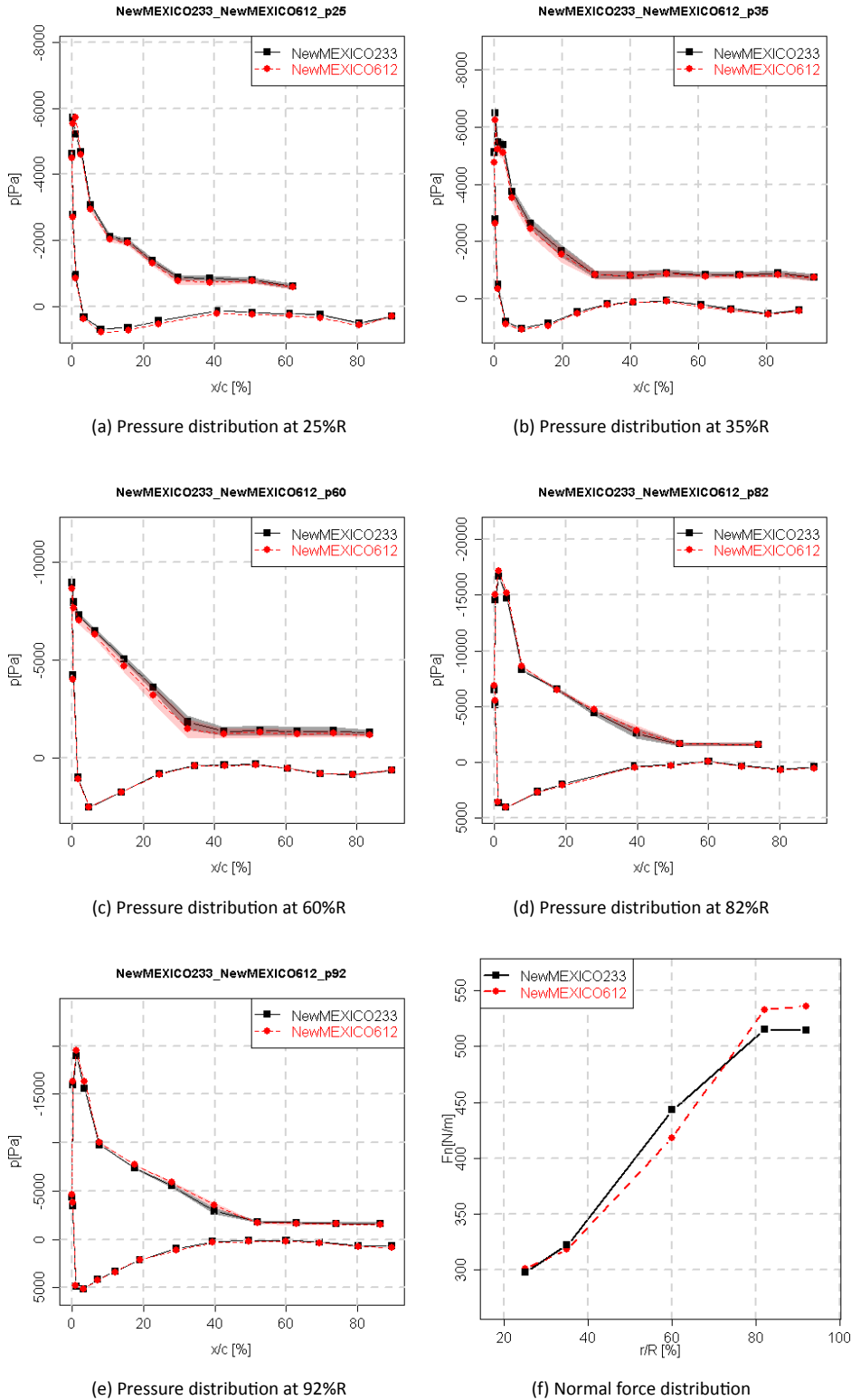


Figure 29: Influence of roughness strips: Comparison between datapoint 233 (config=0,  $U_\infty=24.13$  m/s,  $\lambda=4.2$ ,  $\rho=1.20$  kg/m<sup>3</sup>) and 612 (config=3,  $U_\infty=24.08$  m/s,  $\lambda=4.2$ ,  $\rho=1.19$  kg/m<sup>3</sup>) sectional loads in axial flow at 424 rpm, -2.3° pitch

a load increase for clean conditions, whilst for separated flow (Figure 29f) this is the case to a lesser extent. For this case the 60%R section shows earlier separation in clean condition and consequently features a lower normal force. This is remarkable because the trip strip is still present at this section in clean conditions. Possibly slight differences in set-up (soil or operational condition) or radial interaction of separated flow features can be held responsible. Although the normal force results at 25%R and 35%R look similar, the pressure distributions clearly indicate again that the accuracy of the pressure sensors is limited for these sections.

### Axial force

The axial force is compared for a pitch angle of  $-2.3^\circ$  at 424 rpm for both the balance as well as the pressure results in Figure 30. Since the tunnel speed of the previous campaign has not been re-calibrated yet by DNW, a constant value of 0.2 m/s has been deducted from the measurements.

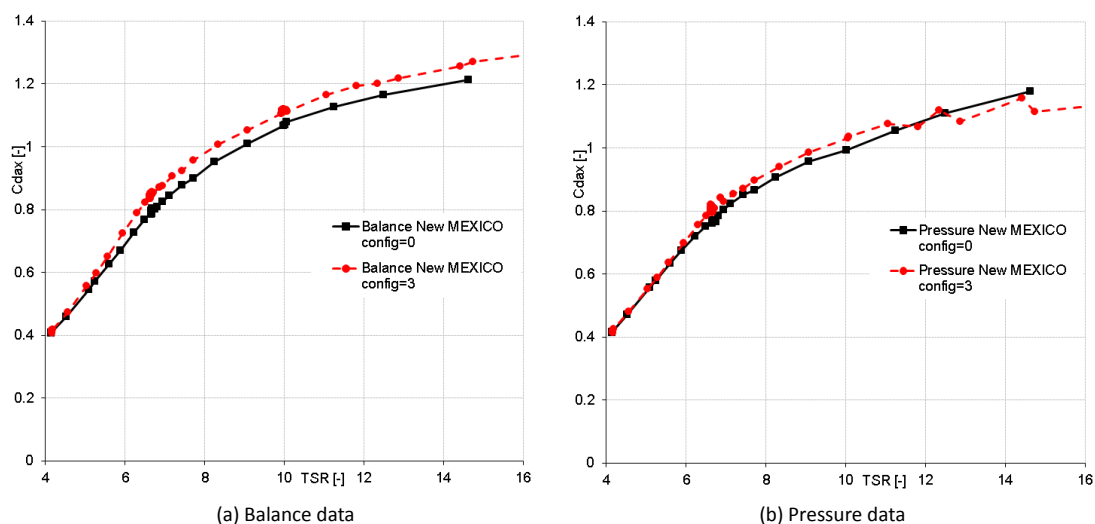


Figure 30: Comparison of axial force coefficient  $C_{dax}$  as a function of tip speed ratio  $\lambda$  between rough and partially clean configuration (424 rpm,  $-2.3^\circ$  pitch)

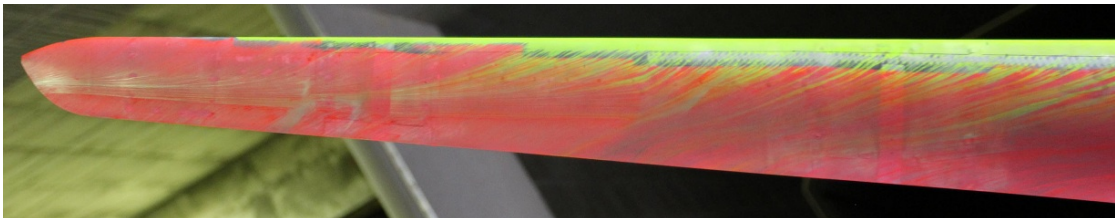
Approximately from a tip speed ratio of 6, there is a clear increase noticeable in axial force for clean conditions. The balance results show a slightly larger increase compared to the pressure data. It should be realized that the pressure data is the result of different sections distributed over the 3 blades. At high tip speed ratios the pressure results for the clean configuration seem to approximate the rough configuration results, although the trend of the line seems to indicate there is a repeatability issue. This should be subject of further investigation by having a closer look at the pressure distributions.

## 5.4 Flow visualization

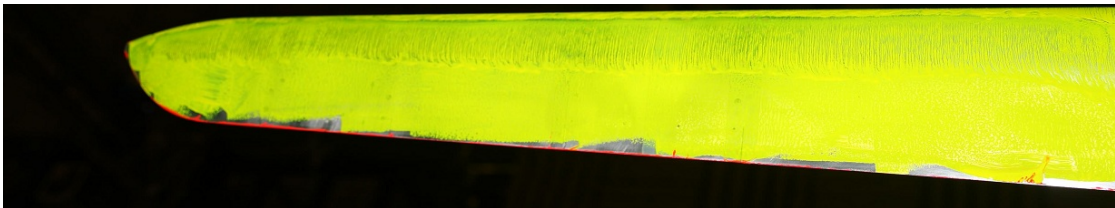
Both oil flow as well as a smoke visualizations were performed.

### Oil flow

The substance used for the flow visualization is a mixture of paraffin, petroleum and pigment. A red paint was used on the pressure side, whilst a yellow paint was used on the suction side of blade 2. Some results are shown in Figure 31. It appeared that for rotating conditions, the centrifugal force dominates the whereabouts of the oil and hence a flow pattern is not visualized. This is illustrated in Figure 31a, which shows the radial pattern even in the outboard region of the blade.



(a) Pressure side,  $r/R \gtrsim 50\%$  ( $\lambda = 6.7$ , 424 rpm,  $-2.3^\circ$  pitch)



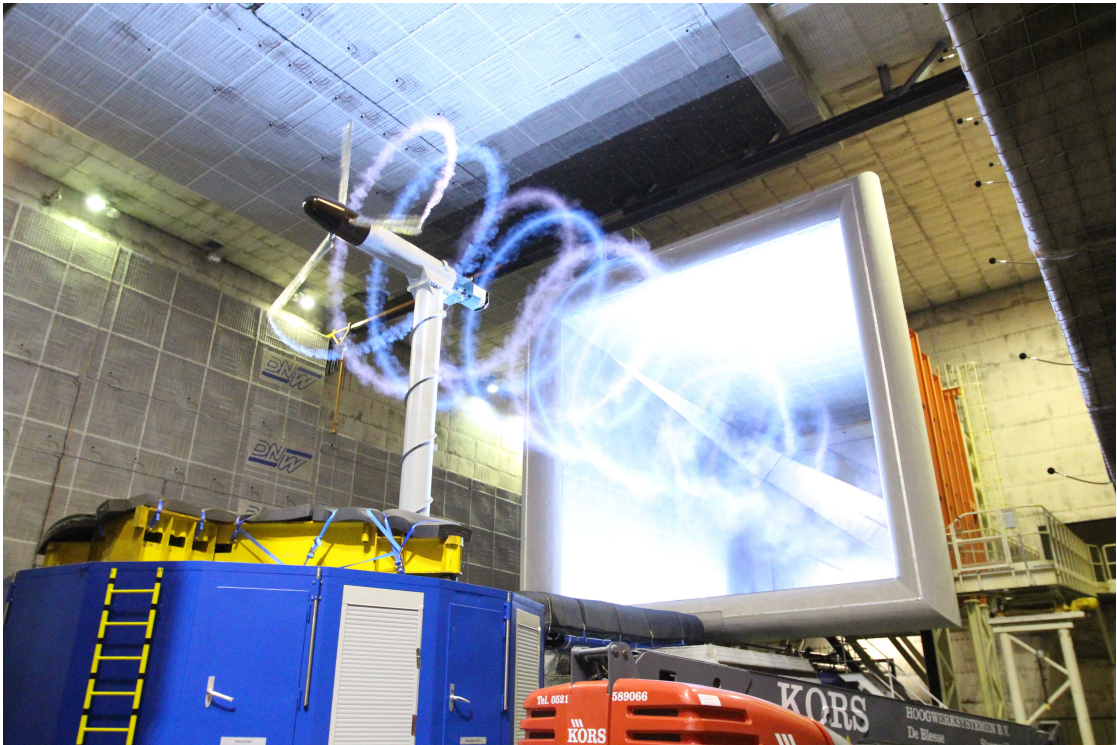
(b) Suction side,  $r/R \gtrsim 70\%$  ( $U_\infty = 30$  m/s, 0 rpm,  $73.6^\circ$  pitch)

Figure 31: Oil flow visualization results (flow from top to bottom)

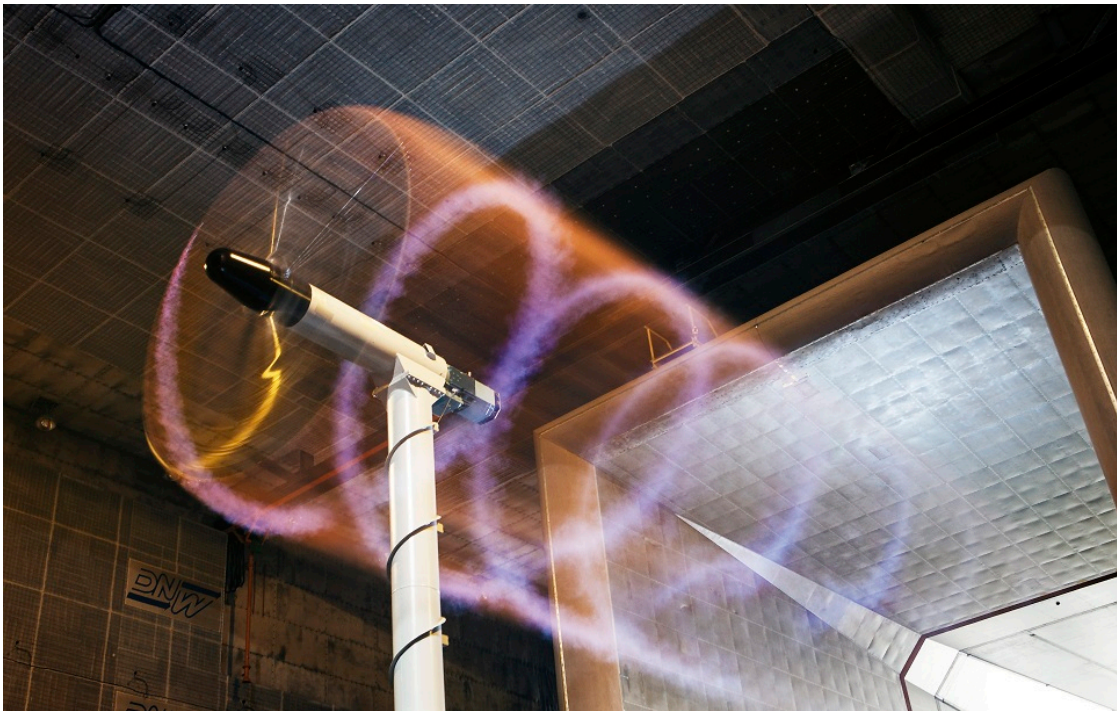
Therefore a standstill case was included as well, which should allow for a comparison to the static experiment results from section 3.3. Although flow patterns are more clearly visible here, it remains more difficult to interpret the picture compared to the corresponding image of Figure 11b. Although the mushroom patterns seem to be absent in Figure 31b, the locations of the separation line seem to agree at approximately 40% chord. Here it must be noted that the static experiment featured roughness strips, whereas this part of the New MEXICO experiment did not (for the radial position in the picture). In addition to that the Reynolds numbers are not matching. The taping off of the sensors for the oil flow measurements also should have provided information regarding the influence of centrifugal force on the pressure sensor readings. Unfortunately it appeared that the trigger for saving the pressure data was not given by the data acquisition software for these cases.

## Smoke

Smoke candles were attached to all three blade tips for this purpose. It appeared to be difficult to have all three candles simultaneously ignited. A first impression can be gained from Figure 32 Although the pictures allow to study tip vortex travel, the main reason for this test was to gain material for promotional activities.



(a)



(b)

Figure 32: Smoke visualization of tip vortices for  $\lambda=4.4$ , 424 rpm

# 6

## Conclusions

An overview has been given of the New MEXICO wind turbine measurements as carried out in the the Large Scale Low Speed Facility (LLF) of the German Dutch Wind Tunnels (DNW) between June 20<sup>th</sup> and July 4<sup>th</sup> 2014. The test is a follow up of the first MEXICO campaign, which was held in 2006. The main objective of the test is to progress aerodynamic (and acoustic) modelling of wind turbines and wind turbine farms. The test preparation activities have been described, including a pressure sensors calibration and static wind tunnel test of the blades. Some preliminary results of the rotating test have been presented in the report. Several open questions from the first campaign have been resolved and a good agreement has been found between these measurements. The MEXICO database has been extended with extra test cases to progress modelling of dynamic inflow, non-uniformity between the blades, yawed flow effects, parked conditions and pitch misalignment. In addition to that several blade add-ons were tested to improve the turbine performance. An example is the blade root spoiler invented by ECN. Acoustic measurements have been performed using both far field microphones as well as a microphone array. Flow visualization has been performed by application of smoke candles to the blade tips and oil to the blade surface.

The conclusion is that ECN and partners have performed very successful aerodynamic experiments in the largest wind tunnel in Europe. A comprehensive high quality database has been obtained which is shared in the wind energy R&D community. The database will be analysed in an international context in order to validate aerodynamic models and to advance the aerodynamic modelling of wind turbines. With the results future large wind turbines will be designed with higher accuracy and less uncertainty.



# Bibliography

- 1 <http://www.eswirp.eu/>. In *European Strategic Wind tunnels Improved Research Potential*, 2014.
- 2 A. Rosen, A. Wolf, D. Ben-Shmuel and G. Omri. “The Mexico project, Wind Turbine Model Part 1”. TAE report 985 NN, Faculty of Aerospace Engineering Technion-Israel Institute of Technology, July 2011.
- 3 A. Rosen, A. Wolf, D. Ben-Shmuel and G. Omri. “The Mexico project, Wind Turbine Model Part 2”. TAE report 986 NN, Faculty of Aerospace Engineering Technion-Israel Institute of Technology, July 2011.
- 4 D. Micallef. “MEXICO Data Analysis, Stage I - MEXICO Data Validation and Reliability Testst”. TUDelft report, Technical University of Delft, February 2009.
- 5 DNW. New MEXICO test. Technical report, To be published in 2014.
- 6 J.G. Schepers and H. Snel. MEXICO, Model experiments in controlled conditions. ECN-E-07-042, Energy Research Center of the Netherlands, 2007.
- 7 J.G. Schepers and K. Boorsma et al. Final report of IEA Task 29, Mexnext (Phase 1): Analysis of MEXICO wind tunnel measurements. ECN-E-12-004, Energy Research Center of the Netherlands, February 2012.
- 8 K. Boorsma and J.G. Schepers. “Description of experimental set-up. Mexico measurements”. ECN-X-11-120, Energy Research Center of the Netherlands, ECN, March 2009.
- 9 K. Boorsma et al. The Latest Results on Experimental Wind Turbine Aerodynamics. In *Proceedings of EWEA 2014 conference*, March 2014.
- 10 E. Lommerse. email with answers to pressure sensor related questions. email, Stekon, January 2014.
- 11 P. Fuglsang and C. Bak. Development of the RISØ wind turbine airfoils. *Wind Energy*, 7(2), 2004.
- 12 J. G. Schepers, A. Brand, A Bruining, J. Graham, M. Hand, D. Infield, H. Madsen, J. Paynter, and D. Simms. Final Report of IEA Annex XIV: Field Rotor Aerodynamics. Technical report, ECN-C-97-027, 1997.



# A

## Kulite® specification sheet

Table 6: Specifications of Kulite® XCQ-95-062-5A

INPUT	
Pressure Range	35 kPa (5 psiA)
Measuring range	40 kPa to 106 kPa Absolute (5.8 to 15.37 psiA)
Operational Mode	absolute
Over Pressure	3 times rated pressure
Burst Pressure	4 times rated pressure
Pressure Media	All non conductive, non corrosive Liquids or Gases
Rated Electrical	Excitation 10 VDC/AC
Maximum Electrical Excitation	15 VDC/AC
Input Impedance	800 (Min.)
OUTPUT	
Output Impedance	1000 ohms (Nom.)
Full Scale Output (FSO)	90 mV (Nom.)
Output at 14.5 psiA (100KPaA)	270 mV (Nom)
Residual Unbalance	± 3 % FSO
Combined Non-Linearity and Hysteresis	± 0.25 % FS BFSL
Hysteresis	Less Than 0.1 % (typ.)
Repeatability	± 0.1 %
Resolution	Infinite
Natural Frequency (KHz)	>150 KHz
Acceleration Sensitivity % FS/g	
Perpendicular	0.002
Transverse	0.0005
Insulation Resistance	50 Megohm Min. at 100 VDC
ENVIRONMENTAL	
Operating Temperature Range	-55° C to +120° C
Compensated Temperature Range	+10° C to +65° C
Thermal Zero Shift	± 1 %/55° C (typ.)
Thermal Sensitivity Shift	± 1 %/55° C (typ.)
Steady Acceleration	10.000 g (max.)
Linear Vibration	10 - 2000 Hz Sine, 100 g max.
PHYSICAL	
Electrical Connection	4 leads AWG 38 (dia including Teflon insulator 0.23 mm). Length between transducer and TC module to be specified later. Length after module to be specified later.
Housing length	2.54 mm (0.1")
Compensation module	2.8 mm dia × 25.4 mm long (0.110 x 1" long)
Weight	0.2 Gram (Nom.) Excluding Module and Leads
Diaphragm protection	B-screen
Sensing Principle	Fully Active Four Arm Wheatstone Bridge Diffused into Silicon Diaphragm



**ECN**

Westerduinweg 3  
1755 LE Petten  
The Netherlands

P.O. Box 1  
1755 ZG Petten  
The Netherlands

T +31 88 5154949  
[info@ecn.nl](mailto:info@ecn.nl)  
[www.ecn.nl](http://www.ecn.nl)

## Document information

Document Name:	Validation of models by the New MEXICO data
Document Number:	Deliverable 2.13 Part II
Author:	Ed. H Aa Madsen (DTU); J Prospathopoulos (NTUA); S Voutsinas (NTUA); V Riziotis (NTUA), K Diakakis (NTUA), P Chassapoyiannis (NTUA)S Gomez-Irardi (CENER); X M Echarri (CENER); A I Ruiz (CENER); W Z Shen (DTU); N N Sørensen (DTU)
Document Type	Report
Dissemination level	PU
Review:	Flemming Rasmussen (DTU)
Date:	June 2015
WP:	WP2: Lightweight Rotor
Task:	Task 2.13: Validation by experiments
Approval:	Approved by Author

## TABLE OF CONTENTS

LIST OF FIGURES & TABLES .....	4
CHAPTER 1 .....	6
1.1 Background .....	6
1.2 Introduction to D2.1.3 .....	6
CHAPTER 2 THE MODELS USED IN THE VALIDATION EXERCISE .....	7
2.1 Introduction .....	7
2.2 The aeroelastic code FAST .....	7
2.2.1 Tip and Hub corrections .....	7
2.2.2 Correction for turbulent wake .....	8
2.2.3 Skewed wake correction .....	8
2.2.4 Dynamic inflow .....	8
2.2.5 Static airfoil tables .....	8
2.2.6 Dynamic stall model .....	8
2.2.7 Input data used .....	9
2.3 The compressible CFD code WMB .....	9
2.4 The compressible CFD code MaPFlow .....	10
2.5 The Actuator Line/Navier-Stokes (ACL) code .....	10
2.5.1 The Navier Stokes solver .....	10
2.5.2 The actuator Line technique .....	11
2.6 The incompressible CFD code EllipSys3D .....	12
2.7 The aeroelastic code HAWC2 .....	12
CHAPTER 3 THE SIMULATION CASES .....	14
3.1 Description of cases .....	14
CHAPTER 4 RESULTS .....	18
4.1 Pressure distributions .....	18
4.1.1 Low wind speed cases at both 325 rpm and 425 rpm .....	18
4.1.2 Middle wind speed cases at both 325 rpm and 425 rpm .....	18
4.1.3 High wind speed cases at both 325 rpm and 425 rpm .....	18
4.1.4 General comments to comparison of pressure distributions .....	19
4.1.5 Pressure distributions at 325 rpm .....	20
4.1.6 Pressure distributions at 425 rpm .....	23
4.2 Radial blade force distributions .....	26
4.2.1 Comments on the blade force distributions .....	26
4.2.2 Radial blade force distributions – 325 rpm .....	27
4.2.3 Radial blade force distributions – 425 rpm .....	28
4.3 Integrated rotor forces from pressure distributions .....	29
CHAPTER 5 CONCLUSION .....	30
REFERENCES .....	31

## LIST OF FIGURES & TABLES

Figure 3.1-1 The overall test matrix for the New MEXICO experiment. Figure from D2.1.3 part I.....	14
Figure 3.1-2 The angle of attack distribution along the blade computed with the HAWC2 code.....	15
Figure 3.1-3 The $C_i$ curves for the here airfoils used on the rotor .....	15
Figure 3.1-4 Drawing showing the spanwise positioning of the three airfoils on the blade .....	16
Figure 3.1-5 The horizontal bars show roughly the position of the five stations on the blades where the pressure is measured distribution is measured.....	16
Figure 3.1-6 Blade oil flow visualization on the suction side for a geometric angle of attack of 10.4 deg. and a flow velocity of 60m/s in blade only wind tunnel testing. The influence of the trip tape is seen as the white line on the upper part of the photo. Figure from D2.1.3 part I.....	17
Figure 4.1-1 Pressure distributions for case 1, 325 rpm and 7.59m/s. A comparison of simulations and measurements. ....	20
Figure 4.1-2 Pressure distributions for case 2, 325 rpm and 11.33m/s. A comparison of simulations and measurements. ....	21
Figure 4.1-3 Pressure distributions for case 3, 325 rpm and 18.33m/s. A comparison of simulations and measurements. ....	22
Figure 4.1-4 Pressure distributions for case 4, 425 rpm and 10.0m/s. A comparison of simulations and measurements. ....	23
Figure 4.1-5 Pressure distributions for case 5, 425 rpm and 14.7m/s. A comparison of simulations and measurements. ....	24
Figure 4.1-6 Pressure distributions for case 6, 425 rpm and 24.12m/s. A comparison of simulations and measurements. ....	25
Figure 4.2-1 Blade force distributions along the blade span in comparison with simulations for the cases 1-3 at 325 rpm.....	27
Figure 4.2-2 Blade force distributions along the blade span in comparison with simulations for the cases 4-6 at 425 rpm.....	28
Figure 4.3-1 Comparison of simulated and measure rotor thrust and torque integrated from the pressure distributions. ....	29
Table 3.1-1 – The selected test cases for the validation exercise. ....	14

## Summary

The present report is part II of D2.1.3 “Validation of high rotational speed aerodynamics by wind tunnel tests”. The first part “New MEXICO experiment – Preliminary overview with initial validation” was reported in September 2014. The reason to report the research work in two stages was that the wind tunnel experiment was first carried out between June 20th and July 4th 2014. A selection of the cases for validation of models required some initial analysis and check of the data as contained in part I of D2.1.3.

The specific target with the activities reported in D2.1.3 is validation of the aerodynamic models used for design of the new high tip speed, low induction rotors with new airfoils, specifically within the Innwind project but most of the models are also used by industry today for design and analysis.

Three CFD codes; the compressible code WMB from CENER; the compressible code MaPFLOW from NTUA and the incompressible code EllipSys3D were used in the validation exercise. Then two medium fidelity codes; the vortex code GENUVP from NTUA and the Actuator Line code from DTU were also part of the exercise. Finally, two widely used aeroelastic codes in research and industry; the FAST code and the HAWC2 code were validated.

The comparison of measured pressure distributions with simulations showed overall very good agreement for the 6 data sets representing two rotational speeds and three wind speeds. In particular the prediction of the massive separation at high wind speed was predicted very well. The selected validation cases included tip speeds of 100m/s and there was no clear indication of compressible effects in the measurements. This was confirmed by the simulations.

The blade forces were validated at five radial positions and the biggest scatter between the simulated results were found at the 92%R station where the tip correction plays an important role. Compared with the measured forces there was a systematic over prediction of the normal forces on the mid part of the blade where a Risoe A1-21 airfoil is used. The airfoil has a considerable higher zero lift angle than the neighbouring airfoils but the predicted higher loading was not seen in the measurements.

Finally comparing the integrated forces and moments a surprising fine correlation between the models as well as with the measurements were seen for the torque at the two lowest wind speed cases. As concerns the thrust force the tendency is slightly over prediction of the force.

As an overall conclusion the validation exercise has demonstrated that the codes when compared at the same fidelity level deliver results that are closely correlated and also with the experimental results. It has also been found the CFD codes predict the separated flow conditions quite well and information from such simulations as e.g. airfoil data should be extracted to be used as input in e.g. the aeroelastic codes.

Finally it can be concluded that the measurable set up in the smart D2.1.3 description: “Simulation models validated against the New Mexico data” has been fulfilled.

## CHAPTER 1

### 1.1 Background

The present report is part II of D2.1.3 “Validation of high rotational speed aerodynamics by wind tunnel tests”. The first part “New MEXICO experiment – Preliminary overview with initial validation” was reported in September 2014. The reason to report the research work in two stages was that the wind tunnel experiment was first carried out between June 20th and July 4th 2014. A selection of the cases for validation of models required some initial analysis and check of the data as contained in part I of D2.1.3. Therefore the selected test cases were first available in November 2014. Initial results of comparisons of the experimental data with simulations were circulated in January 2015. However, several rounds of comparisons have afterwards been conducted to reach the final results with confidence to all the data.

### 1.2 Introduction to D2.1.3

The specific target with the activities to be reported in D2.1.3 is validation of the aerodynamic models used for design of the new high tip speed, low induction rotors with new airfoils, specifically within the Innwind project but most of the models are also used by industry today for design and analysis.

The validation is carried out through comparisons with data from the New MEXICO experiment carried out in the DNW wind tunnel in the summer 2014 as mentioned above. The original MEXICO experiment was conducted from December 6<sup>th</sup> to December 14<sup>th</sup> 2006 within the EU FP5 program [1] and comprised detailed aerodynamic measurements on a wind turbine model with a diameter of 4.5 m, which was placed in the largest European wind tunnel, the German Dutch Wind Tunnel, DNW with a size of 9.5 x 9.5 m<sup>2</sup>. The most unique feature of the MEXICO measurements was that the flow field around the rotor plane was measured simultaneously with the blade pressures and forces. The MEXICO project was finished at the end of 2006 very shortly after the measurements were taken.

The analysis of the MEXICO measurements was conducted within the IEA Annexes 29 Mexnext [2] and Mexnext II [3] and it was found that there was a discrepancy between simulated forces on the rotor and the measured flow field with PIV. Clarification of this issue was one of the objectives with the New Mexico measurement campaign. See D2.1.3 part I of the present report for a further discussion of objectives with the New Mexico experiment as well as details on the planning, actual measurements and initial analysis.

## CHAPTER 2 THE MODELS USED IN THE VALIDATION EXERCISE

### 2.1 Introduction

The Innwind partners CENER, NTUA and DTU contributed with simulations from the following codes to the validation exercise:

CENER:

- The aeroelastic code FAST
- The compressible CFD code WMB

NTUA:

- The compressible CFD code MaPFlow
- The aeroelastic vortex code GENUVP

DTU:

- The Actuator Line/Navier-Stokes (ACL) code
- The incompressible CFD code EllipSys3D
- The aeroelastic vortex code HAWC2

There is thus a good variety of model type represented. Three different CFD codes are used where two are compressible and one is incompressible. One of the focus points in the present validation is to investigate if compressible effects can be seen at a tip speed of 100m/s. The actuator line code does not have the shortcomings in the induction computation as the BEM based codes (FAST and HAWC2) but because the model also use airfoil data as input it is an interesting model to compare with the BEM based models. Finally there is the vortex based code GENUVP which also computes the basic flow physics but does resolve the flow over the blades in the same details as a CFD code.

### 2.2 The aeroelastic code FAST

FAST is an aeroelastic simulation code that can model the dynamic response of 2 or 3 bladed horizontal axis wind turbines. It is coupled to the aerodynamic code AeroDyn, which calculates the lift, drag and pitching moment coefficients on each section of the blade as well as the forces on each of the elements along the span. Those forces are lately used by the aeroelastic simulation program FAST to calculate the distributed forces on the turbine blades.

The wind input files for calculations can consist on steady mean winds, steady winds with gusts and/or direction changes, or three-dimensional turbulent winds. For generation of the steady winds the routine IECwind is used, while for the turbulent winds TurbSim is employed. For the present New Mexico data, all winds are steady mean winds: constant and uniform wind fields.

For calculating the induced velocities on the blades, AeroDyn has two models implemented: BEM and a Generalized Dynamic Wake model. For the current work on the Innwind project, the BEM model has been used in all calculations. This model does not include the drag in the calculation of induction, and includes the next corrections:

#### 2.2.1 Tip and Hub corrections

Aerodyn uses a theory originally developed by Prandtl to account for the tip effect. The theory is summarized by a correction factor that is applied to the momentum part of the blade element momentum equations. There also exists the option of using an empirical

relationship based on the Navier-Stokes solutions of Xu and Sankar, which is a correction to the Prandtl model. To account for the hub effects, a hub loss model is used, that has an identical implementation as the Prandtl tip loss model. The user can choose whether to apply the tip and/or hub corrections or not.

### **2.2.2 Correction for turbulent wake**

To correct the local thrust coefficient of the individual blade elements when the basic BEM theory becomes invalid (when induction factor is greater than 0.5), the Glauert correction is implemented in AeroDyn.

### **2.2.3 Skewed wake correction**

When the wind turbine operates at yaw angles relative to the incoming wind direction, AeroDyn uses a correction to account for the skewed wake effect. Such correction is based on a method developed by Pitt and Peters, based on a correction originally developed by Glauert.

### **2.2.4 Dynamic inflow**

The dynamic inflow model of AeroDyn is based on the Generalized Dynamic Wake theory, that is an expanded version of the Pitt and Peters model. It uses a series solution to describe the induced velocity field in the rotor plane, which includes Legendre functions in the radial direction and trigonometric functions in the tangential direction. The current GDW model in AeroDyn employs OP, 1P, 2P and 3P terms. The AeroDyn GDW model is based on the work of Suzuki. The user can choose whether to use the dynamic inflow correction or not. There was not used at MexNext.

The aerodynamic calculations in AeroDyn mentioned above are based on pseudo two-dimensional properties of the local airfoil aerodynamics. For calculating the airfoil aerodynamics, the code has two options:

### **2.2.5 Static airfoil tables**

The static airfoil data are represented by tables of lift, drag and pitching moment coefficients as function of angle of attack and Reynolds number. To determine the aerodynamic coefficients at a particular angle of attack, the linear interpolation is used.

### **2.2.6 Dynamic stall model**

The dynamic stall model included in AeroDyn is based on the work of Beddoes and Leishman, with a modification to allow reproducing aerodynamic coefficients at high angles of attack. In addition, CENER has developed the code DYSTOOL, which has been implemented in AeroDyn. DYSTOOL is also based on the Beddoes-Leishman model with several modifications to improve the results. The main advantage is the possibility to include an optimized set of parameters for each aerofoil or unsteady condition, in order to improve the calculations for the corresponding case. The value of the parameters can be adjusted using an independent tool, based on optimization through a methodology of genetic algorithms, and using experimental or reliable computed data as a baseline. For these calculations, the original dynamic stall model of FAST has been used.

The influence of the tower on the blade aerodynamics is also modelled in AeroDyn. For Mexnext project, as the rotor is far from the tower, the tower model has been disabled in all calculations.

### 2.2.7 Input data used

#### Structural inputs:

Blades are flexible, tower is considered rigid. Flapwise and edgewise stiffness's: calculated using the values in "d00\_ExperimentDescriptionMexico\_version\_6.xls-BladeStructure", and multiplying them by the material's Modulus of Elasticity, taken as:  $73.42 \times 10^9$  N/mm<sup>2</sup> (Aluminium 7075-T651 Alloy). The blade has been defined by 26 stations.

#### Aerodynamic inputs:

Stall model: Steady. The conditions of the tests seem suitable for a steady computation (yaw=0°, constant wind, tower effect not considered)

Inflow model: Considers that the stall is completely developed at each time instant. As we don't have any transitory, this is the model that best suits our case

Enable the calculation of the axial and tangential inductions

Tip and hub loss models enabled: PRANDTL

Tower shadow model disabled.

#### Aerodata:

CYLINDER: used a cylinder with a drag coefficient of 1. (For a clean cylinder, CD at 24m/s is around 0.7, and at 10m/s is around 1.3. We have taken an average value. Tower shadow model disabled.

2D Profile information of DU and NACA taken as distributed in the project, but the curves have been softened to eliminate discontinuities in the whole range -180;180

RISO airfoil: a CFD (WMB) polar for Re=700.000 has been used instead of the original data.

## 2.3 The compressible CFD code WMB

The Wind Multi-Block (WMB) code, developed at Liverpool University in collaboration with CENER, is used for the present work, and has so far been validated for wind turbine applications [4], using the NREL UAE Phase VI experiments [5] as well as the pressure and PIV data of the MEXICO project [6].

WMB solves the Navier-Stokes equations in integral form using the arbitrary Lagrangian Eulerian (ALE) formulation for time-dependent domains with moving boundaries. For steady rotor simulations, as has been the case for these simulations, where just a 120degree domain was modelled, the grid is not rotating. A source term is added to compensate for the inertial effects of the rotation along with a velocity assigned to grid nodes.

The Navier-Stokes equations are discretised using a cell-centred finite volume approach on a multi-block grid. Osher's [7] upwind scheme is typically used for the discretisation of the convective terms and MUSCL [8] variable extrapolation is used to provide higher order accuracy. The linearised system is solved using the generalised conjugate gradient method with a block incomplete lower-upper (BILU) pre-conditioner [9].

The WMB solver has a library of turbulence closures which includes several one- and two-equation turbulence models and for the current simulation, Menter's  $k-\omega$  SST has been used.

Multi-block structured meshes are used for WMB. These meshes are generated using ICEMCFD of ANSYS. The multi-block topology allows for an easy sharing of the calculation load for parallel computing. In this case, the mesh that was created for flow analysis had 40 million cells. The span- and chord-wise cell distribution was of 351 and 414 and the computational domain boundaries were located at 6R - Inflow, 12R - Outflow and 5R - Far-field. The hub of the rotor was also modelled in the simulations but not the tower.

## 2.4 The compressible CFD code MaPFlow

MaPFlow [10] is a multi-block MPI enabled compressible solver equipped with preconditioning in regions of low Mach flow. The discretization scheme is cell centered and makes use of the Roe approximate Riemann solver [11] for the convective fluxes. In space the scheme is 2nd order accurate defined for unstructured grids and applies the Venkatakrishnan's limiter [12]. The scheme is also second order and implicit in time introducing dual time stepping for facilitating convergence. The final system of equations is solved with an iterative Gauss-Seidel method using the Reverse Cuthill-Mckee (RCM) reordering scheme [13]. The solver is equipped with the Spalart-Allmaras (SA) and  $k-\omega$  SST eddy viscosity turbulence models.

For the 425 rpm cases a mesh of 5 million cells was implemented. The blade was discretized with 304 cells around the airfoil surface and 200 cells in the spanwise direction. A grid independence analysis was made for the 10m/s case by refining the mesh from the blade and outwards using 3 different grid densities of 5,8 and 11 million cells. It was concluded that the mesh of 5 million cells is sufficient for the prediction of the pressure distributions / loads, but not sufficient to reproduce the velocity field measurements due to increased diffusion. Therefore, the mesh of 8 million cells was adopted for the simulation of the 325 rpm cases. Blade discretization was made using 304x179 cells.

Simulations were steady state in the rotating frame of reference using one third of the original wind turbine geometry, thus simulating the flow around one blade out of the three. Periodic boundary conditions at the boundaries of the computational domain were applied. The CFL was increased linearly from 1 to a maximum of 20 at 500 time steps in order to accelerate convergence. In that way a full convergence was achieved at 5000-6000 time step iterations.

## 2.5 The Actuator Line/Navier-Stokes (ACL) code

### 2.5.1 The Navier Stokes solver

The EllipSys3D code is used as the Navier-Stokes solver. The EllipSys code was developed at the Department of Wind Energy, Technical University of Denmark (DTU). The code is based on a multi block/cell-centered finite volume discretization of the steady/unsteady incompressible Navier-Stokes equations in primitive variables (pressure-velocity). The predictor-corrector method is used. In the predictor step, the momentum equations are discretized using a second-order backward differentiation scheme in time and second-order central differences in space, except for the convective terms that are discretized by the QUICK upwind scheme. In the corrector step, the improved Rhie-Chow interpolation is used in order to avoid numerical oscillations from pressure decoupling. Since there is no optimal value for the SIMPLE algorithm for unsteady flow computations, the solution is

slightly dependent on the relaxation parameters and the time-step. In order to make it more consistent, the improved SIMPLEC scheme for collocated grids is used. Using the scheme the solution is independent of the relaxation parameter and the time-step. The obtained Poisson pressure equation is solved by a five-level multi-grid technique. Since the EllipSys3D code is programmed using a multi-block topology, it can be parallelized relatively easily using Message Passing Interface (MPI). The turbulence model used for Large Eddy Simulation is the mixed scale turbulence model developed at LIMSI

$$\nu_t = C \left| \bar{\omega} \right|^\alpha k^{(1-\alpha)/2} \Delta^{(1+\alpha)}$$

where  $\Delta = (\Delta_x \Delta_y \Delta_z)^{1/3}$  is an average grid size, and  $\alpha = 0.5$ . Assuming similarity between two grid levels, the turbulent kinetic energy can be estimated by using the following filter

$$k = \frac{1}{2} \sum_{j=1}^3 (U_j - \bar{U}_j)^2 \approx \frac{1}{2} \sum_{j=1}^3 (\bar{U}_j - \tilde{\tilde{U}}_j)^2$$

where  $\tilde{\tilde{U}}_j$  is the filtered velocity of the resolved velocity,  $\bar{U}_j$ , by the second filter, i.e. the double filtered velocity.

### 2.5.2 The actuator Line technique

To determine the body forces on the rotor blades, we use a blade-element approach combined with airfoil characteristics. The computational domain is chosen to be fixed with the ground and three rotating blades are represented with a rotating body force. At each time step, the flow solver gives a Cartesian velocity field. The velocity at a given blade position is calculated by identifying the index of blade position and performing a tri-linear interpolation. In order to find the loading, the obtained velocity is transformed into polar velocity  $(V_r, V_\theta, V_z)$  with the origin located at the rotor centre. Since the rotor is rotating with an angular velocity  $\Omega$ , the flow angle is determined as

$$\phi = \tan^{-1} \left( \frac{V_z}{\Omega r - V_\theta} \right)$$

The angle of attack at each cross section is defined as  $\alpha = \phi - \gamma$  where  $\gamma$  is the sum of local twist and pitch angles on the rotor. The relative velocity is

$$V_{rel} = \sqrt{V_z^2 + (\Omega r - V_\theta)^2}$$

The force per spanwise unit length is

$$\vec{f}_{2d} = \frac{d\vec{F}}{dr} = \frac{1}{2} \rho V_{rel}^2 c (C_l \vec{e}_L + C_d \vec{e}_D)$$

where  $C_l = C_l(\alpha, Re)$  and  $C_d = C_d(\alpha, Re)$  are the lift and drag coefficients, respectively. The airfoil data obtained directly from 2D measurements or computations need to be corrected for rotational effects caused by Coriolis and centrifugal forces, especially for cross-sections near the root. At the same time, airfoil cross-sections near the blade tip are influenced from the fact of pressure equalization from the pressure and suction sides at the tip such that the tip flow is different from the corresponding 2D flow at the same angle of attack. To take into account these effects, a function  $F_1$  is applied on the 2D airfoil data. The function is

$$F_1 = \frac{2}{\pi} \cos^{-1} \left[ \exp \left( -g \frac{B(R-r)}{2r \sin \phi} \right) \right]$$

where B is number of blades and the function g is

$$g = \exp(-0.125(B\Omega R/U_{\infty} - 21)) + 0.1$$

The g function adjusts the influence of the tip vortices on the pressure distribution in the blade tip region. The number of blades, B, determines the distance between the tip vortices at a fixed tip speed ratio whereas the tip speed ratio,  $\Omega R/U_{\infty}$ , determines both the distance between the tip vortices at a fixed number of blades, and the pitch of the vortex structure. Their influences on the pressure distribution on the blade are similar and thus are considered together in the g function. The obtained 2D force is put into a polar or Cartesian regularized volume force.

The tower nacelle is not included in the computations. The open tunnel is included to study the tunnel effects. For more information, the reader is referred to [14].

A Cartesian mesh of 11.8 M mesh points is used in a domain of  $[-16R, 16R] \times [-16R, 16R] \times [-16R, 16R]$  where 120x120x240 cells are uniformly distributed in a domain near the rotor  $[-2R, 2R] \times [-2R, 2R] \times [-2R, 4R]$  with the finest mesh of  $R/30$  where R is the rotor radius is used.

The inflow and lateral boundary conditions are specified with the uniform velocity whereas at the outlet convective boundary condition is used. The blade is divided into 30 elements in the actuator line model. The Beddoes-Leishman type dynamic stall model has been implemented in the code. No inflow or tower shadow models are included.

## 2.6 The incompressible CFD code EllipSys3D

EllipSys3D is an in-house incompressible finite volume Reynolds-Averaged Navier-Stokes (RANS) flow solver developed at DTU, see [15], [16], [17]. The flow variables are collocated in the mesh to facilitate complex mesh geometries. The SIMPLE algorithm is used to solve the Navier-Stokes equations, see [18]. The pressure correction equation is solved using the Rhie-Chow algorithm to avoid odd/even pressure decoupling, see [19] and is accelerated by a multi-grid technique. The convective terms are discretized using the QUICK scheme, as given by [20]. The system is parallelized in a multi-block structure, where the problem can be distributed across multiple processors. The communication of data between each processor is done through the MPI libraries. Both fully turbulent simulations and transitional computations can be performed using the Menter's  $k - \omega SST$  model described in [21]. To account for transition the code features the e-correlation based transition model of Menter et al. [22] or using the Drela-Giles bypass transition model [23]. No inflow or tower shadow models are included.

In the present investigation, the EllipSys3D code is used in the steady state mode, simulating the movement of the rotor using the 'Steady State' moving mesh option [24], and modeling fully turbulent flow using the k-omega SST model. The grid size is ~28 million cells, describing only the actual rotor geometry, neglecting the tower and nacelle, more details about the actual grid can be found in [25].

## 2.7 The aeroelastic code HAWC2

The HAWC2 code is an aeroelastic model intended for calculating wind turbine response in time domain [26]. The core of the code was mainly developed within the years 2003–2007 in the Aeroelastic Design Research Program at Risø, National Laboratory, Denmark, but is continuously being updated and improved. The structural part of the code is based on a multi-body formulation as described in Shabana [27] using the floating frame of

reference method. In this formulation, the wind turbine main structures are subdivided into a number of bodies, where each body is an assembly of Timoshenko beam elements. Each body includes its own coordinate system with the calculation of internal inertia loads when this coordinate system is moved in space; hence, large rotation and translation of the body motion are accounted for. Inside a body, the formulation is linear, assuming small deflections and rotations. This means that a blade modelled as a single body will not include the same nonlinear geometric effects related to large deflections of a blade divided into several bodies. The bodies, representing the mechanical parts of the turbine, are connected by kinematic constraints. The constraints are formulated as algebraic equations, which impose limitations of the bodies' motion. Examples of such constraints are a fixed connection from a structural node to a global point (e.g. tower bottom clamping), a fixed coupling of the relative motion (e.g. fixed pitch, yaw), a frictionless bearing and a bearing where the rotation angle is controlled by the user. It may be worth to notice that also for the last constraint where the rotation is specified externally, inertial forces related to this movement are accounted for in the response. External forces are placed on the structure in the deformed state, which is especially important for pitch loads and twist of the blades, and since large rotations are handled by a proper subdivision of bodies, the code is suited for calculations on very flexible turbines subjected to, e.g. large blade deflections. The structural model is general, but in its simplest form, a turbine is modelled using one body for the tower, one for the nacelle and one for each blade.

The aerodynamic part of the code is based on the blade element momentum (BEM) theory, but implemented so that induced velocities are calculated on the basis of the local inflow velocities causing different inductions over the rotor disc as in the case of a large wind shear [28]. Sub models are implemented to handle dynamic inflow, dynamic stall, skew inflow, shear effects on the induction and effects from large deflections. The dynamic stall model [29] is a modified Beddoes–Leishmann model [30] that includes the effects of shed vorticity from the trailing edge as well as the effects of stall separation lag caused by an instationary trailing edge separation point.

A Newmark-beta solution scheme together with Newton–Raphson iterations within each time step is used for time integration. The calculation time is approximately a factor of 1–2 slower than real time on a 3 GHz CPU.

## CHAPTER 3 THE SIMULATION CASES

### 3.1 Description of cases

The complete test matrix from the New MEXICO measurements in 2014 comprised many different turbine configurations with variations of pitch, rpm and with different add-ons, Figure 3.1-1. For the present initial validation exercise, six cases with axial, uniform inflow conditions were selected, Table 3.1-1.

Test type	Velocity verification	Loads vs velocity	Standstill	Axial flow (pressure)	PIV	Dynamic inflow	Yawed flow (pressure)	Blade add-ons	Pitch misalignment	Flowviz	Blade-off	
DEMO	x	x	x	x	x	x	x	x	x	(x)	(x)	
Balance	x	x	x	x	x	x	x	x	x	x	x	
Apparatus	PIV traverse	(+ pitot) radial	axial radial		axial radial							
Mics Array	x	x	x	x	x	x	x	x	x	x	x	
Model config <sup>1</sup>	0	0	0, 3	3	3	3	3	1, 2, 4, 5	3, 7	6	99	
Operational condition	Pitch angle [°]	90	-5.3→1.7	-2.3→90	-5.3→1.7	-2.3	-2.3 Steps	-2.3,0.7	-5.3→1.7	-5.3→20	-2.3, 73.6	NA
	Yaw angle [°]	0	0	-90→+30	0	-30,0,30	0,15,30	-30→+45	0	0	0	-30→+30
	Rot. speed [rpm]	0	324,424	0	324,424	424	324,424 Ramp	424	0,324,424	324	0,324,424	0,324,424
	$U_{ref}$ [m/s]	10→30	7.5→24	30	5→30	10,15,24	10,15,18	10,15,18,24	5→30	-5→15	15,18,30	10→30

Figure 3.1-1 The overall test matrix for the New MEXICO experiment. Figure from D2.1.3 part I.

Case	Run no.	V [m/s]	Rpm.	Pitch [deg.]	Lambda
1	323	7.59	324.9	-2.3	10.08
2	324	11.33	324.9	-2.3	6.76
3	326	18.33	324.9	-2.3	4.18
4	265	10.00	425.1	-2.3	10.02
5	266	14.7	425.1	-2.3	6.81
6	267	24.12	425.1	-2.3	4.15

Table 3.1-1 – The selected test cases for the validation exercise.

The three cases at 425 rpm were selected for studying the flow conditions at the highest achievable tip speed of 100m/s. This is above the tip speed of most MW turbines today but the design studies in the Innwind project comprise such tip speeds and also above. The three 325 rpm cases were then selected as the tip speed ratio is almost the same as for the 425 rpm cases as seen in Table 3.1-1. It means that the influence on non-dimensional coefficients such as the thrust coefficient or the airfoil pressure coefficients is

due to Reynolds number and/or Mach number effects. Also the angle of attack AoA distribution along the blade will then be the same for the three wind speeds at 325 rpm and at 425 rpm, respectively, as shown in Figure 3.1-2.

When the AoA distribution for the three wind speeds are correlated with the  $C_l$  polar for the three airfoils used on the blade as shown in Figure 3.1-3 it can be seen that at the lowest wind speed the AoA is below 5 deg. and we operate in the linear  $C_l$  vs. AoA region. Also for the middle wind speed most of the rotor will operate below stall while at the highest wind speed massive stall will be present.

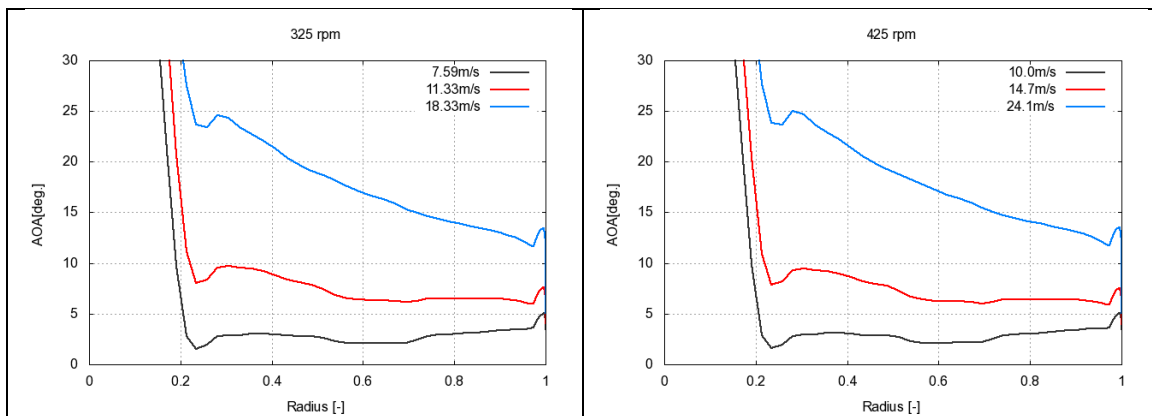


Figure 3.1-2 The angle of attack distribution along the blade computed with the HAWC2 code.

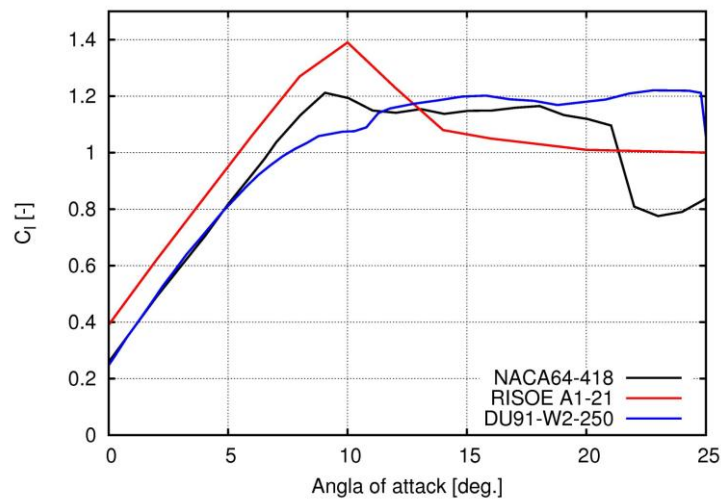


Figure 3.1-3 The  $C_l$  curves for the three airfoils used on the rotor

The positioning of the three different airfoils used on the blade are shown in Figure 3.1-4 and Figure 3.1-5. It can be seen that there are transition zones between the three different airfoils where in particular the Risoe A1-21 airfoil has a quite higher zero lift than the two other airfoils as can be seen in Figure 3.1-3

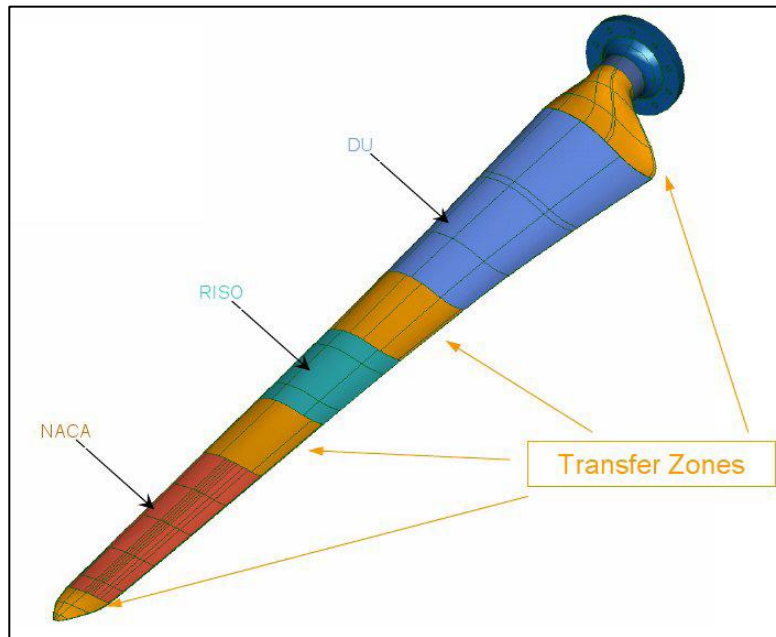


Figure 3.1-4 Drawing showing the spanwise positioning of the three airfoils on the blade

Station nr	Span <sup>‡</sup> [m]	Chord [m]	Twist [°]	Chordwise location of AC <sup>†</sup> [m]	Profile name
1	0.000	0.195	0.000	-0.049	Cylinder
2	0.020	0.195	0.000	-0.049	Cylinder
3	0.025	0.090	0.000	-0.023	Cylinder
4	0.090	0.090	0.000	-0.023	Cylinder
5	0.165	0.165	8.200	-0.011	Transition (0.090 m to 0.240 m)
6	0.240	0.240	16.400	0.000	DU91-W2-250
7	0.465	0.207	12.100	0.000	DU91-W2-250
8	0.690	0.178	8.300	0.000	DU91-W2-250
9	0.815	0.166	7.100	0.000	DU91-W2-250
10	0.915	0.158	6.100	0.000	Transition (0.815 m to 1.015 m)
11	1.015	0.150	5.500	0.000	RISØ A1-21
12	1.140	0.142	4.800	0.000	RISØ A1-21
13	1.265	0.134	4.000	0.000	RISØ A1-21
14	1.365	0.129	3.700	0.000	Transition (1.265 m to 1.465 m)
15	1.465	0.123	3.200	0.000	NACA64-418
16	1.590	0.116	2.600	0.000	NACA64-418
17	1.815	0.102	1.500	0.000	NACA64-418
18	1.955	0.092	0.700	0.000	NACA64-418
19	1.983	0.082	0.469	0.000	NACA64-418
20	2.012	0.056	0.231	0.000	NACA64-418
21	2.040	0.011	0.000	0.000	NACA64-418

Figure 3.1-5 The horizontal bars show roughly the position of the five stations on the blades where the pressure is measured distribution is measured.

It should also finally be noticed that the selected cases have the model configuration number of 0 as seen in Figure 3.1-1. It means that the flow over the blade is tripped. The strips had a width of 5 mm and a thickness of 0.2mm. The chordwise position of the strips was at 10%chord for both pressure and suction side of the blades. An example of the flow over the blade in the wind tunnel testing of the blades before the rotor testing can be seen in Figure 3.1-6 where the white line at the top is the transition line of the flow.

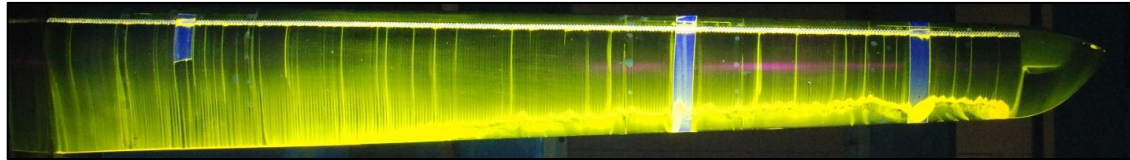


Figure 3.1-6 Blade oil flow visualization on the suction side for a geometric angle of attack of 10.4 deg. and a flow velocity of 60m/s in blade only wind tunnel testing. The influence of the trip tape is seen as the white line on the upper part of the photo. Figure from D2.1.3 part I

## CHAPTER 4 RESULTS

### 4.1 Pressure distributions

Comparisons of simulated and measured pressure distributions are shown in Figure 4.1-1 to Figure 4.1-6.

Overall, the three wind speeds represent three different operational regimes as mentioned in the previous section:

1. At the lowest wind speed the thrust coefficient is high and thus also the induction. Operation is on the linear part on the  $C_t$  vs. AoA curve along the whole blade.
2. At the middle wind speed the rotor operates at an optimal loading and induction. On most of the blade operation is still below stall.
3. At the highest wind speed a major part of the flow over the airfoils separates and there is deep stall.

#### 4.1.1 Low wind speed cases at both 325 rpm and 425 rpm

At the most inboard radial position at 25%R there is a big scatter in the experimental data which is caused by the fact that the dynamic pressure is very low compared with the operational range of the kulite pressure sensors. This is discussed in D2.1.3 part I.

Further outboard at the Risoe airfoil at 60%R the codes generally overestimate the suction on the front part of the airfoil. There are also some deviations between the results of the codes.

For the two most outboard sections with the NACA64-418 airfoil the correlation between simulated and measured pressure distributions is almost perfect and in particular for the results from the three CFD codes.

#### 4.1.2 Middle wind speed cases at both 325 rpm and 425 rpm

There is still scatter in the experimental data at the 25% position but at the 35% position the scatter in the measured data are now much less than before and the correlation with measurements is quite good. At the 60% station the tendency is the same as before with an overestimation by the codes of the suction on the front part of the airfoil.

Again there is a very good correlation between experiment and simulations on the two outboard stations although the EllipSys3D code shows some irregularities in the pressure distribution and in particular at the 92% position at 325 rpm. A detailed look at the streamlines showed that the cause is a small separation bubble at that spanwise position trailing two counter-rotating vortices.

#### 4.1.3 High wind speed cases at both 325 rpm and 425 rpm

As indicated in Section 3 the AoA is now so high that massive separation must be expected and this is also seen in the simulations at all radial stations by a flat pressure distribution on the suction side from the trailing edge towards the leading edge. Overall the CFD codes predict the pressure distributions very well in spite of the complex flow with massive separation. However, the distributions at the 25% and 35% positions were not predicted well for the lowest rotational speed by WMB code. The none-fully converged

solution was similar to the experiments, but the converged solution moved to a fully stalled inboard region. Finally, the pressure distributions by the vortex code GENUVP show some deviations from experimental data.

#### **4.1.4 General comments to comparison of pressure distributions**

When pressure is compared, the 82%R and 92%R stations of the 425rpm case and the 92%R station of the 325rpm cases experienced Mach numbers of 0.2 and above. It cannot be said that the agreement between the compressible CFD methods compared here is closer between them than with respect to the incompressible one. However, the incompressible solver shows a different pressure distribution predictions in the regions where the flow has a higher local speed.

### 4.1.5 Pressure distributions at 325 rpm

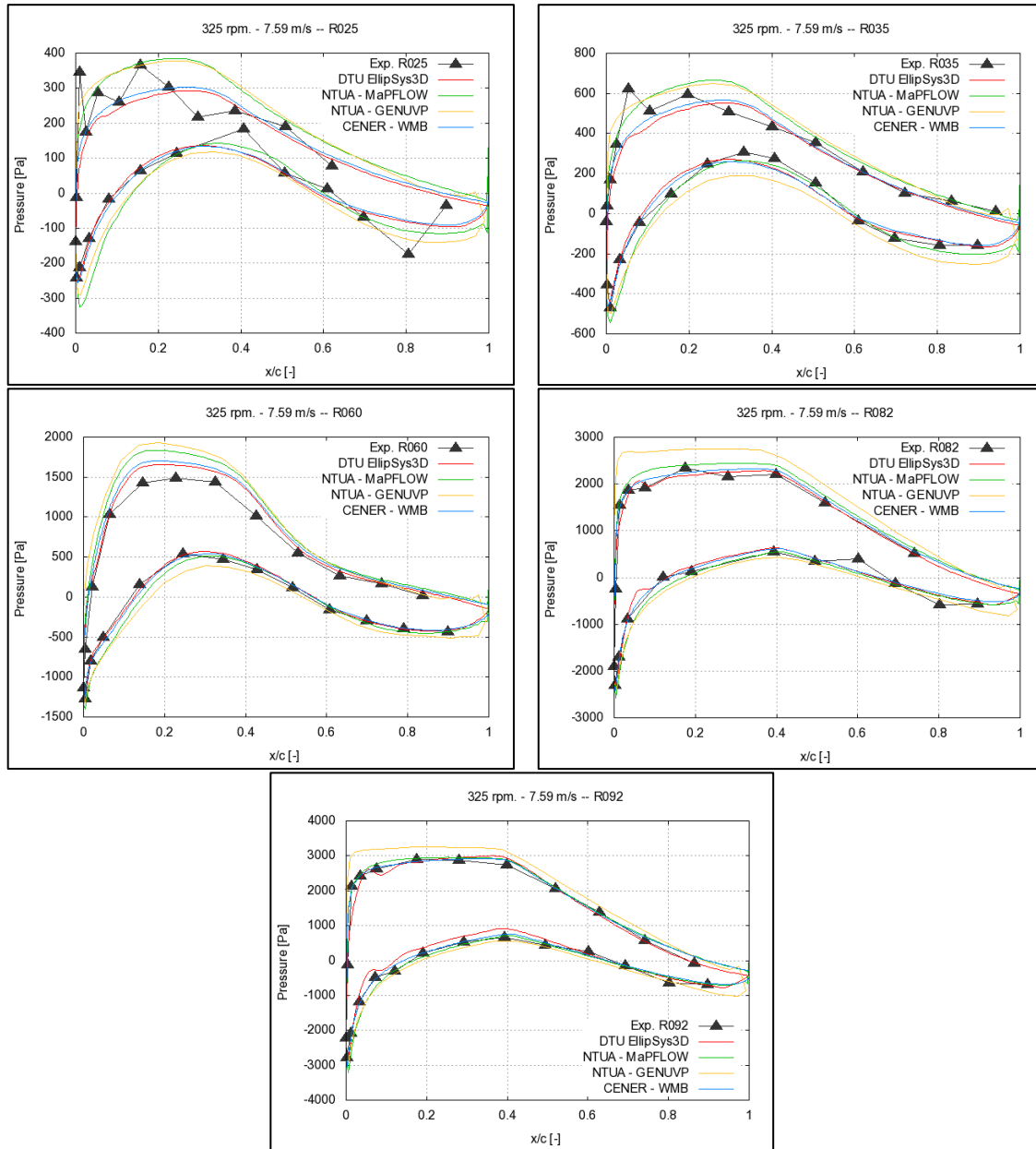


Figure 4.1-1 Pressure distributions for case 1, 325 rpm and 7.59m/s. A comparison of simulations and measurements.

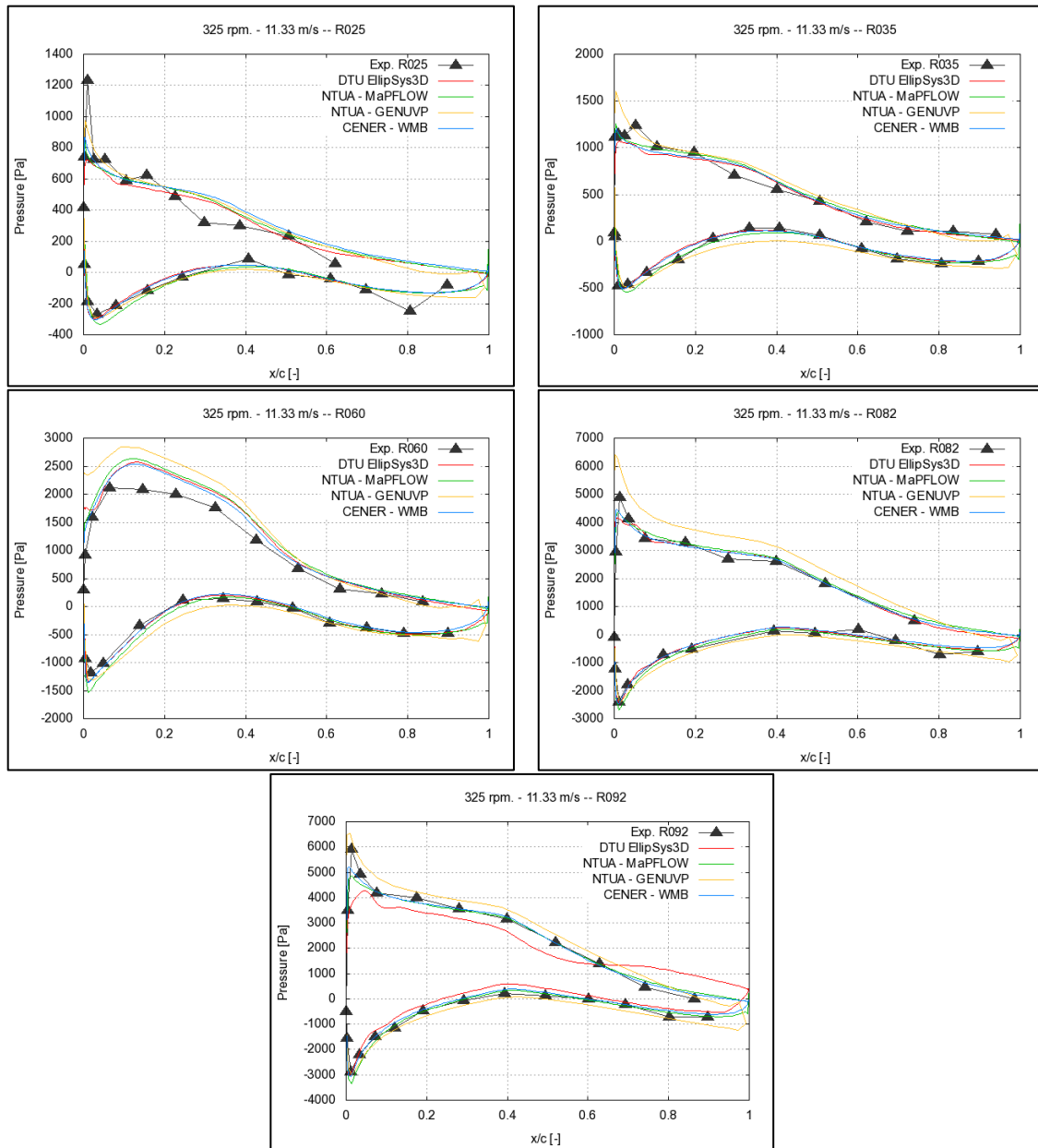


Figure 4.1-2 Pressure distributions for case 2, 325 rpm and 11.33m/s. A comparison of simulations and measurements.

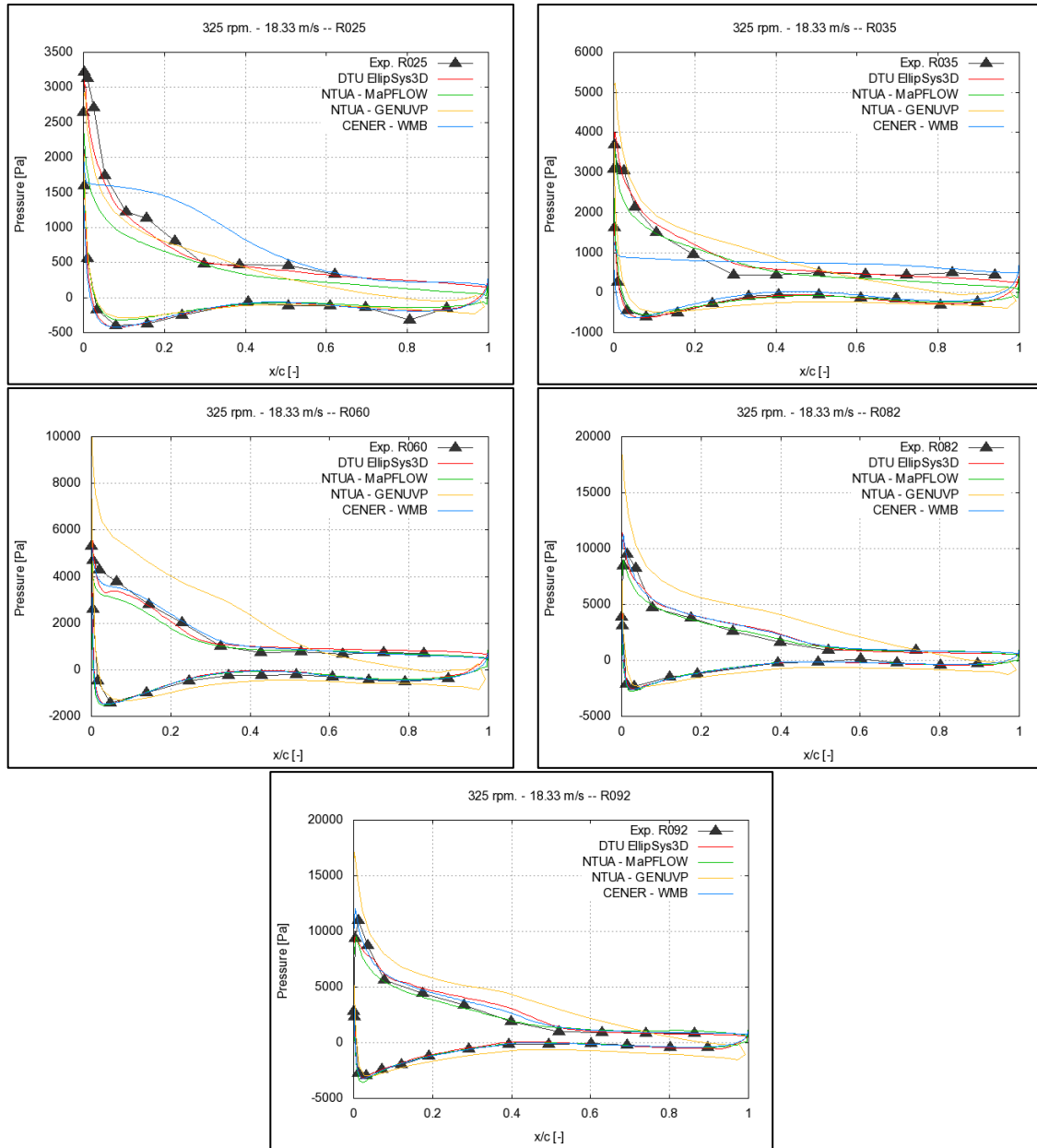


Figure 4.1-3 Pressure distributions for case 3, 325 rpm and 18.33m/s. A comparison of simulations and measurements.

### 4.1.6 Pressure distributions at 425 rpm

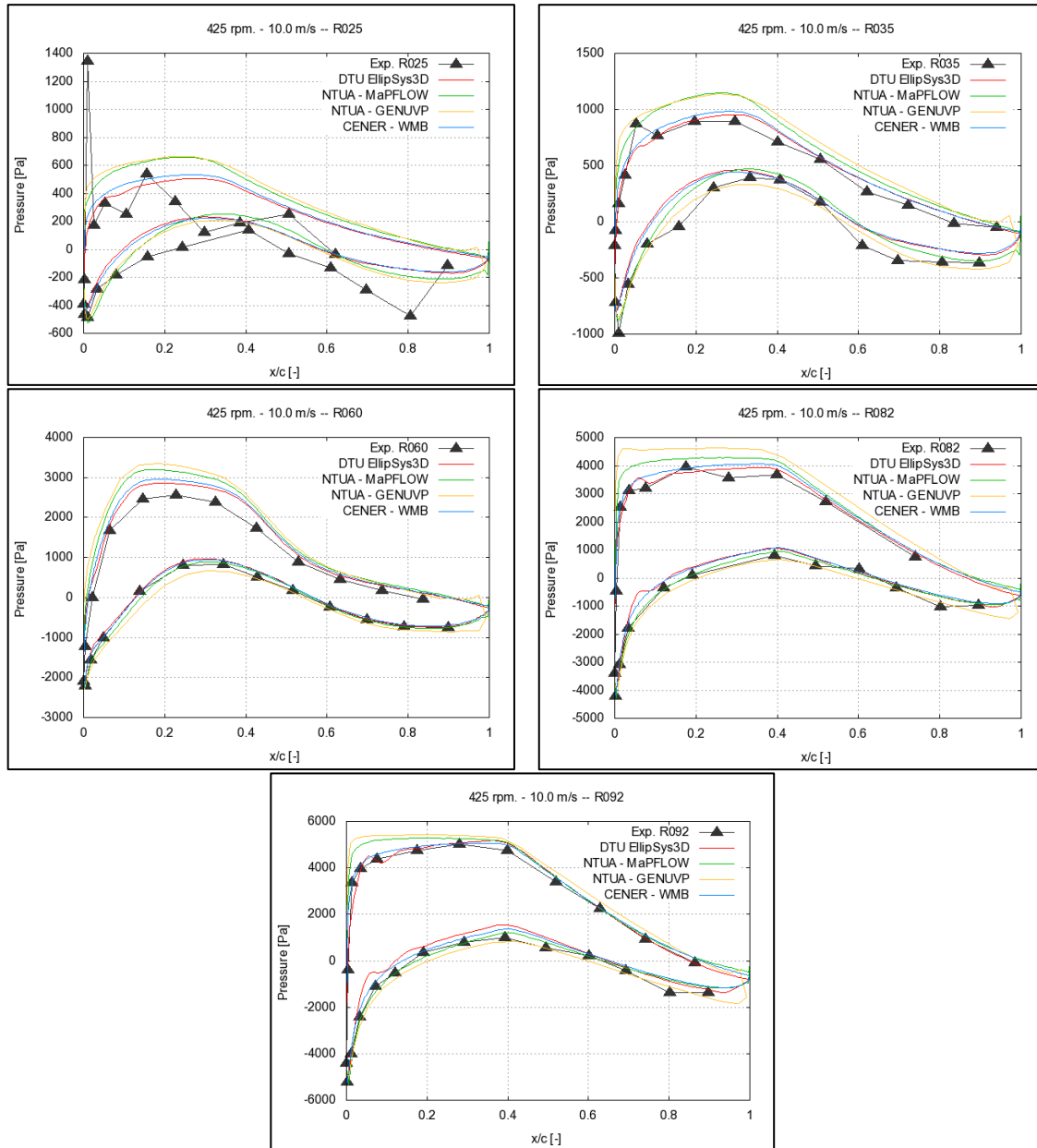


Figure 4.1-4 Pressure distributions for case 4, 425 rpm and 10.0m/s. A comparison of simulations and measurements.

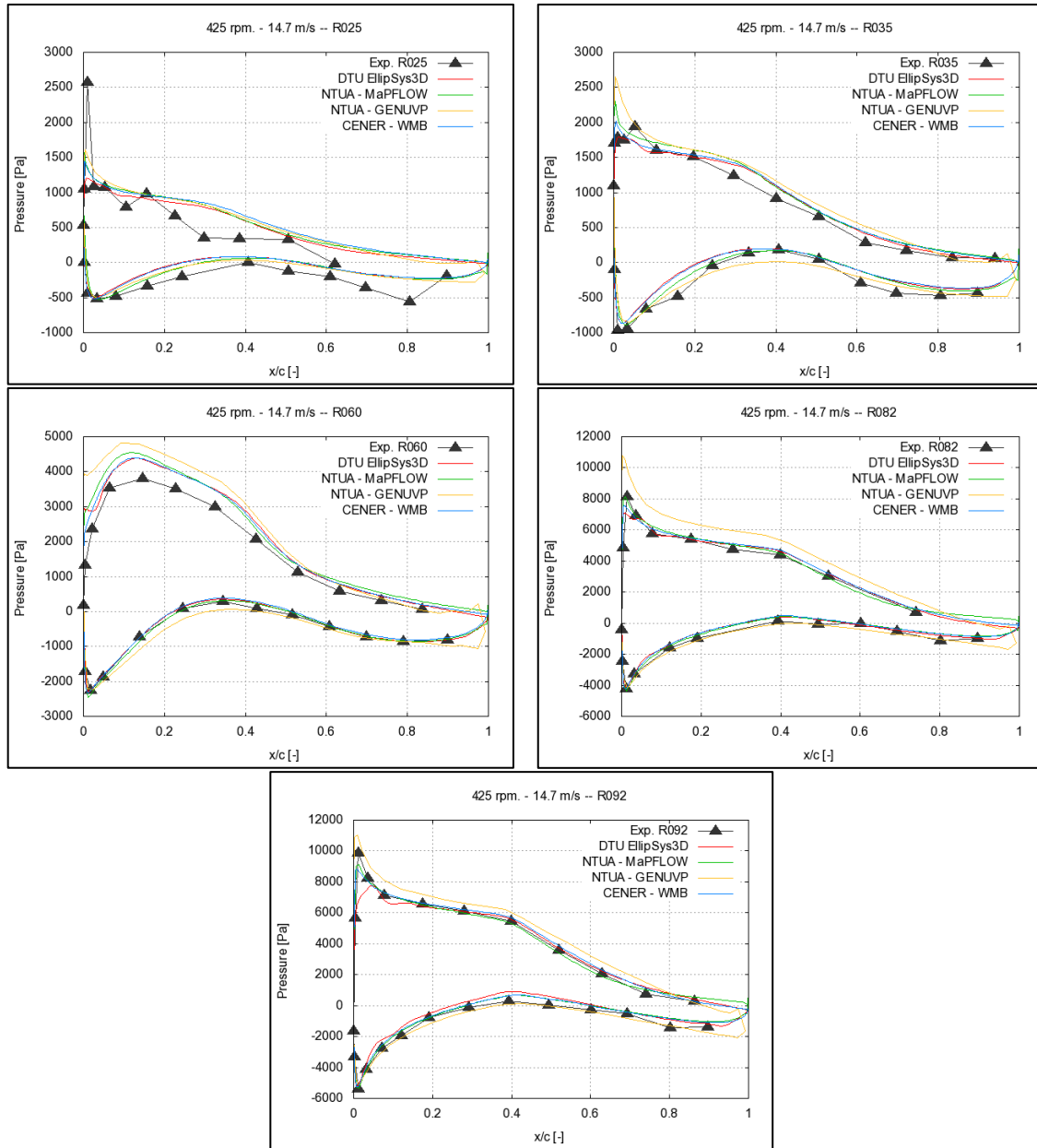


Figure 4.1-5 Pressure distributions for case 5, 425 rpm and 14.7m/s. A comparison of simulations and measurements.

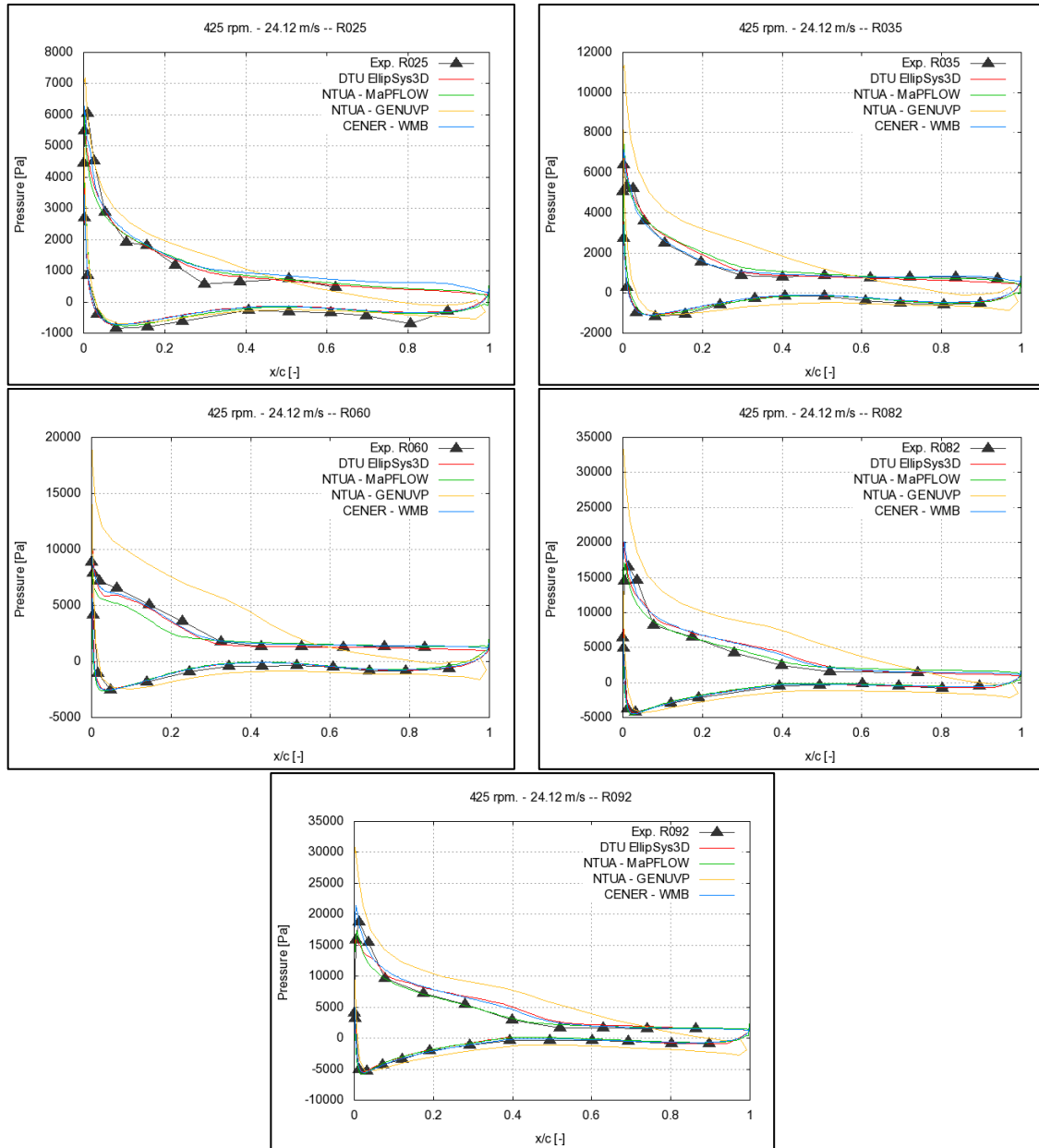


Figure 4.1-6 Pressure distributions for case 6, 425 rpm and 24.12m/s. A comparison of simulations and measurements.

## 4.2 Radial blade force distributions

### 4.2.1 Comments on the blade force distributions

The blade force distribution along the blade span is shown in Figure 4.2-1 at 325 rpm and in Figure 4.2-2 for 425 rpm and in both cases at the three different wind speeds. For the CFD codes the forces are integrated from the simulated pressure distributions. The same is true for the measurements. However, due to the much fewer pressure ports in the measured pressure distribution and the use of a linear interpolation between the pressure ports this is a source of uncertainty of the integrated forces as discussed on page 42-49 in D2.1.3 part I. CFD predictions of spanwise loads reduces when the experimental measurements resolution is used instead the available CFD resolution.

For the normal forces there is a good correlation between all the models and also for most radial position with the measured forces. However, the increase in loading that should be expected from the higher zero lift for the Risoe airfoil and also clearly predicted by e.g. the WMB code is not confirmed by the measurements. The measured loading shows the opposite with a slightly decrease. The cause of the deviations was explored by the pressure distributions shown in the previous section where the tendency was an over prediction of the suction on the front part of the airfoil. However, the causes of this are not clear but the wind tunnel testing of the blade prior to the rotor testing showed also considerable deviations from the original wind tunnel tests on the Risoe airfoil as seen in Figure 9 on page 25 of D2.1.3 part I. Maybe the difference in Reynolds number can be a major effect.

There is some scatter in the results at the outboard section with a tendency to an over prediction in loads. This is the station where the tip correction is most important and this could be the basis for adjustment of the tip correction models.

For the highest wind speed at both 325rpm and 425 rpm the flow over the blade is separated over a major part of the blade and combined with the blade rotation and spanwise pressure gradient this causes strong 3D effects. The CFD codes capture the increased loading on the inboard part of the blade due to the 3D flow effects quite well.

Although the tangential loading is quite small there is overall a good correlation with the model predictions. However, for the most in board station the measured tangential force is systematically above the predictions. It could be due to a speed up effect from the hub but most likely due to the considerable scatter in the measured pressure distributions.

Again the CFD codes, with exception of the WMB code at 325rpm, capture the increased tangential loading due to 3D flow effects quite well when compared with the other codes using 2D airfoil data.

### 4.2.2 Radial blade force distributions – 325 rpm.

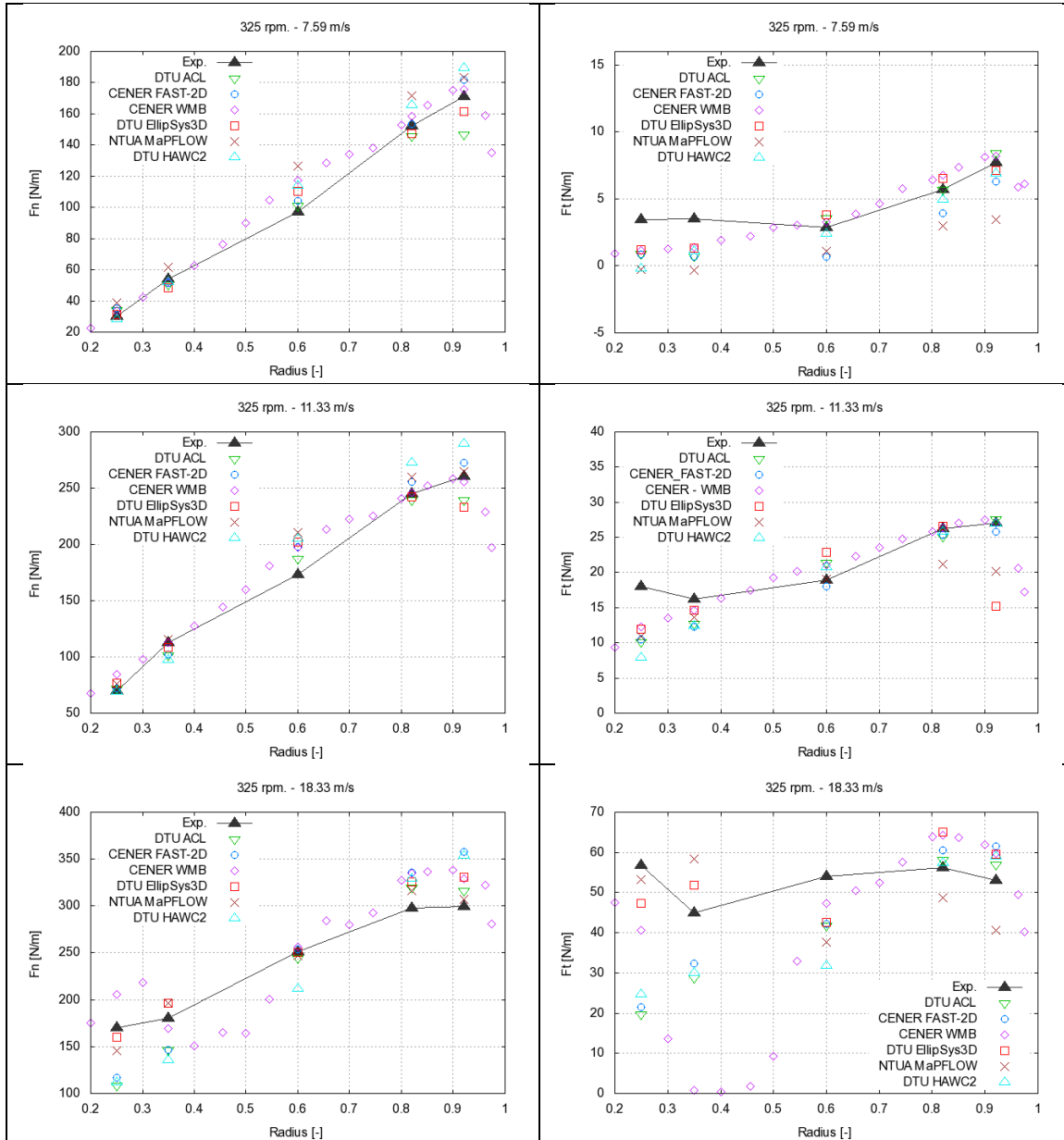


Figure 4.2-1 Blade force distributions along the blade span in comparison with simulations for the cases 1-3 at 325 rpm.

### 4.2.3 Radial blade force distributions – 425 rpm.

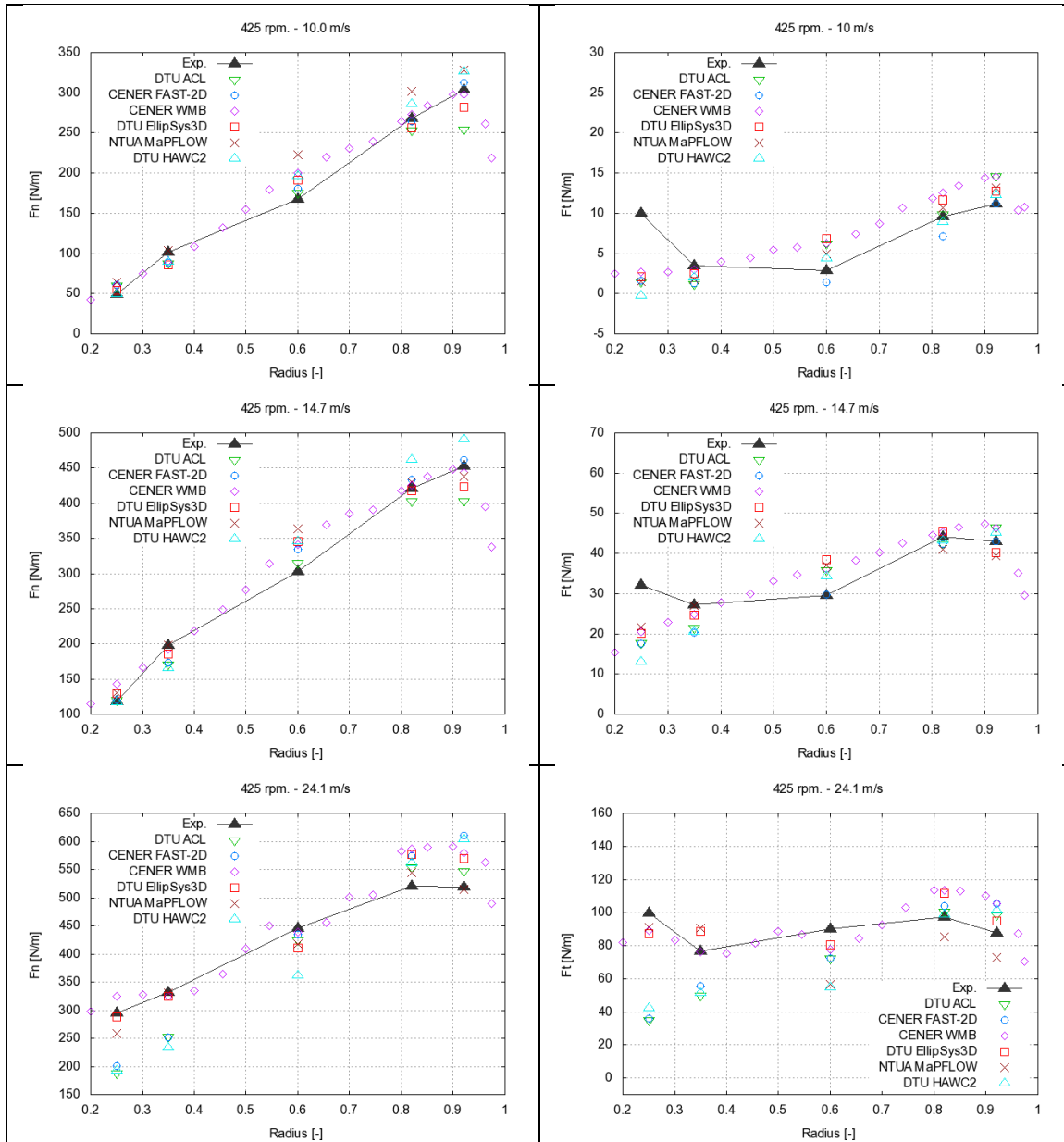


Figure 4.2-2 Blade force distributions along the blade span in comparison with simulations for the cases 4-6 at 425 rpm

### 4.3 Integrated rotor forces from pressure distributions

The integrated rotor thrust force and rotor torque shown in Figure 4.3-1 are integrated on basis of the blade force distributions shown in the previous section. The same is also done for the measured forces but as there are only five radial stations this will cause an underestimation of the experimental load as discussed on pages 42-49 in D2.1.3 Part I. An estimate of a 6% reduction has been derived and corrected experimental results with a correction factor of 1.06 are also shown in Figure 4.3-1.

When comparing the measured and simulated thrust there is a tendency of an overestimation of the thrust even with the corrected experimental results. One major contribution is probably the over predicted axial loading from the blade region with the Risoe airfoil.

Surprisingly, the torque at the two lowest wind speeds show a very small variation between the codes and also correlates very well with the measured torque. It was shown in the previous section that the tangential forces are much lower than the axial forces and therefore the small scatter on the torque was not foreseen. Finally, it should be noted again that the CFD codes predict the torque quite well in comparison with experiment.

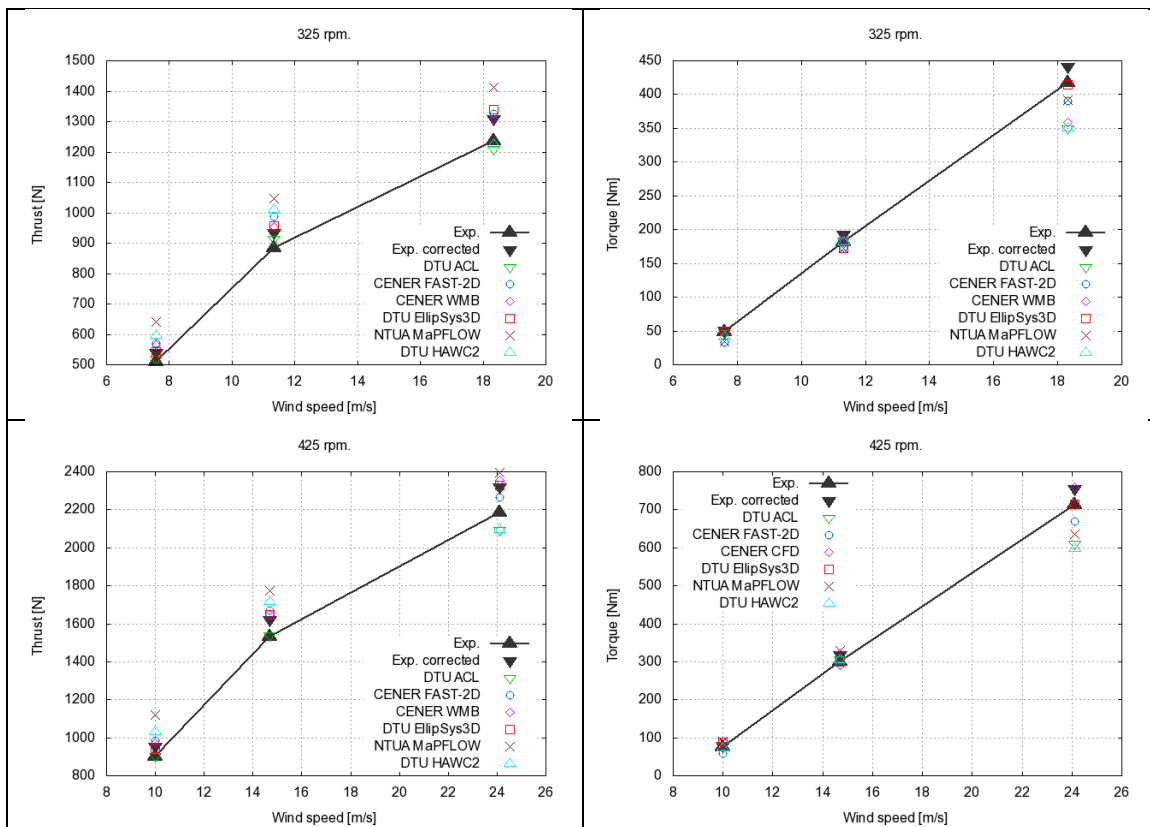


Figure 4.3-1 Comparison of simulated and measure rotor thrust and torque integrated from the pressure distributions.

## CHAPTER 5 CONCLUSION

The second part of D2.1.3 has been accomplished by conducting a validation exercise using 6 data sets from the New MEXICO data from the wind tunnel experiment with the MEXICO rotor in the DNW tunnel in June-July 2014.

Three CFD codes; the compressible code WMB from CENER; the compressible code MaPFLOW from NTUA and the incompressible code EllipSys3D were used in the validation exercise. It is codes used in the Innwind project but also by industry. Then two medium fidelity codes; the vortex code GENUVP from NTUA and the Actuator Line code from DTU were also part of the exercise. Finally, two widely used aeroelastic codes in research and industry; the FAST code and the HAWC2 code were validated.

The comparison of measured pressure distributions with simulations showed overall very good agreement for the 6 data sets representing two rotational speeds and three wind speeds. In particular the prediction of the massive separation at high wind speed was predicted very well. The selected validation cases included tip speeds of 100m/s and there was no clear indication of major compressible effects.

The blade forces were validated at five radial positions and the biggest scatter between the simulated results were found at the 92%R station where the tip correction plays an important role. Compared with the measured forces there was a systematic over prediction of the normal forces on the mid part of the blade where the Risoe A1-21 airfoil is used. The airfoil has a considerable higher zero lift than the neighbouring airfoils but the predicted higher loading was not seen in the measurements.

Finally comparing the integrated forces and moments a surprising fine correlation between the models as well as with the measurements were seen for the torque at the two lowest wind speed cases. As concerns the thrust force the tendency is slightly over prediction of the force.

As a final conclusion it can be stated that the measurable set up in the smart D2.1.3 description: "Simulation models validated against the New Mexico data" has been fulfilled.

## REFERENCES

- [1] J. G. Schepers and H. Snel, "Model experiments in controlled conditions," ECN-E-07-042, Energy Research Center of the Netherlands, 2007.
- [2] J. G. Schepers and K. Boorsma, "Final report of IEA Task 29, Mexnext (Phase 1): Analysis of MEXICO wind tunnel measurements," ECN-E-12-004, Energy Research Center of the Netherlands, 2012.
- [3] J. G. Schepers and K. Boorsma, "Final report of IEA Wind Task 29: Mexnext (Phase 2)," ECN-E-14-060, Energy Research Center of the Netherlands, 2014.
- [4] S.-I. Gomez, "CFD for Horizontal Axis Wind Turbines," PhD Thesis, University of Liverpool, 2009.
- [5] M. M. Hand, "Unsteady Aerodynamics Experiment Phase VI: Wind Tunnel Test Configurations and Available Data Campaigns.," Technical report TP-500-29955, NREL, 2001.
- [6] J. Schepers and H. Snel, "Model Experiment in Controlled Conditions, Final Report.," Technical report, ECN, 2007.
- [7] S. Osher and S. Chakravarthy, "Upwind Schemes and Boundary Conditions with Applications to Euler Equations in General Geometries," *J. Comp Phys.J.*, vol. 50, p. 447–481, 1983.
- [8] B. v. Leer, "Towards the Ultimate Conservative Difference Scheme, V. A Second Order Sequel to Godunov's Method," *J. Comp. Phys.*, vol. 32, pp. 101-136, 1979.
- [9] O. Axelsson, "Iterative Solution Methods," Cambridge University Press: Cambridge, MA., 1994.
- [10] G. Papadakis and S. G. Voutsinas, "In view of accelerating cfd simulations through coupling with vortex particle approximations," *The Science of Making Torque from Wind Journal of Physics: Conference Series*, p. pp. 012126., 2014.
- [11] P. Roe, "Approximate Riemann solvers, parameter vectors, and difference schemes," *Journal of computational physics*, vol. 43(2), pp. 357-372, 1981.
- [12] V. V., "On the accuracy of limiters and convergence to steady state solutions," *AIAA Paper 93-0880.*, 1993.
- [13] Y. Saad, "Iterative methods for sparse linear systems. 2003," Siam, 2003.
- [14] W. S. Shen, "Actuator line/Navier–Stokes computations for the MEXICO rotor: comparison with detailed measurements," *Wind Energy*, vol. 15, pp. 811-825, 2012.
- [15] J. A. Michelsen, "Basis3D - a Platform for Development of Multiblock PDE Solvers," Technical Report AFM 92-05, Technical University of Denmark, Department of Fluid Mechanics, December 1992, 1992.
- [16] J. A. Michelsen, "Block structured Multigrid solution of 2D and 3D elliptic PDE's," Technical Report AFM 94-06, Technical University of Denmark, Department of Fluid Mechanics, 1994.
- [17] N. N. Sørensen, "General Purpose Flow Solver Applied to Flow over Hills," Technical Report Risø-R-827-(EN, Risø National Laboratory, June 1995, 1995.
- [18] S. V. Spalding and D. B. Patankar, "A Calculation Procedure for Heat, Mass and Momentum Transfer in Three-Dimensional Parabolic Flows," *Int. J. Heat Mass Transfer*, vol. 15, 1972.
- [19] C. M. Rhie, "A numerical study of the flow past an isolated airfoil with separation," Report PhD Thesis, Univ. of Illinois, 1981.
- [20] B. P. Leonard, "A stable and accurate convective modelling procedure based on quadratic upstream interpolation," *Comput. Meths. Appl. Mech. Eng.*, vol. 19, pp. 59-98, 1979.
- [21] F. Menter, "Zonal Two Equation Kappa-Omega Turbulence Models for Aerodynamic Flows," in *In 23rd Fluid Dynamics, Plasmadynamics, and Lasers Conference*, 1993.
- [22] F. R. Menter, R. B. Langtry, S. R. Likki, Y. B. Suzen, P. G. Huang and S. Völker, "A Correlation-Based Transition Model Using Local Variables, Part I - Model Formulation," in *In Proceedings of ASME Turbo Expo 2004, Power for Land, Sea, and Air, June 2004.*, 2004.

- [23] J. A. Michelsen, "Beregning af laminar-turbulent omslag i 2D og 3D," Forskning i aeroelasticitet EFP-2001, Technical Report Risø-R1349(DA), Risø National Laboratory, 2002., 2002.
- [24] N. N. Sørensen, "Rotor computations using a 'Steady State' moving mesh.," in *Abstract from IEA Joint Action Committee on Aerodynamics*, Pamplona, Spain, 2005.
- [25] N. N. Sørensen, A. Bechman, P.-E. Réthoré and F. Zahle, "Near wake Reynolds-averaged Navier–Stokes predictions of the wake behind the MEXICO rotor in axial and yawed flow conditions. *Wind Energy*," *Wind Energy*, vol. 17, no. 1, pp. 75-86, 2014.
- [26] T. J. Larsen and A. M. Hansen, "How to HAWC2, the users manual," Technical Report Risø-R-1597(en), Risoe National Laboratory, Technical University of Denmark., 2007..
- [27] S. A., *Dynamics of Multibody Systems*, New York: Cambridge University Press: New York, 1988.
- [28] H. A. Madsen, V. Riziotis, Z. F. M. O. Hansen, H. Snel, F. Grasso, E. Politis and F. Rasmussen, "BEM Blade element momentum modeling of inflow with shear in comparison with advanced model results," *Wind Energy 2011; 15(1): 63–81. DOI: 10.1002/we.493.*, vol. 15, pp. 63-81, 2011.
- [29] M. H. Hansen, M. Gaunaa and H. A. Madsen, "Beddoes-Leishman type dynamic stall model in state-space and indicial formulations," Technical Report Risø-R-1354(EN), Risoe National Laboratory, 2004.
- [30] L. J and B. T, "A generalized model for airfoil unsteady aerodynamic behaviour and dynamic stall using the indicial method," in *Proceeding of the 42nd Annual Forum of the American Helicopter Society*, Washington D.C., 1986.